NANOTRIBOLOGY AND NANOMECHANICS OF THIN FILMS INCLUDING MATERIAL CHARACTERIZATION, MECHANICAL WEAR, ADHESION AND LUBRICATION

A Dissertation

by

YOUFENG ZHANG

Submitted to the Office of Graduate and Professional Studies of
Texas A&M University
in partial fulfillment of the requirements for the degree of

DOCTOR OF PHILOSOPHY

Chair of Committee,	Andreas A. Polycarpou
Committee Members,	Haiyan Wang
	Anastasia Muliana
	Jonathan R. Felts
Head of Department,	Andreas A. Polycarpou

August 2017

Major Subject: Mechanical Engineering

ABSTRACT

The present work is dedicated to addressing nanotribological issues of ultra-thin (sub-10 nm) films at contacting interfaces. In devices such as micro-electro-mechanical systems (MEMS), thin films are deposited for specific functions. In some occasions, mechanical durability of the thin films is also important. Magnetic storage hard disk drives (HDD) are a good example where nanotribology at the head-disk interface (HDI) is extremely important. Especially in recent years, where the areal density increases exponentially and the write/read head has been brought as close to as less than 10 nm to the disk surface. As a result, direct contact is possible to occur at such small distance and such unfavorable contact will cause mechanical wear and demagnetization. Nanometer thick diamond like carbon (DLC) and lubricant films provide important protection and study of their failure mechanisms is necessary.

The present thesis has conducted research to understand the nanotribology of thin films in the multilayered system used in HDDs. The majority of the work is measurement of the nanomechanical and nanotribological properties of the solid thin films with thickness of less than 20 nm. A method combining finite element analysis (FEA) and nanoindentation was proposed to extract nanomechanical properties from nanoindentation data for multilayered samples. A highly sensitive nanomechanical transducer was introduced to perform sub-5 nm shallow nanoindentation experiments on thin films deposited at different conditions. To study the tribological performance of DLC films at high temperatures up to 300 °C, the present work performs nanoscratch and nanowear

tests on a 3-nm thick DLC film. The results show the wear rate of DLC films begin to increase abruptly at around 200°C and this degradation of wear resistance is irreversible. The present thesis also proposes a mathematical model to quantitatively predict the hydrodynamic lubrication effects of the molecularly thin lubricant between the head and the disk surfaces. After considering the nanorheological behavior of the lubricant, the model is able to make predictions of contacting forces and pressures and explain the tribological role of the lubricant in terms of continuum mechanics. Lastly, present thesis proposed a model considering Van der Waals forces between lubricants on the disk and on the head. The proposed model provides stricter criterion for onset of adhesion induced lubricant-transfer between the two wet surfaces and is in better agreement with Molecular Dynamics simulations than conventional models.

In summary, the findings above center about nanomechanics and nanotribology at the interfaces of the magnetic storage hard disk. However, these findings can also extend their applications to other MEMS devices where tribology issues are of important concerns. The shallow nanoindentaton instrument and FEA-based characterization method can be applicable any other solid thin films. The high-temperature tribological properties of a ultra-thin DLC films utilize a unique test rig but the findings are generally instructive in understanding behaviors of DLC at high temperature. The nano-lubrication model for a lubricated single asperity can be an addition of current contact mechanics which usually neglects the presence of lubricants.

ACKNOWLEDGEMENTS

I would like to thank my committee chair, Dr. Andreas Polycarpou, and my committee members, Dr. Haiyan Wang, Dr. Anastasia Muliana, and Dr. Jonathan Felts, for their guidance and support throughout the course of this research. Their discussion toward excellent research always motivated me to dig deeper and explore new unknowns. It was my pleasure and great honor to have these great researchers and teachers in my committee.

Special thanks go to my Ph.D. advisor, Prof. Andreas Polycarpou. His passionate pursuit of academic work encouraged me to overcome difficulties I met during my Ph.D. research. He is not only a good advisor, but also a great human being from who I learned expertise and also wisdom. For such I named my first-born son after his name.

Thanks also go to my friends and colleagues and the department faculty and staff for making my time at Texas A&M University a great experience. I also want to Thank Dr. Emerson Escobar Nuenz and Dr. Tanil Ozkan for their valuable discussions and my labmates including Wasim Akram, Shahla Chowdury, Pixiang Lan, Mohammad Humood and Stephen Keen for their help with some work in present thesis.

Thanks to my mother and father for their love and support from China. My mother, Guifang Huang, passed away in November 2014. Her untimely passing is a major loss and regret for me. I believe she would be happy to see my Ph.D. graduation in heaven.

Finally, I would like to thank my wife, Tianliao (Olivia) Ma, for her persistent patience and love; and my son, Andreas Zhang, for the happiness he brought to the whole family.

CONTRIBUTORS AND FUNDING SOURCES

This thesis was completed mainly based upon supervision of my committee chair, Dr. Andreas Polycarpou, and my committee members, Dr. Haiyan Wang, Dr. Anastasia Muliana, and Dr. Jonathan Felts.

Experimental results shown in Chapter 4 and Chapter 5 were obtained with help of my colleagues in the group, Pixiang Lan and Mohammad Humood.

The motivation of this work was through a sponsored research project from Seagate Technology LLC, with Grant No. SRA-32724.

NOMENCLATURE

a	Blunt radius
A_c	Contact area
a-C:H	amorphous hydrogenated carbon
AFM	Atomic force microscope
A_n	Nominal contact area
BPM	Bit Patterned Media
BR	Bonding ratio
COC	Carbon overcoats
CVD	Chemical vapor deposition
DLC	Diamond-like carbon
E^*	Combined elastic modulus of elasticity= $1/(\frac{1-v_1^2}{E_1}+\frac{1-v_2^2}{E_2})$
E_r	Reduced elastic modulus= $1/(\frac{1-v^2}{E}+\frac{1-v_i^2}{E_i})$
F	Force
FEA	Finite Element Analysis
H	Hardness
h	Displacement
HAMR	Heat Assisted Magnetic Recording
h_c	Contact depth
$h_{conical}$	Depth of the conical part

HDD	Hard Disk Drives
HDI	Head Disk Interface
HMS	Head Media Spacing
$h_{spherical}$	Spherical depth
k	Specific wear rate
k_b	Boltzmann constant
K_w	Wear coefficient
m	mass
MEMS	Microelectromechanical System
MTL	Molecularly thin lubricants
P	Normal contact load
p	Normal contact pressure
PEEQ	Equivalent plastic strain
PFPE	Perfluoropolyether
PPA	Parallel plate actuator
Q	Shear force
R	Asperity radius, tip radius
Ra	Radius of asperity
RMS	Root mean square
R_q	Root mean square roughness
S	Sliding distance, unloading stiffness
SEM	Scanning Electron Microscope

SPM	Scanning Probe Microscope
t	Film thickness
TEM	Transmission Electron Microscopy
W_d	Wear depth
β	Correction factor in nanoindentation
η	Areal density of asperities
μ	Friction coefficient
v	Poisson's ratio
σ_y	Yield strength

TABLE OF CONTENTS

LIST OF FIGURES

Page

LIST OF TABLES

1 INTRODUCTION AND LITERATURE REVIEW

1.1 Introduction to nanotribology

The word tribology derives from Greek, meaning "knowledge of rubbing." According to Wikipedia (Wikipedia contributors, 2017), "tribology is the study of science and engineering of interacting surfaces in relative motion." It includes the study and application of the principles of friction, lubrication and wear. Tribology is a branch of mechanical engineering and materials science". With development of manufacturing, deposition and characterization techniques, the study of tribology has also reached nanoscale dimensions and given birth to the term "nanotribology." Figure 1.1 shows elements involved in nanotribology. It is an interdisciplinary area involving knowledge of interfacial forces (adhesion and friction), characterization of nanomechanical properties (nanoindentation and Atomic Force Microscopy), nanowear mechanisms, lubrication, coatings and lubricants, etc.

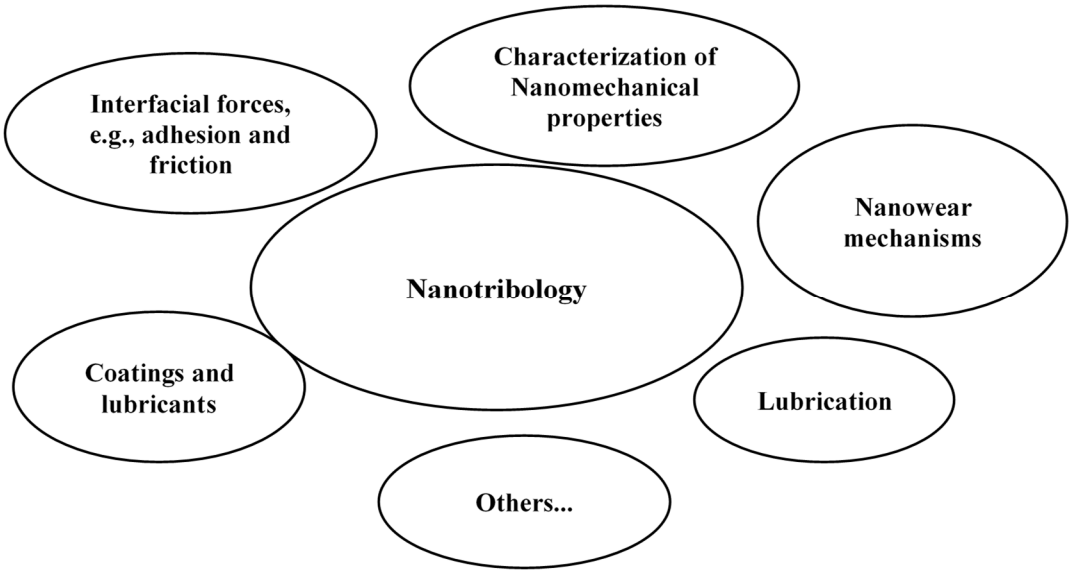

Figure 1.1 Elements involved in nanotribology.

1.2 Nanotribology in magnetic storage

A successful example of the application of nanotribology is in magnetic storage devices. Figure 1.2 depicts a schematic view of the head disk interface (HDI). The disk is driven by a spindle spinning at high a speed (~7,200-15,000 rpm). The write/read head is embedded in the slider and takes the charge of reading or writing data stored on the magnetic media below it. Both the head and the media are coated with a thin Diamond-like carbon (DLC) as protective layer. On the disk surface, above the DLC coating, there is an additional molecularly thin perfluoropolyether (PFPE) lubricant to reduce friction.

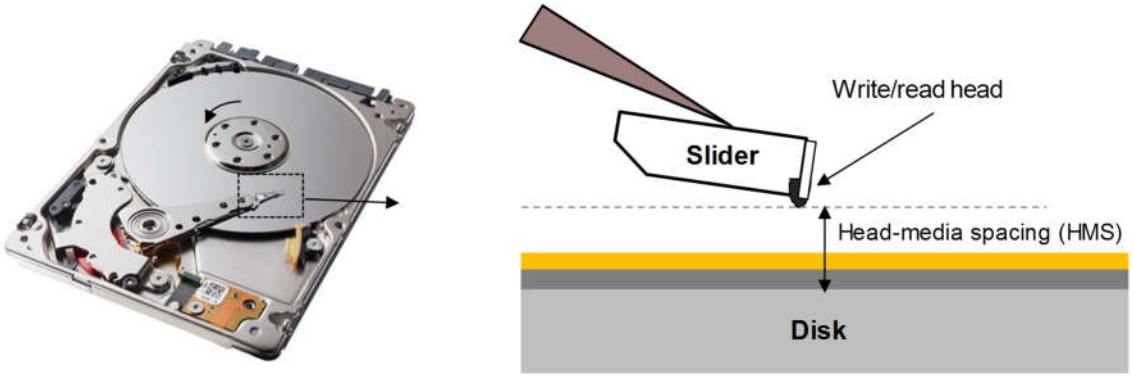

Figure 1.2 Schematic view of the head-disk interface.

The distance between the head and the media is called "Head-media spacing (HMS)." HMS is an important terminology in the hard disk drive (HDD) industry because it is the key factor in determining the areal density of the HDD. The smaller HMS is, the closer the head is to the media and the less area of media is required to store per unit amount of data. Figure 1.3 is a roadmap showing the correlation of the areal density with HMS. The areal density increases sharply with HMS and for the present 1 Tb/in^2 areal density an HMS of less than 10 nm is required (Marchon et al., 2013).

Please note that HMS does not represent the smallest distance between the head and the disk surfaces. There are carbon overcoats on both the disk and the head surfaces with a total thickness of ~4 nm and a molecularly thin lubricant with thickness of ~1 nm. In addition, if we consider surface roughness that is about 0.2 nm (rms values), which means the highest asperity is 0.6 nm. Given an HMS of 10 nm, the actual margin for the head to fly over the disk surface without direct contact is less than 5 nm. As a result, there is a higher probability for direct contact of the head and the disk surface with lower spacing. And this direct contact is one of the major reasons for failure of HDDs.

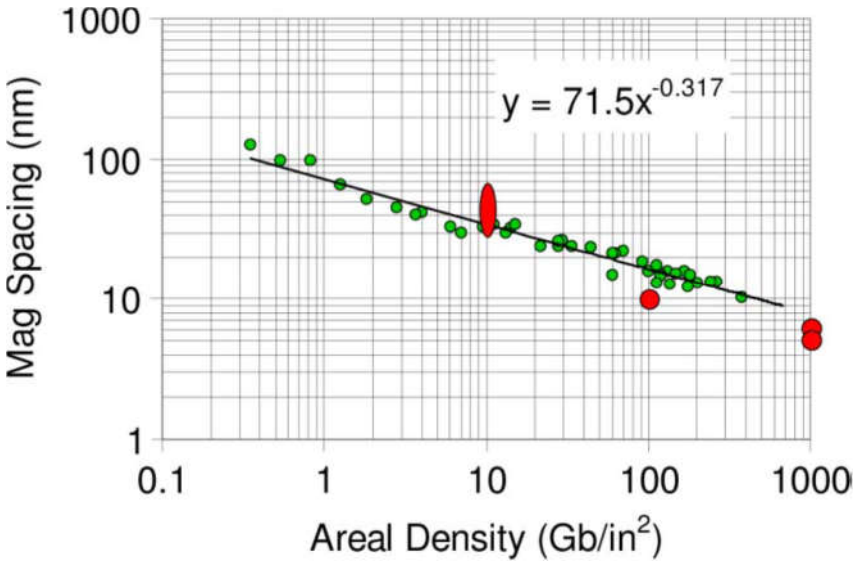

Figure 1.3 Roadmap for areal density of HDDs (Marchon et al., 2013).

Figure 1.4 shows the surface of a used hard disk under optical microscopy. The wear pits in series are due to scratches of the writing/reading head. When the head contacts with the disk surface, the media material is at the risk of mechanical wear and also high temperature due to frictional heating. Both of them can cause demagnetization and thus data loss. Severe mechanical wear may induce tilting of grains in the recording material and physically damage the data storage media (Xu et al., 2009); and frictional heating can give rise to transient high temperature that leads to data erasure (Roy and Brand, 2007). Meanwhile, the high velocity impact can destroy the head material as well. Therefore, nanotribology at the head-disk interface is extremely important in terms of mechanical durability and has been one of the major challenges for the HDD industry to increase the areal density (Gui, 2003).

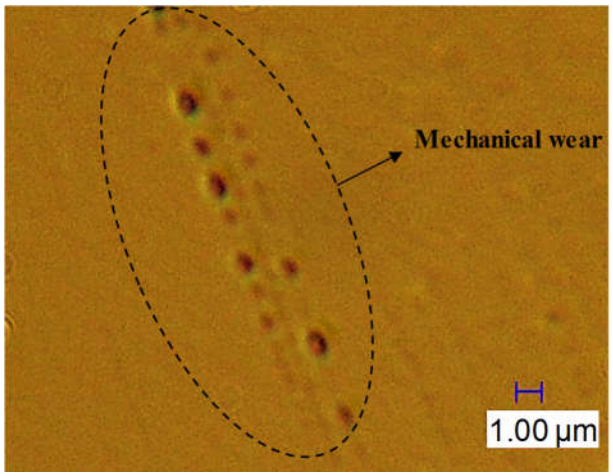

Figure 1.4 Wear pits on the surface of a hard disk under optical microscopy.

1.3 Objectives and outlines

Due to the importance of HDI nanotribology, the present thesis is dedicated to the improvement of mechanical reliability of HDDs by reducing tribology induced failures. In fact, applications of the findings in the present thesis can be extended to any other MEMS devices that have nanotribological issues. Fig. 1.5 depicts the outline of the research work in the form of a flowchart. The work can be categorized from two aspects. The x-axis represents categorization by elements for research methodology including instrumentation, characterization and analysis, and tribological properties. The y-axis defines the work according to contact regimes between the head and the disk surfaces, i.e., solid contact, lubricant contact and no contact corresponding to the distance between the disk and the head increasing from small to large.

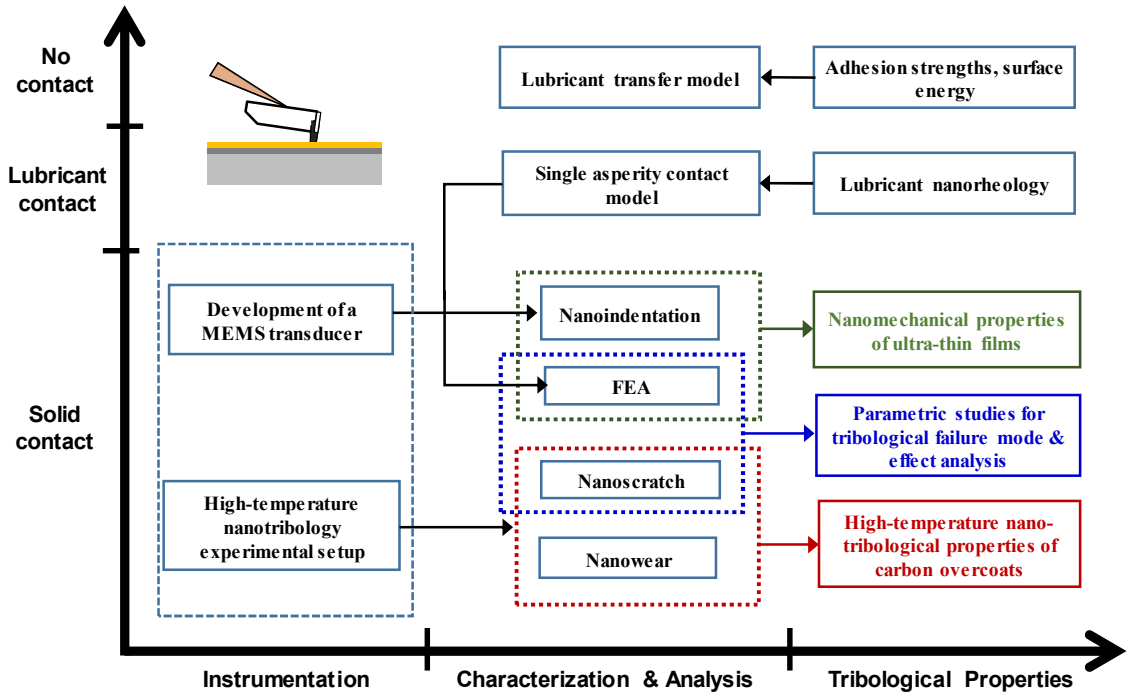

Figure 1.5 Outlines and structure of work in current thesis.

According to the contact regime, the present thesis can be divided into the following three parts:

(1) Solid-contact regime (Chapters 2, 3, 4 and 5). This regime takes up the majority of the contents in the present research as the core of the HDD, the recording layer, is sandwiched in multiple layers of thin films. Comparing to the previous two parts, this part has a good amount of experimental work using nanoindentation, nanoscratch and nanowear techniques. These techniques were employed to measure the nanomechanical and nanotribological properties of thin films.

In Chapter 2, the thesis proposes a method of combining nanoindentation and Finite Element Analysis (FEA) in order to extract nanomechanical properties of thin films

from loading-unloading responses by curve-fitting. In Chapter 3, a highly sensitive nanomechanical transducer was developed to achieve sub-10 nm shallow nanoindentation experiments. Then, the sensitive transducer was utilized to measure nanomechanical properties of 14-nm nanocomposite recording layers, as demonstrated in Chapter 4. The nanotribological properties were also characterized using a regular nanoindentation transducer. In Chapter 5, the thesis demonstrates high-temperature tribologoical testing on an ultra-thin DLC coating using a state-of-the-art high-temperature stage, which provides insight for understanding of the tribological behaviors of carbon films under high-temperature conditions.

(2) Lubricant-contact regime (Chapter 6). As the flying height of the head goes lower, the lubricant-contact regime is reached. The nanometer thick lubricant is confined between the head and disk surfaces under extremely high shear rates ($\sim 10^{11}$ s^{-1}) and there are hydrodynamic forces generated. The present work proposed a nanolubricaton model by taking into account behaviors of lubricants under sliding contact at the nanoscale, in order to understand the role of the lubricant in terms of mechanics.

(3) No-contact regime (Chapter 7). Lubricant transfer is an important phenomenon and used to decide the safe clearance or spacing in the HDD industry. The present investigation of lubricant transfer belongs to the no-contact regime where atomic level forces are considered in the proposed model to predict the onset of lubricant transfer from the disk to the head. In this regime, adhesion behaviors and properties of the lubricant are involved. The critical condition (distance) for Lubricant-transfer from one wet surface to another is determined based on the equilibrium of net Van der Waals forces.

1.4 Recommended future work

As continuation of the work by present thesis, high-temperature contact mechanics between two rubbing surfaces can be one path of the future work. With the current high-temperature nano-mechanical stage, it is feasible to characterize dependence of mechanical properties and surface adhesion strengths on the temperature. Then the temperature dependence can be substituted into the conventional continuum mechanics and lead to predictions of contact forces, plastic deformation and friction coefficients. And also, high-temperature tribological tests can be performed in order to compare predictions by the model and results from experiments.

2 A FINITE ELEMENT CORRECTION METHOD FOR SUB-20 NM NANOINDENTATION CONSIDERING TIP BLUNTNESS

2.1 Introduction to FEA-nanoindentation method

The indentation and specifically nanoindentation technique is widely used to measure the mechanical properties of materials, including thin films. Tabor (1970) proposed that the indentation hardness is related to the yield strength with a coefficient of 2.8. With the advancement of nanoindentation instruments, Pethica et al. (1983) obtained hardness at indentation depths as low as 20 nm. Investigation to obtain the elastic modulus using the indentation technique followed. Loubet et al. (1984) utilized the solution for elastic punch by Sneddon (1965) and proposed a relation between the unloading slope and the reduced modulus for a Vickers indenter. Doerner and Nix (1986) proposed a relation between the unloading compliance and the reduced modulus for a pyramid indenter (such as a Berkovich indenter). Subsequently Oliver and Pharr (1992) published the classical work that calculates the elastic modulus and hardness from load-displacement responses obtained from indentation experiments. As for shallow indentation experiments discussed here, they demand high-resolution force and displacement sensors to ensure low noise level and very sharp indenters to cause plastic deformation at low contact depths (Yu et al., 2005; Lee et al., 2007). Another obstacle for characterizing and measuring mechanical properties of such ultra-thin films is substrate effects. It is generally accepted that the indentation depth has to be less than 10% of the film thickness to minimize substrate effects. Note that the 10% rule only applies to hardness measurements (Fischer-Cripps,

2006) and in some cases, substrate independent measurements allow indentation depths up to 25% (Doerner et al., 1986).

In the literature (Saha and Nix, 2002; Li and Vlassak, 2009), substrate effects are evaluated by relying on numerical solutions of the stress field for the film/substrate composite (King, 1987; Yu et al., 1990). Such techniques assume that indenters have a perfect geometry, such as flat-ended cylindrical, quadrilateral, and triangular punches (King, 1987), and conical and spherical punches (Yu et al., 1990). For contact depths on the order of 100 nm or more, these methods are effective in determining substrate effects. However, when the contact depth is shallow (less than 20 nm), minute defects of the indenter tip (especially at the very top of the tip) have a significant effect, and thus cannot be neglected, and are addressed in this work.

The Finite Element Method (FEM) has been used to investigate mechanical properties of thin films, combined with the nanoindentation technique. FEM-nanoindentation techniques follow the same routine, namely adjusting the FEM input mechanical properties until the force-displacement response correlates well with the experimental nanoindentation measurements, and the best-fit mechanical properties are regarded as FEM-extracted mechanical properties. Usually the materials are taken as elastic perfectly plastic to reduce complexity and also to avoid multiple solutions with variable strain hardening coefficients. Bhattacharya and Nix (1988) used FEM to simulate load-depth responses by nanoindentation experiments for Si, Al and Ni. Pethica et al. (1983) performed sub-micrometer indentations and proved that FEM can be a reliable technique to extract mechanical properties. Lichinchi et al. (1998) simulated indentation

experiments on TiN and high-speed steel with a Berkovich probe and obtained yield strength values by fitting the loading-unloading curves. They also compared the loading-unloading curves by a 3D model and an equivalent 2D conical model that has the same projected contact area as the 3D indenter and found that the 2D FE models gave similar results. Therefore, many FE simulations employ equivalent 2D conical spherical tip models to save computational time. Pelletier et al. (2000) investigated strain-hardening behavior of metals using FEM, by fitting the experimental curves. Yu et al. (2004) built a spherical-conical FE model for two different indenters based on analytical expressions of their area function. Using FEM, they obtained the mechanical properties of coatings on bilayered samples. FEM nanoindentation has also been applied for investigations of pile-up (Taljat and Pharr, 2004), substrate effects (Sun et al., 1995; Chen and Vlassak, 2001), indentation size effects (Chen et al., 2016) and scaling parameters (Cheng and Cheng, 1998).

In the present study, we use the FEM to extract mechanical properties of ultra-thin films. First, we show that the conventional FE fitting technique is incorrect at shallow contact depths due to the assumption of point contact when the contact depth h_c=0. Using scanning electron microscopy (SEM) we measure the top of the indenter tip, which has a "flat" portion. We then develop a generalized analytical expression for the area function including tip bluntness. This tip bluntness is determined from FEA-fitting with an elastic punch on Fused Quartz. Such a blunt-tip FE model is applied on a bulk material (Fused Quartz), and on a thin film stack composed of a 90 nm metal layer and a 14 nm magnetic layer on a glass substrate material.

2.2 Basic indentation theory

From indentation experiments, the force and displacement curves of the indenter are recorded and referred to as loading-unloading curves. According to the Oliver-Pharr method (Oliver and Pharr, 1992), the reduced modulus is related to the unloading stiffness as:

$$S = \left(\frac{dP}{dh}\right) = \beta \frac{2}{\sqrt{\pi}} E_r \sqrt{A}, \tag{2.1}$$

where dP/dh is the slope of the unloading curve (unloading stiffness); β is a correction factor with a value of around 1; $\frac{1}{E_r} = \frac{1-v^2}{E} + \frac{1-v_i^2}{E_i}$, E and v are the elastic modulus and Poisson's ratio of the sample, E_i and v_i are the corresponding properties for the indenter; A is the projected contact area that usually takes the following form:

$$A = C_0 h_c^2 + C_1 h_c + C_2 h_c^{1/2} + C_3 h_c^{1/4} + C_4 h_c^{1/8} + C_5 h_c^{1/16}, \tag{2.2}$$

where h_c is the contact depth related to the maximum depth and the slope of the unloading curve, C_0, C_1, ...C_5 are coefficients determined from curve-fitting calibration indentation data. The indentation hardness follows the conventional form:

$$H = \frac{P_{max}}{A}. \tag{2.3}$$

Fused Quartz is usually used to calibrate the area function because of its stability and known properties. After indentation using different load values on the Fused Quartz standard sample, each indentation curve can yield an unloading stiffness S_i. Because the reduced elastic modulus of Fused Quartz is known to be 69.6 GPa, then from Eq. (2.1) the contact area corresponding to each test A_i can be obtained. Then the area function can be obtained by fitting data points of A_i as a function of h_c using Eq. (2.2). For measurements

on other samples, the reduced modulus and the hardness can be calculated from Eq. (1) and Eq. (2.3) with substitution of the calibrated area function.

2.3 Experimental

2.3.1 Calibration experiments on Fused Quartz

The present study utilizes a commercial nanoindenter Triboscope (Hysitron, Inc., MN) and a diamond cube corner probe. To obtain the area function of the probe, experiments were performed on Fused Quartz standard sample using a triangular load with the maximum load varying from 20 μN to 120 μN. The measured elastic modulus and hardness values based on the Oliver-Pharr method are shown in Fig. 2.1, focusing on shallow indentation depths up to 25 nm.

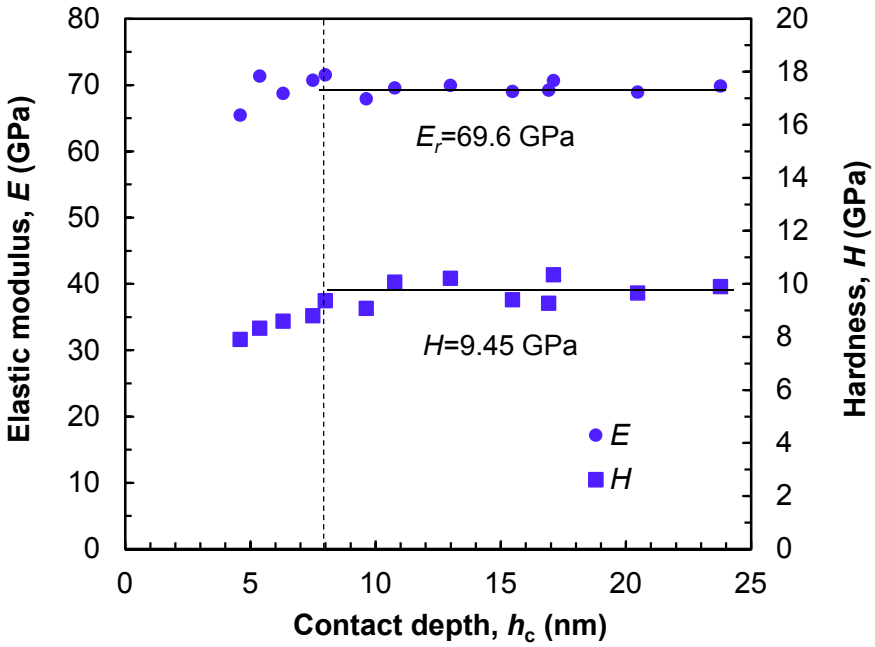

Figure 2.1 Experimental reduced elastic modulus and hardness values of standard Fused Quartz sample.

The reduced modulus is calibrated as 69.6 GPa. The resultant hardness has a mean value of 9.45 GPa which is close to the reference value of 9.25 GPa. However, note that the hardness and reduced modulus values for contact depths less than 7 nm show a decreasing trend. Usually for shallow indentation experiments, the measured hardness at indentation depths less than 10% of the tip radius is underestimated, which is commonly seen for shallow indentation experiments (Yu and Polycarpou, 2004; Yeo and Polycarpou, 2007) and also observed by FE simulations (Lu and Bogy, 1995). Note that Fused Quartz is amorphous without any known surface layers, and so are the solid thin films discussed in this paper, and the increasing trend at shallow depths in Fig. 2.1 is contrary to the indentation size effects in crystalline materials (Nix and Gao, 1998). This phenomenon is attributed to tip bluntness (Lemoine et al. 2007) and/or contribution from elastic recovery (Yeo and Polycarpou, 2007). No matter how this phenomenon is induced, the nanoindentation hardness and modulus at shallow depths (h_c<10%R_{tip}) based on the Oliver-Pharr method are underestimated and cannot be taken as the real intrinsic mechanical property values.

2.3.2 Conventional area function

The area function fitted by Eq. (2.2) is shown in Fig. 2.2. At shallow contact depths, especially at h_c < 3 nm, the fitted area function is negative and obviously incorrect. The reason is that Eq. (2.2) assumes A=0 nm^2 at h_c=0 nm, meaning that the onset of contact between the tip and the sample surface is a point contact. However, in practice the tip geometry is imperfect or blunt due to mechanical wear or manufacturing defects and the tip top is flat rather than spherical. In such a case, the conventional contact area obtained

by Eq. (2.2) cannot be used for shallow depths and so does the spherical-conical FE model for the tip. Yeo and Polycarpou (2007) identified this problem and proposed an improved contact area function for the residual contact area only, which does not include any elastic deformation. Their reduced area function results in hardness values that are in better agreement with reference values, at very shallow depths. However, the proposed correction in by Yeo and Polycarpou (2007) relies on extremely shallow indentation data (to cause elastic deformation only), which are not readily obtainable with standard nanoindentation instruments. Moreover, it uses a variable tip radius (for extremely shallow depths), which is a function of contact depth, which is quite complex to implement in practice.

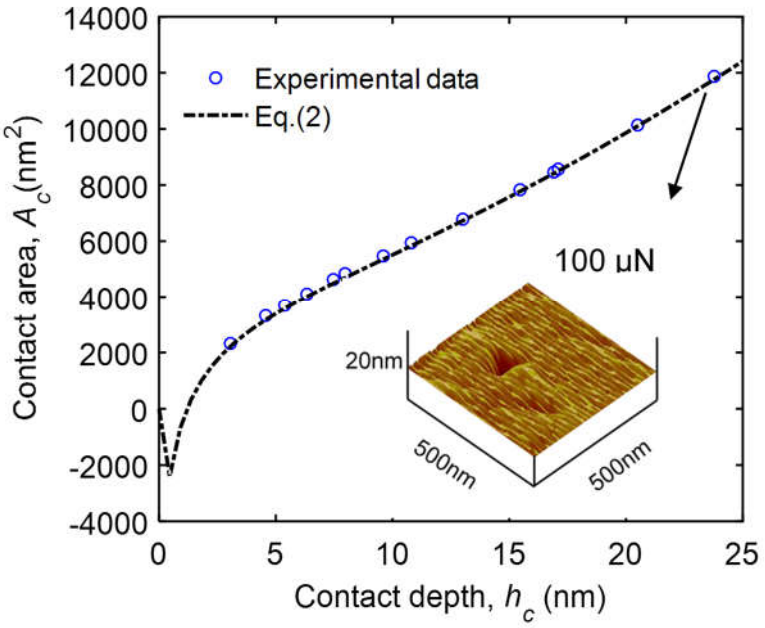

Figure 2.2 Area function fitted using Eq. (2.2). The insert shows a typical residual image of a 100 μN maximum load nanoindentation experiment, corresponding to the maximum h_c in the figure.

2.3.3 Proposed improved area function

SEM was used in the present study to characterize the tip geometry. Fig. 2.3(a) shows an overall image of the cube corner probe. From such image, it is difficult to extract geometry information of the very top of the tip. A zoomed in image shown by Fig. 2.3(b), shows that the tip radius can be roughly estimated at about 100 nm. Though it is impossible to precisely measure the tip radius suing SEM, it can be seen from Fig. 2.3(b) that the tip is not exactly spherical on the top but has a "flat cap."

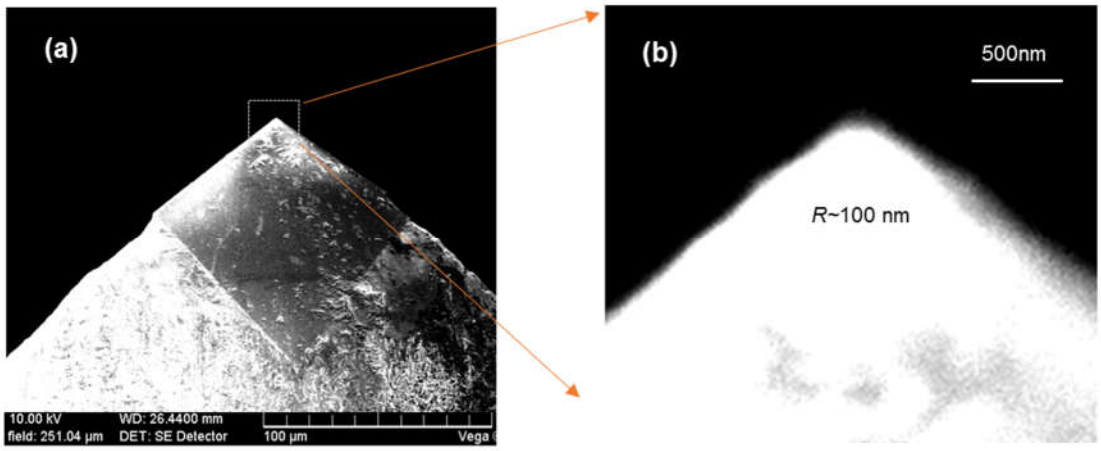

Figure 2.3 SEM images of the indenter: (a) overall image, (b) zoom-in showing the imperfection on the top of the tip.

Recall the discussion in reference to Fig. 2.2 that the conventional area function Eq. (2.2) cannot represent the test data at very shallow contact depths. Considering the SEM image of the tip of the imperfect indenter, the present study proposes a solution for this issue from the geometry of the indenter point of view and employs an area function by adding a constant term A_0 to take into account the degree of tip wear or bluntness:

$$A = A_0 + C_0 h_c^2 + C_1 h_c + C_2 h_c^{1/2} + C_3 h_c^{1/4} + C_4 h_c^{1/8} + C_5 h_c^{1/16}, \quad (2.4)$$

where A_0 is the area of the "blunt top" of the indenter, as also shown in Fig. 2.4. When A_0=0, there is no blunt top and thus Eq. (2.4) reverts to Eq. (2.2). Note also that such a function has been proposed before, however, the uniqueness and contribution of the present work is on the use of a simplified FEM to obtain an accurate estimation of the contact area function at very low contact depths, thus enabling accurate nanomechanical properties at shallow depths.

Typically, an indenter no matter whether it is conical spherical or pyramidal in shape, has a radius of curvature formed on the top during manufacturing. Usually this tip radius is provided by the vendor to denote the sharpness of the indenter. The smaller the radius is, the sharper the indenter is. Yu et al. (2004) provided an analytical expression for the area function of the equivalent spherical conical tip. For example, for a perfect Berkovich tip, the half angle for the equivalent conical tip is θ≈65.35°, and for a perfect cube corner tip θ≈35.26°.

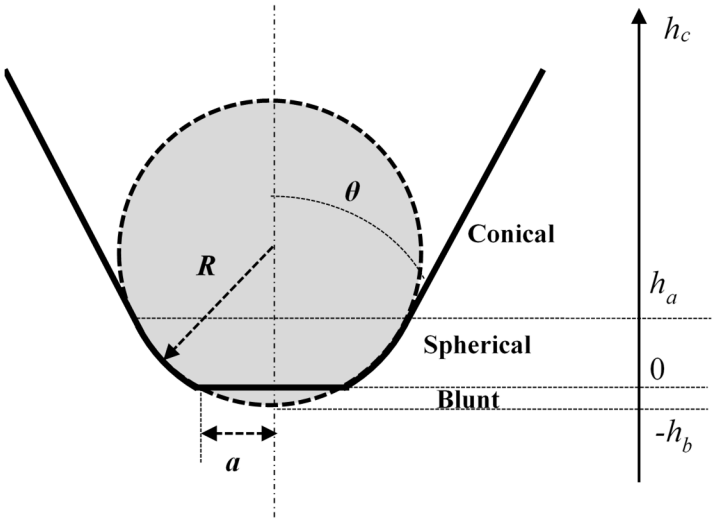

Figure 2.4 Schematic of equivalent conical spherical probe considering tip bluntness.

As per the geometry proposed in Fig. 2.4, the present study modifies the formulation of Yu et al. and proposes more generalized analytical expressions for the contact areas for the spherical and conical parts:

$$A_{spherical} = \pi(h_c + h_b)[2R - (h_c + h_b)], 0 < h_c < h_a, \quad (2.5)$$

$$A_{conical} = \pi tan^2\theta(h_c + h_b + \frac{R}{sin\theta} - R)^2, 0 < h_c < h_a, \quad (2.6)$$

where the tip radius R can be estimated as $C_1/2\pi$ after setting C_0 to $-\pi$ and coefficients C_2 through C_5 equal to zero in Eq. (2.2) (Probe Calibration, Hysitron Inc). h_a is the height of the spherical curvature and $h_a = R - R\sin\theta - h_b$. Note that by setting $h_c = 0$, the area for the blunt top in Eq. (2.4) can be obtained as

$$A_0 = \pi h_b(2R - h_b), 0 < h_c < h_a \, . \quad (2.7)$$

When $h_b = 0$ in Eq. (2.7), the blunt area $A_0 = 0$, which implies that the tip top is perfectly spherical.

2.4 FE simulations

2.4.1 Finite Element Model

FEM corresponding to the generalized analytical expressions given by Eqs. (5) and (6) is used to simulate the nanoindentation contact. Similar to FE simulations reported in the literature, the present work employs a 2D axisymmetric model to reduce computational complexity. The difference is that the present indenter is modeled as a truncated sphere to capture the bluntness of the tip. The FE model is built in ABAQUS as shown in Fig. 2.5. The indenter uses an analytic rigid model and the sample model is meshed with 5,420 axisymmetric-stress elements. The region below the indenter is heavily meshed, with element size of 1×1 nm^2. A boundary condition constraining rotation and lateral movement is applied on the axis of symmetry; another boundary condition is applied at the bottom to constrain rotations and vertical movement. A triangular load function is applied on the indenter model, the same as in the experiments. The displacement response of the indenter is extracted and plotted with the applied load, thus obtaining load-displacement responses from the FE simulations and used to compare with experiments. Note that the blunt tip area is circular and can be obtained from

$$a = \sqrt{\frac{A_0}{\pi}} = \sqrt{\pi h_b (2R - h_b)}. \tag{2.8}$$

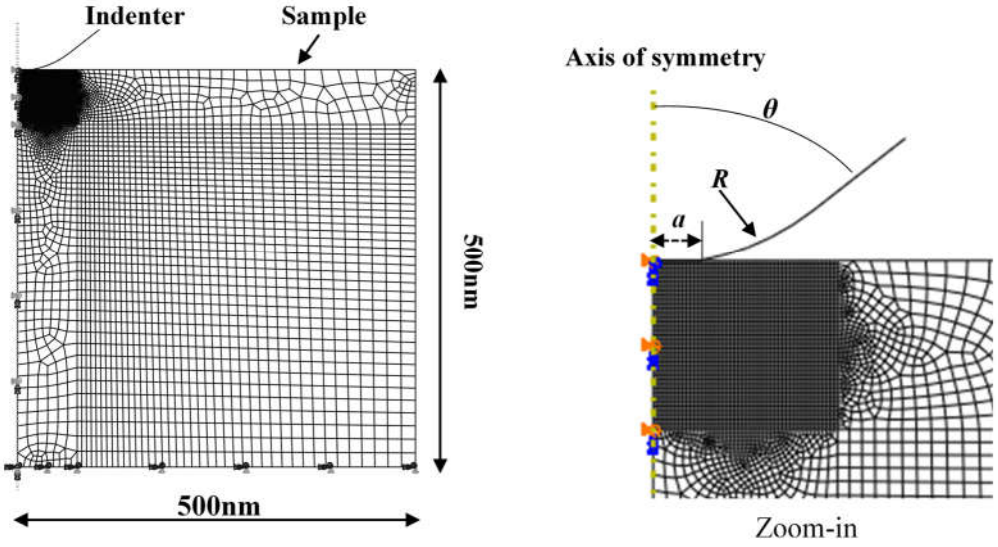

Figure 2.5 FEA model of the rigid indenter and sample, showing dense mesh in the contact region.

2.4.2 Determination of the blunt radius a

Fused Quartz is used as a calibration sample to obtain the area function because of its stable and well recognized mechanical properties. Fig. 2.6 (a) shows FE simulation data for indentation using a maximum force of 15 μN on Fused Quartz. As the peak indentation force is very small, there is no plastic deformation and the indentation behaves as an elastic punch. Also, the maximum indentation depth is only 5 nm, which limits the contact within the spherical part, i.e., $h_c < h_a$. The elastic modulus and Poisson's ratio of Fused Quartz are E=67.6 GPa and v=0.17). After inputting these elastic properties, the only parameter to be determined is the blunt tip radius a in the FE model (assuming the tip radius is known, which in this case is 85 nm).

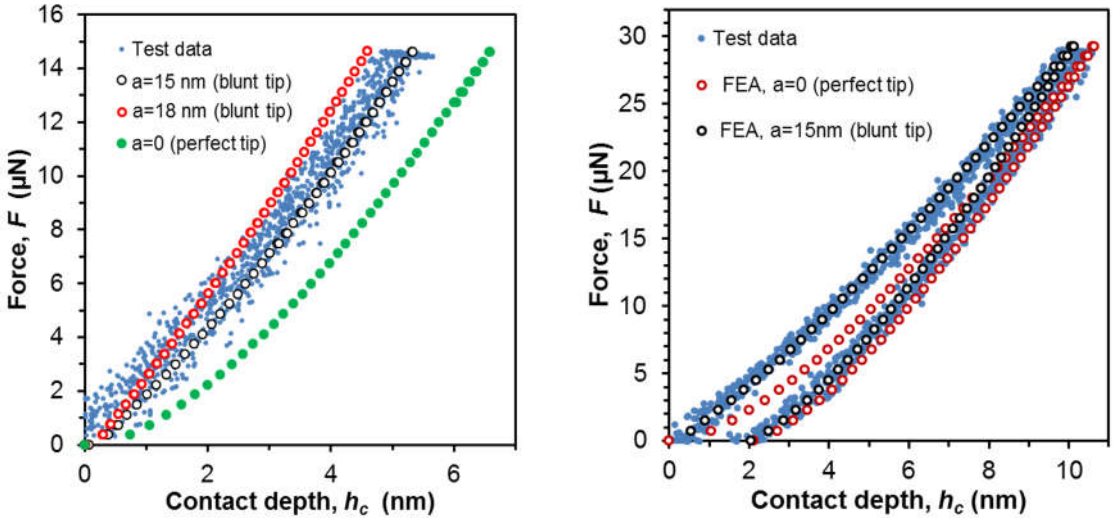

(a) (b)

Figure 2.6 FEA and experimental nanoindentation force-displacement curves on Fused Quartz: (a) determination of the blunt tip radius a assuming elastic deformation only (F_{max}=15 μN), (b) FEA best-fitting for perfect tip model (a=0 nm) and blunt tip model (a=15 nm).

Referring to Fig. 2.6(a), when a is equal to zero, the model corresponds to a perfect tip (conical or conical-spherical) and the resultant FE force-displacement response does not correlate well with the nanoindentation experiments. Through adjustment of a, it is found that when a=15 nm, the FE simulation matches the experimental data. This value agrees with previous analysis using Eq. (2.2). Note that the blunt radius should vary for different indenters. The technique proposed in this work was verified using a different cube corner indenter with a tip radius of 46 nm, where the best-fit for the blunt radius is found to be only 7 nm. Fig. 2.6 (b) shows the force-displacement curve at F_{max}=30μN from nanoindentation experiments and its best-fit from FEA using the perfect tip model (a=0 nm) and the blunt tip model (a=15 nm). The blunt tip model shows a good fit with both the loading and unloading curves, whereas the perfect tip cannot fit the experimental

data, irrespective of the input material properties. The simulated loading curve tends to be lower than the experiments. The reason is that the perfect tip model overestimates the sharpness of the tip and indents deeper than the actual indenter.

2.4.3 Validation of the FE model

Having obtained the radius of the tip bluntness *a,* using Eq. (2.8), the corresponding h_b is calculated as 1.33 nm. The last unknown parameter is half angle θ. Determination of θ relies on curve-fitting Eqs. (5) and (6) with experimental data for the contact area. The best-fit was found when θ is 42.3° (note that a typical 90° cube corner should be θ =45°). Fig. 2.7 shows the experimental contact area data and the comparison with the FE model. The developed model for the indenter will be used for all simulations in the present study.

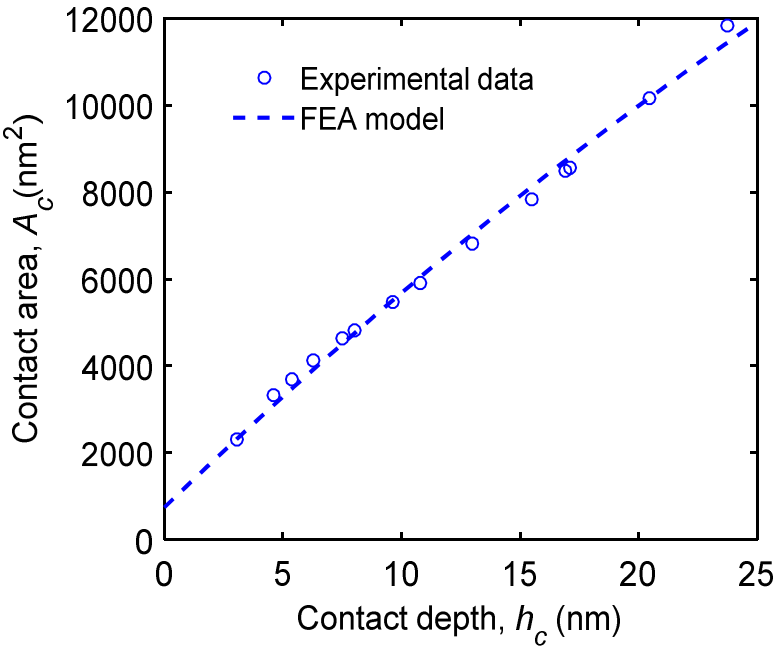

Figure 2.7 FEA model (R=85 nm, a=15 nm, θ=42.3°) for shallow indentation and corresponding contact area and comparison with experimental data.

For further validation, we performed FE simulations and nanoindentation experiments using higher indentation loads that cause plastic deformation, with maximum indentation forces of F_{max} =20, 25, 35 and 40 μN. Fig. 2.8 (a) shows the experimental results for force-displacement curves and Figs. 2.8 (b) to (e) show the corresponding FEA-fitting results for each case. The best-fit elastic moduli and yield strengths are listed in Table 2.1. The average reduced modulus obtained through FE simulations is 68.17 GPa, which is slightly lower than the reference value of 69.6 GPa. The average fitted yield strength for Fused Quartz is 4.92 GPa that is between 4.3 GPa reported by Yu et al. (2004) and 5.43 GPa reported by Xin and Lambropoulos (2000).

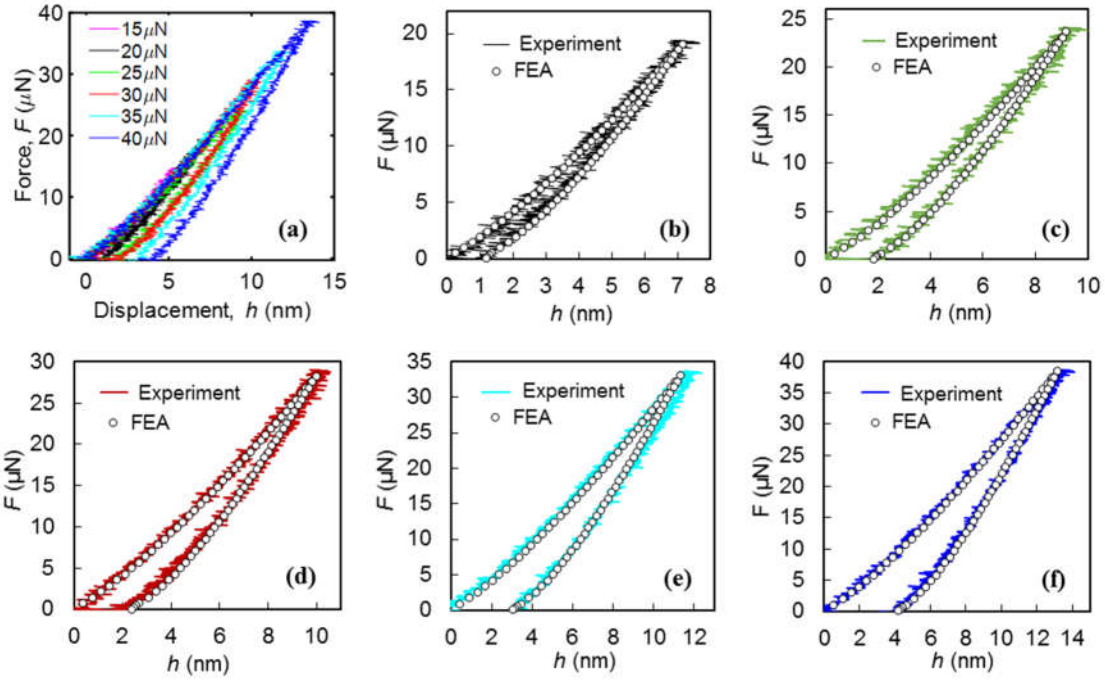

Figure 2.8 (a) Measured force-displacement responses for maximum indentation forces varying from 20μN to 40μN on Fused Quartz. Experimental and FEA simulation comparisons at different peak load values: (b) 20 μN, (c) 25 μN, (d) 30 μN, (e) 35 μN and (f) 40 μN.

Table 2.1 FEA fitting results for elastic moduli and yield strength values for Fused Quartz.

Indentation force, F (μN)	15	20	25	30	35	40	Average	Yu et al. (2004)	Xin and Lambropoulos (2000)
FEA, E (GPa)	72	70	65	68	68	66	68.17	67.60	73.00
FEA, σ_y (GPa)	-	5.0	4.8	5.0	5.0	4.8	4.92	4.30	5.43

2.4.4 Nanomechanical properties of ultrathin films

2.4.4.1 Structure of multilayered sample

A major objective of the present study is to reliably measure the mechanical properties of ultra-thin solid films, using experimental data from conventional nanoindentation techniques. A typical application where such a need exists is magnetic

storage hard disk drives. A schematic cross section of the solid films of a typical magnetic disk in a hard disk drive (HDD) is shown in Fig. 2.9. In this case the magnetic layer for the data storage is 14 nm thick. Above the magnetic layer there is a 2.5 nm thick Carbon Overcoat (COC) to protect the magnetic material and below it there is a thicker 90 nm metal alloy that is used to grow the magnetic material on. Note that with advances of modern HDD technology this disk structure differs from others reported in previous publications (Katta et al., 2010; Ovcharenko et al., 2010).

To perform FE simulations, it is necessary to know the mechanical properties of each layer. In the present work, we use the mechanical properties for the COC, as measured and reported in the literature (Lee et al., 2006), i.e., E=138 GPa and H =14.5 GPa. The yield strength is calculated through a relation for amorphous carbon films reported by Robertson, H=1.8 σ_y (Robertson, 2002). This coefficient correlates well with the finding that elastic materials have H=1.7 σ_y (Cheng and Cheng, 1998), and with calculations using relations proposed by Johnson (1970) (H=1.92 σ_y) and Ye and Komvopoulos (2003) (H=1.98σ_y). The properties of the glass substrate are provided by the vendor: elastic modulus of 80 GPa and yield strength of 3 GPa. The mechanical properties of the magnetic layer and the metal alloy are unknown and will be obtained by the FEA-fitting method.

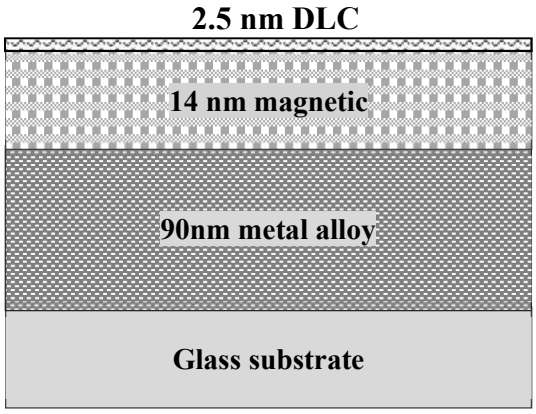

Figure 2.9 Schematic of typical thin layer structure in a typical HDD magnetic disk.

2.4.4.2 FEA results of metal alloy

To extract the mechanical properties of the magnetic layer, it is necessary to first characterize the mechanical properties of the thicker layer below, i.e., the 90 nm thick metal alloy layer. Then the only mechanical properties to be determined would be those of the magnetic layer. To this end, nanoindentation experiments were performed on specially made samples where there was a 90 nm thick metal alloy deposited on the glass substrate and a 2.5 nm thick COC (without the magnetic layer). The measured root-mean-square roughness is 0.2 nm, and the measured elastic modulus and hardness values are shown in Fig. 2.10. To avoid any contribution from the 2.5 nm COC coating, the indentation depth is kept larger than 7 nm. The data shows good consistency and the mean value of the reduced elastic modulus is 112.7 GPa and the mean hardness is 9.82 GPa.

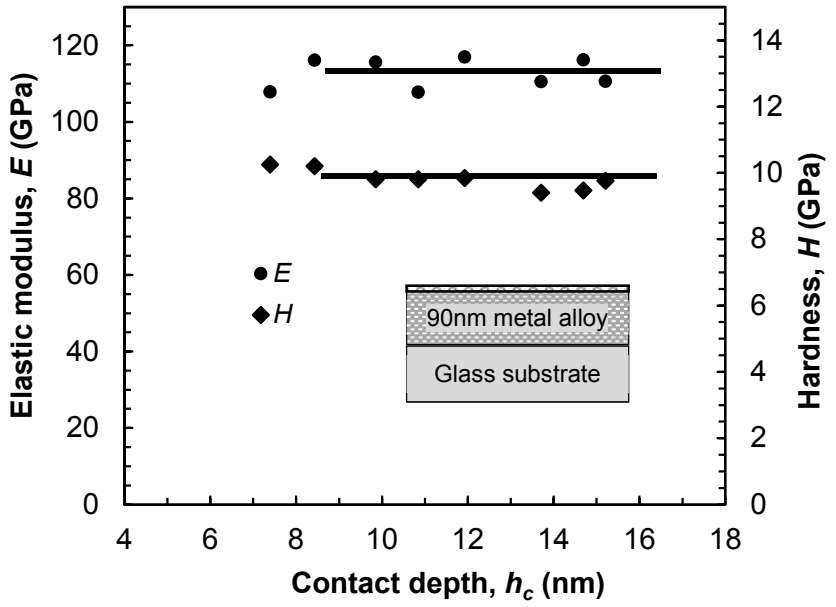

Figure 2.10 Experimental nanoindentation data for elastic modulus and hardness for the metal alloy sample.

The first four nanoindentation experiments were selected for the FEA-fitting method, whose *F*-*h* responses are shown by Fig. 2.11(a). Fig. 2.11(b) to (e) are *F*-*h* responses from the nanoindentation experiments and best FEA-fitting simulations. Note that the maximum displacement of the indenter is 14 nm and is within the spherical part of the indenter depicted in Fig. 2.6. The resulting elastic moduli and yield strength values are listed in Table 2.2. The average elastic modulus is 95.75 GPa and the corresponding reduced modulus is 105.30 GPa, assuming a Poisson's ratio of 0.3. Compared to the nanoindentation data, the reduced modulus using FEA-fitting is slightly lower, as it was the case for the elastic modulus of Fused Quartz, given in Table 2.1.

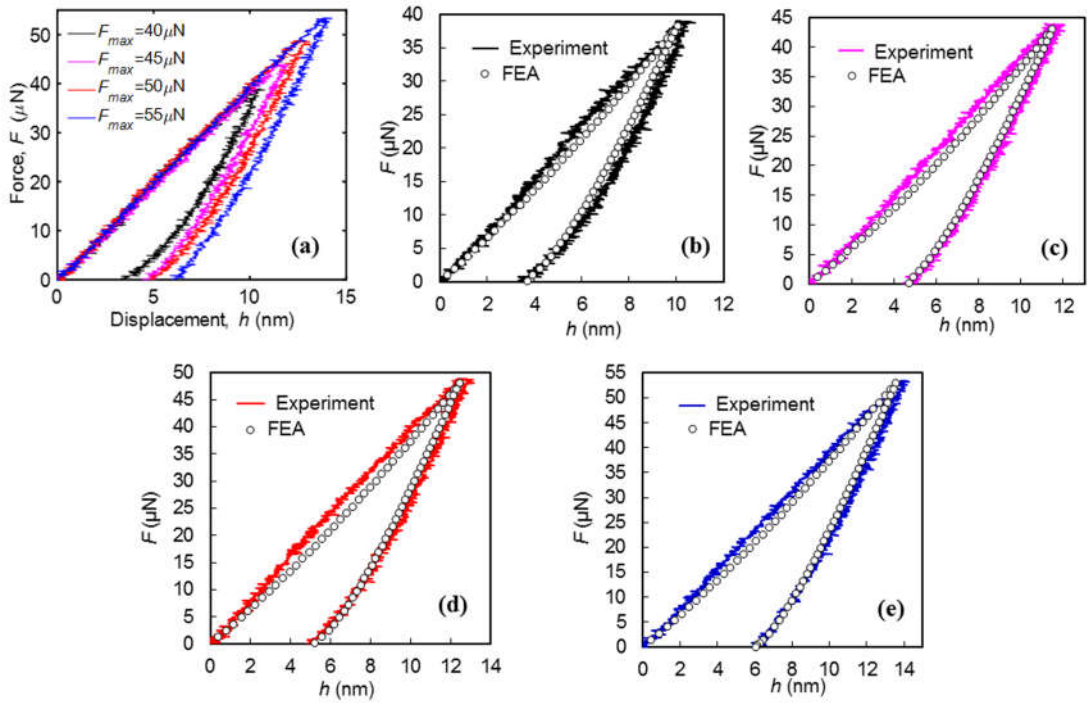

Figure 2.11 Measured force-displacement responses for maximum indentation forces varying from 40μN to 55μN on metal alloy. Experimental and FEA simulation comparisons at different peak load values: (b) 40 μN, (c) 45 μN, (d) 50 μN, and (e) 55 μN.

Table 2.2 FEA fitting results for elastic moduli and yield strength values of the metal alloy layer.

Max indentation force, F (μN)	40	45	50	55	Average	Standard deviation
FEA, E (GPa)	98	95	95	95	95.75	1.30
FEA, σ_y (GPa)	4.8	4.5	4.5	4.5	4.58	0.13

The yield strength of the metal layer obtained in the present study is 4.6 GPa, which is higher than 2.9 GPa for the interlayer material reported by Katta et al. (2010). This is to be expected since the HDD industry is constantly developing new materials with improved mechanical properties, for improved wear-resistant.

Fig. 2.12 (a) and (b) shows a typical image scanned with the same indenter used for the nanoindentation experiment for the case of max indentation force of 40 μN. The maximum residual depth measured with the AFM is 3.18 nm, compared to the actual residual displacement of h_r=3.87 nm, shown in Fig. 2.11(b). The residual depth from the image is generally underestimated since we are using the same tip to indent and measure the topography, which in this case the tip radius is R=85 nm (which is blunt and thus has worse resolution than typical AFM probes with tip radius of R=~10 nm). As seen from the images, there is very limited pile-up in the cross sectional view, indicating that the measurement in Fig. 2.10 is accurate and not affected by any pile-up.

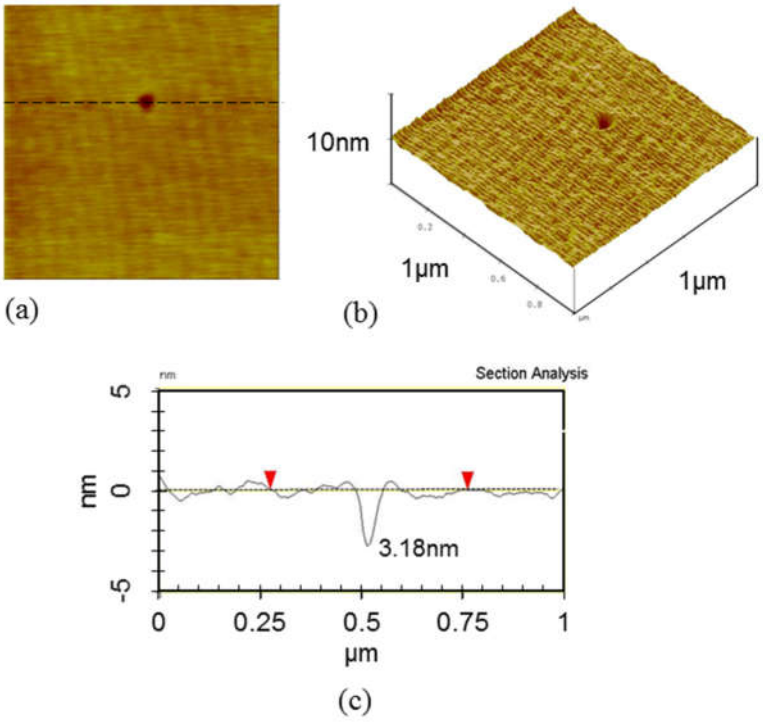

Figure 2.12 Residual images of the metal alloy sample after a maximum indentation force F=40 μN: (a) top view; (b) isomeric view; (c) cross sectional view.

2.4.4.3 FEA results for the magnetic layer

The cross-sectional structure of the disk sample is shown by Fig. 2.9. As introduced previously, the mechanical properties of the COC film and the glass substrate are known. After measuring the mechanical properties of the 90 nm metal layer, the last task is to obtain the mechanical properties of the 14 nm magnetic layer which are of the greatest interest. Firstly, nanoindentation experiments were performed on a full stack HDD sample and the measured elastic modulus and hardness are shown by Fig. 2.13. The reduced elastic modulus decreases gradually from about ~135 GPa to ~120 GPa, from which it can be inferred that the magnetic layer has a higher elastic modulus, i.e., $E_{mag}>E_{metal}$. The measured hardness is almost constant at about 10 GPa and equal to the metal sample, shown in Fig. 2.10. This is because of substrate effects from the metal alloy layer. From Fig. 2.13, it is difficult to clearly identify the mechanical properties of the 14 nm magnetic layer, using existing nanoindentation techniques that preclude reliable measurements at sub-5 nm contact depth experiments. In such situations, the importance of the proposed FEA-fitting method becomes significant as it provides a way to extract the specific layer's mechanical properties.

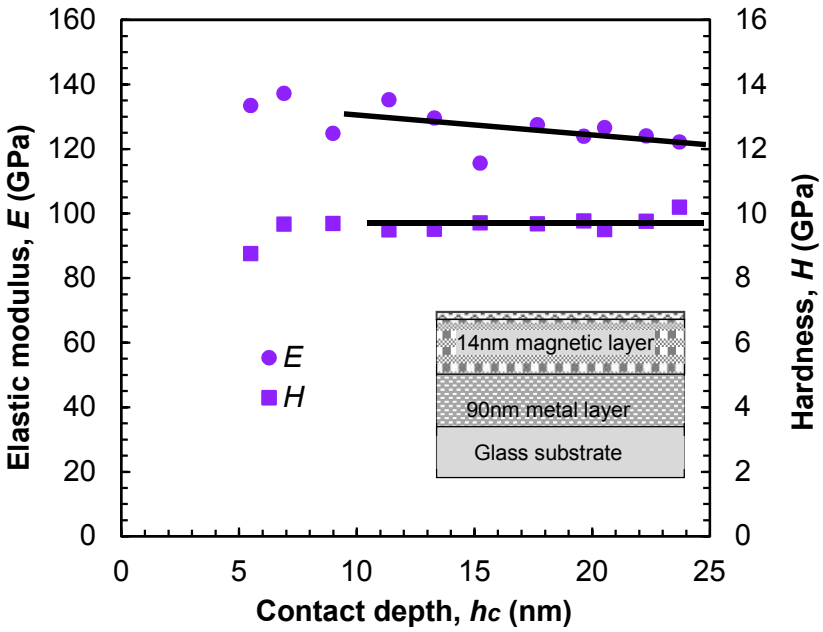

Figure 2.13 Experimental nanoindentation data for reduced elastic modulus and hardness for the full stack sample with magnetic layer.

Fig. 2.14 (a) shows the *F-h* curves from the nanoindentation experiments at maximum loads ranging from 20 to 40 μN and (b) to (f) show the individual peak load experiments with the FEA results. The loading curves overlap, as expected since the experiments are consistent and stable. The peak forces used are very small so as to detect the material behavior of the topmost layers, including the magnetic layer. As the elastic modulus and yield strength of the metal layer have already been measured and shown in Table 2.2, and the Poison's ratio of the magnetic material is taken to be 0.3 (Katta et al., 2010), the parameters to be determined by FEA-fitting are the elastic modulus and yield strength of the magnetic layer.

Fig. 2.14 (b) to (f) show the best-fit *F*-*h* responses for the different peak forces and also compared to the nanoindentation experiments. The best-fit mechanical properties are also listed in Table 2.3. The average elastic modulus is 180 GPa and the average yield strength is 2.92 GPa. Note that the deviation for the elastic modulus is much larger than that of the yield strength. Recall from the previous finding that the elastic moduli of Fused Quartz and the metal layer were underestimated, and we conclude that the current FEA-fit method under predicts the elastic modulus by ~5%, which is reasonable. A potential reason for this is that the elastic modulus determines the slope of the initial part of the unloading curve that is more difficult to fit than the residual depth determined by the yield strength.

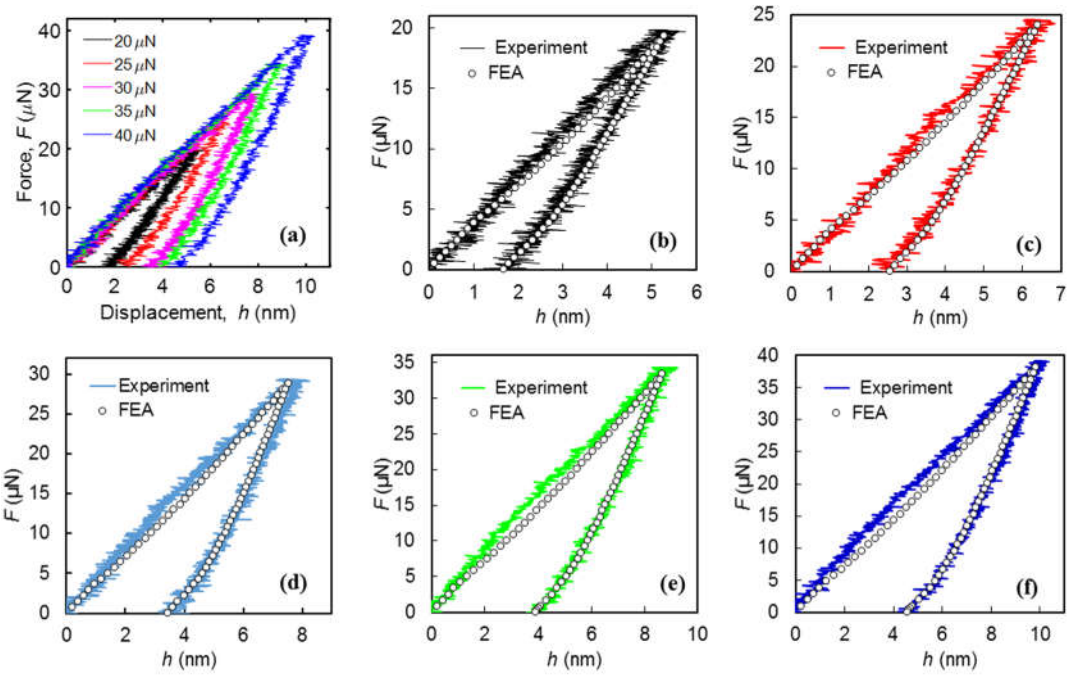

Figure 2.14 (a) Measured force-displacement responses for maximum indentation forces varying from 20 μN to 40 μN on full stack HDD sample. Experimental and FEA simulation comparisons at different peak load values: (b) 20 μN, (c) 25 μN, (d) 30 μN, (e) 35 μN, and (f) 40 μN.

Table 2.3 FEA fitting results for elastic moduli and yield strength values of the magnetic layer.

Indentation force, F (μN)	20	25	30	35	40	Average	Standard deviation
FEA, E (GPa)	150	200	150	200	200	180	24.50
FEA, σ_y (GPa)	3.0	2.8	3.2	2.8	2.8	2.92	0.18

Fig. 2.15 shows a typical 3D AFM image and cross sectional profile of the HDD sample after indented with the 30μN peak force. The residual indent looks round from the top view because of the spherical part on the top of the probe.

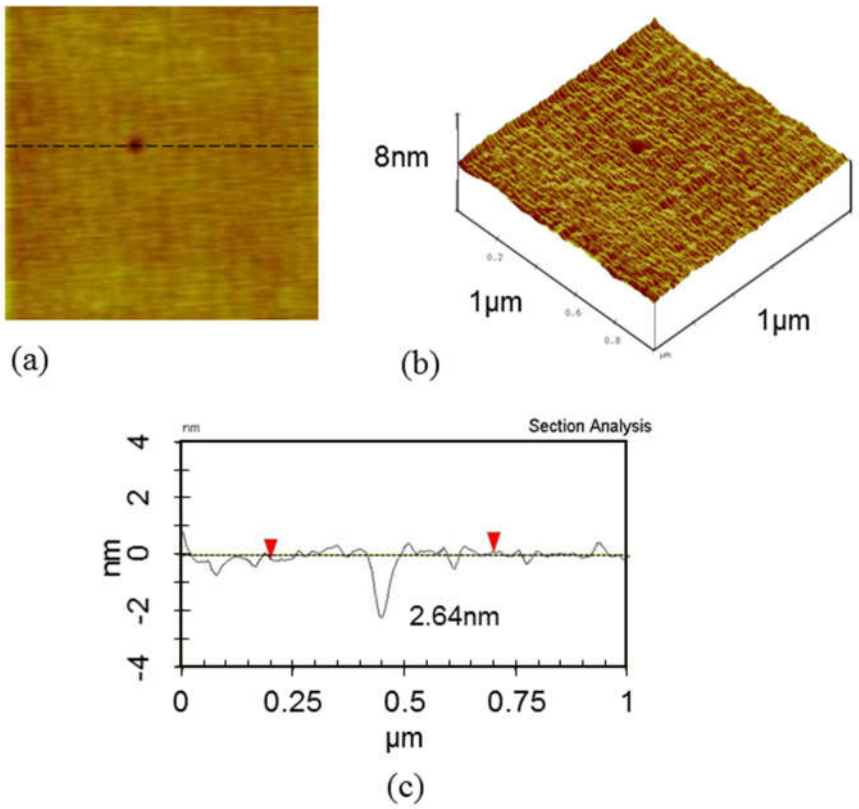

Figure 2.15 Residual images of the full-stack HDD sample after a maximum indentation force F=30 μN: (a) top view; (b) isomeric view; (c) cross sectional profile.

2.4.5 Discussion on the yield strength values by the FEA-fitting method

Different from elastic modulus, yield strength as a fundamental material property, cannot be directly measured from nanoindentation experiments. Normally the yield strength is calculated from hardness through a relationship. Besides the relationship proposed by Tabor (1970), i.e., $H=2.8\sigma_y$, Johnson (1970) proposed a more comprehensive relationship with dependence on indenter geometry and elastic modulus E:

$$\frac{H}{\sigma_y} = \frac{2}{3}\left[1 + ln\left(\frac{1}{3}\frac{E}{\sigma_y}\tan\beta\right)\right], \tag{2.9}$$

where β is the equivalent angle between the indenter and the sample surface plane, 19.7° for Berkovich and 47.7° for 90 degree cube corner tip. Based on FEA simulations, Ye and Komvopoulos (2003) also obtained a relationship for hardness and yield strength:

$$\frac{H}{\sigma_y} = 0.9 + \ln\left(\frac{E}{\sigma_y}\right), 0 < \frac{E}{\sigma_y} < 200. \tag{2.10}$$

In the present work, we investigated the yield strength of three different materials, Fused Quartz, a 90 nm thick metal alloy layer and a 14 nm magnetic layer. The magnetic layer cannot utilize any of the hardness/yield strength relations due to lack of hardness information for such a thin layer (due to instrumentation limitations). For Fused Quartz and the metal layer, mechanical properties including elastic modulus and hardness have been either well recognized or measured from nanoindentation experiments, referring to Tables 2.1 and 2.2. Yield strengths calculated by the different relationships and also as obtained in the present study are shown in Table 2.4. The results in the resent study show good agreement with the three models, which verify that the current FEA-fitting method for shallow nanoindentation is trustworthy in characterizing yield strengths of thin films.

For extremely thin film such as the 14 nm magnetic layer, hardness and elastic modulus are not conclusive and the proposed FEA-fitting method can be used for mechanical property characterization.

Table 2.4 Yield strength values obtained using different models.

Sample	E (GPa)	H (GPa)	σ_y (GPa), Eq. (2.9)	σ_y (GPa), Eq. (2.10)	σ_y (GPa), Present study
Fused Quartz	70.2	9.45	5.29	5.01	4.92
Metal layer	112.7	9.82	4.57	4.71	4.58

Regarding the 14 nm magnetic layer, all above hardness/yield strength relations are not applicable as its elastic modulus and hardness are inconclusive from nanoindentation experiments. Even using an extremely sensitive transducer (Yu et al., 2005), it is difficult to directly measure the mechanical properties of the magnetic layer in a multilayered HDD sample, referring to the nanoindentation data by Katta et al. (2010). Present work relies on nanoindentation experiments and FEM and finds conclusive mechanical properties of the magnetic layer, shown in Table 2.3. The obtained elastic modulus shows more variation compared to the yield strength. Note that the present study utilizes a conventional nanoindentation and indenter system, which is appealing as they are readily available. In the future work, a sharper indenter and a more sensitive transducer will be used, and there will be better resolution for loading- unloading curves and thus present FEA-fitting method can achieve better accuracy.

2.5 Summary of Chapter 2

Shallow sub-20 nm nanoindentation measurements are challenging because the Oliver-Pharr method needs correction at contact depths h_c <5nm, and for very thin multilayered samples, measurements are not conclusive due to layer/substrate effects. The present study addresses these two issues with the aid of FEM. Through FE simulation of the nanoindentation on a standard Fused Quartz sample, the present study found that a blunt tip model is more realistic and able to match with nanoindentation experiments. The bluntness can be characterized simply by fitting an elastic punch. Compared to previous FE simulations for nanoindentation, the contact depth in the present study is shallower and thus the tip bluntness effect is significant and cannot be ignored. The blunt tip model is used to measure the mechanical properties of three different materials, and the results are summarized below:

(a) The blunt tip model is first validated on a bulk Fused Quartz standard material using FEA-fitting with nanoindentation experiments at different loads. The average yield strength value is 4.92 GPa, which correlates well with data reported in the literature (Yu et al., 2004; Xin and Lambropoulos, 2000) and also with the hardness/yield strength models by Johnson (1970) and Ye and Komvopoulos (2003).

(b) The proposed model is then applied to a 90 nm thick solid film (metal alloy) sandwiched between a thin DLC coating and a glass substrate. The model gives an elastic modulus of 95.75 GPa and a yield strength of 4.58 GPa, which also agree well with values by the two hardness/yield strength models.

(c) Finally, the model is applied to measure the mechanical properties of a 14 nm thick magnetic layer sandwiched between a DLC and the 90 nm thick metal alloy layer that cannot be directly measured using current state-of-art instrumentation. The magnetic layer properties were found to be: reduced modulus 180 GPa and yield strength 2.92 GPa.

As shown in (c) above, the primary objective of the proposed work is to accurately measure the mechanical properties of ultrathin films (sub-20 nm) from force-displacement responses of shallow nanoindentation experiments, using conventional techniques. Despite the advantages of the proposed method, there are two areas that need further improvement: first is that the obtained elastic moduli values are underestimated by ~5% compared to the direct measured data; second potential issue is that the present approach assumes elastic-perfectly plastic material properties, which even though is justified for the materials used in this work, it may not be the case for other material systems, and the model should be modified to include strain hardening behavior.

3 A MICROELECTROMECHANICAL (MEMS) FORCE-DISPLACEMENT TRANSDUCER FOR SUB-5 NM NANOINDENTATION

3.1 Introduction to nano-mechancal instruments

The present chapter presents a highly sensitive force-displacement transducer capable of performing ultra-shallow nanoindentation and adhesion measurements. The transducer utilizes electrostatic actuation and capacitive sensing combined with MEMS fabrication technologies. Air indentation experiments report a root-mean-square (RMS) force resolution of 1.8 nN and a RMS displacement resolution of 0.019 nm. Nanoindentation experiments on a standard Fused Quartz sample report a practical RMS force resolution of 5 nN and a RMS displacement resolution of 0.05 nm at sub-10 nm indentation depths, indicating that the system has a very low system noise for indentation experiments. The high sensitivity and low noises enable the transducer to be capable of obtaining high-resolution nanoindentation data at sub-5 nm contact depths. The sensitive force transducer is also used to perform adhesion measurements, clearly capturing the pull-on and pull-off forces during approach and separation of two contacting surfaces.

In nanoindentation experiments, a rigid indenter made of a very hard material (usually diamond) is pressed into a test sample with either controlled load or controlled displacement, and then withdrawn from the sample. During indentation experiments, a transducer measures the in-situ force and displacement responses that compose direct load-displacement measurements or loading-unloading curves. The hardness of the sample is calculated by dividing the load with the contact area, and the reduced elastic

modulus is calculated from the unloading stiffness using the Oliver-Pharr method (Oliver and Pharr, 1992). The nanoindentation technique has become the most widely used means to measure mechanical properties of solids, especially thin films and coatings in miniature devices (Li et al., 2003; Espinosa et al., 2003; Lee et al., 2007). An emerging application of nanoindentation is to combine it with Transmission Electron Microscopy (TEM) and Scanning Electron Microscopy (SEM) for in-situ nanomechanical testing (Minor et al., 2001; De Hosson et al., 2006; Lee et al., 2013; Zhu and Espinosa, 2005; Maschmann et al., 2011; Warren et al., 2010).

Several industries have been striving to develop products with better capabilities and smaller size. This usually comes along with the employment of thinner films achieved by more advanced thin-film deposition and processing techniques. Performing nanoindentation measurements on such thin films is challenging and it is necessary to develop more sensitive nanomechanical transducers. For instance, in order to obtain lower head-media spacing and thus higher areal density, the magnetic storage industry has reportedly reduced the thickness of diamond-like carbon (DLC) coatings on top of the media from ~20 nm in 1999 (Mate and Homola, 1998) to ~3 nm in 2014 (Marchon et al., 2014). According to the literature and ISO standards (Lucca et al., 2010), the maximum permissible error for depth sensing nanoindentation (contact depth, h_c <200 nm) should be less than 1% of the maximum indentation depth. That is, without consideration of substrate effects, the displacement resolution for measuring the 3 nm thick DLC coating in magnetic storage has to be less than ~0.03 nm, which is practically impossible with current technology.

Earlier commercial nanoindentation instruments had a force resolution of 100 nN and displacement resolution of 0.2 nm (Asif et al., 1999). Yu et al. (2005) developed a sensitive nanoindentation transducer attached to a multimode Atomic Force Microscope (AFM) (Yu et al. 2005). They managed to improve the force and displacement resolutions by reducing the transducer moving mass and improving the electronic circuitry. Their calibration data reported a force resolution of ~3 nN and a displacement resolution of 0.05 nm, which was a significant improvement, compared to state-of-the-art nanoindentation instruments.

Gao et al. (2010) presented a MEMS-based force instrument that employs an electrostatic comb-drive to generate the actuation force. Compared to previous traditional systems, the MEMS-based system reports a low force resolution of 1~2.5 nN, and a displacement sensing resolution of ~0.2 nm, which is not sufficiently low for sub-10 nm nanoindentation measurements. The transducer introduced in the present study combines MEMS fabrication technology with an advanced displacement sensing system (Oh et al., 2012; Warren et al. 2013). The MEMS transducer includes two micromachined comb drives comprising a number of capacitive pairs configured to drive the probe and sense the displacement.

To quantify the performance of the transducer under nanoindentation experiments, the present study performed both air-indentation experiments and light load calibration experiments on a Fused Quartz standard sample. The two experiments demonstrate out-of-contact and in-contact noise levels. Comparisons with two state-of-the-art nanoindentation instruments show that the present transducer has lower RMS force and

displacement noise levels. The present transducer also demonstrates its capability of measuring very low adhesive forces that cannot be measured using conventional instrumentation.

3.2 Instrumentation

3.2.1 Conventional force transducer

Capacitive transducers are widely used in nanoindentation systems. Fig. 3.1 shows a schematic of a conventional nanoindentation capacitive transducer that utilizes a parallel plate actuator (PPA). The PPA has two fixed drive electrode plates and a movable pick-up electrode plate that is connected with the indentation probe. The capacitance between the two electrode plates is:

$$C = \frac{\varepsilon_r \varepsilon_0 A}{d} \tag{3.1}$$

, where ε_r is the relative permittivity of the medium between the plate electrodes and ε_0 is the permittivity in vacuum, A is the overlapping area and d is the relative distance between the two plates. The energy stored in the PPA capacitor is:

$$E_c = \frac{CV^2}{2} = \frac{\varepsilon_r \varepsilon_0 A V^2}{2d} \tag{3.2}$$

, where V is the applied voltage. The resultant actuation electrostatic force is:

$$F = \frac{\varepsilon_r \varepsilon_0 A V^2}{2d^2} = E_f V^2 \tag{3.3}$$

, where E_f is the electrostatic force constant. The actuation force moves the probe toward the sample and the moving distance is determined by the change in capacitance due to the displacement of the pick-up electrode relative to the two drive electrodes.

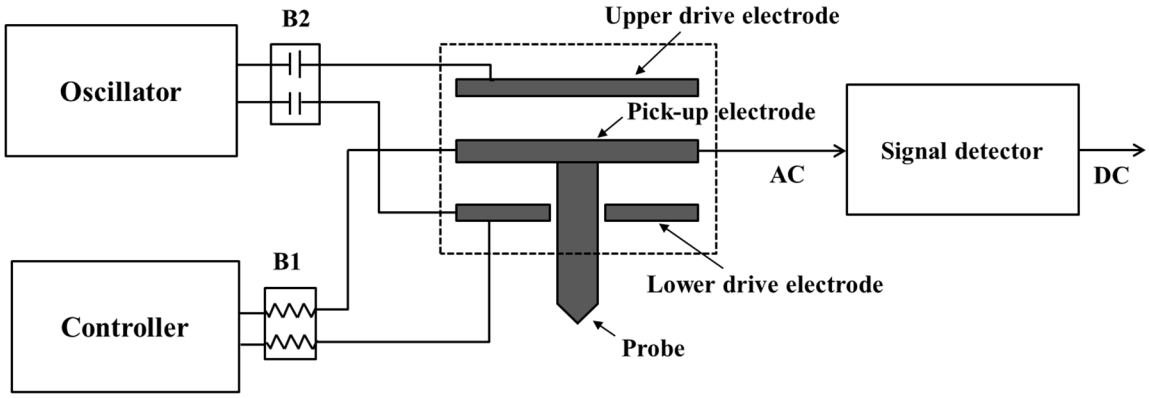

Figure 3.1 Schematic of a conventional transducer for nanoindentation using electrostatic actuation and capacitive displacement sensing.

As depicted in Fig. 3.1, the controller applies a voltage between the middle pick-up electrode and the lower drive electrode to actuate an attractive electrostatic force between the two plates. Then, the probe is pressed towards the sample surface to make an indentation. The oscillator connected on the two drive electrodes has two output AC modulation signals applied to the two drive electrodes. The two modulation signals have a phase difference of 180 electrical degrees and the center electrode picks up both signals. The sensed oscillation signals are demodulated into DC voltages and the difference in sensed signals are detected through a differential amplifier. When the pick-up electrode is at the center position between the two drive electrodes, the two capacitances are equal and thus the same magnitude of signals with 180 degrees out of phase are detected by the pick-up electrode and the differential voltage output becomes zero. As the pick-up electrode moves towards one of the electrodes in accordance with movement of the probe, the differential capacitance between the pick-up electrode and the upper/lower drive

electrodes proportionally increases and the differential DC output increases as well. The voltage of the DC signal represents the nanoindentation displacement.

The design of the force transducer has an inherent non-linearity because the capacitance between the electrode plates varies with the reciprocal of the spacing, given by Eqn. (3.1). For the transducer shown in Fig. 3.1 that has a movable center electrode and two outer fixed electrodes, this non-linearity in voltage output relative to the displacement is typically large for large displacement movement, so the transducer is used only for small displacement that shows linear voltage output relative to the displacement. Yu et al. improved the electronic circuitry and thus reduced electronic noise, and also reduced substantially the moving mass of the center plate and probe by using a hollow rotor plate (Yu et al. 2005).

3.2.2 MEMS-based force transducer

The present work focuses on improvements of the force transducer by using MEMS fabrication, while the electrical circuitry remains as in the conventional system. In the MEMS-based transducer shown schematically in Fig. 3.2, there are two micromachined comb drives separated by springs. One is movable and integrated with the probe and the other is fixed. Both combs have multiple fingers such that the transducer is composed of multiple sets of PPAs. Assuming there are N fingers on the movable comb drive, then there are N sets of PPAs and each of them has a similar design as the conventional system.

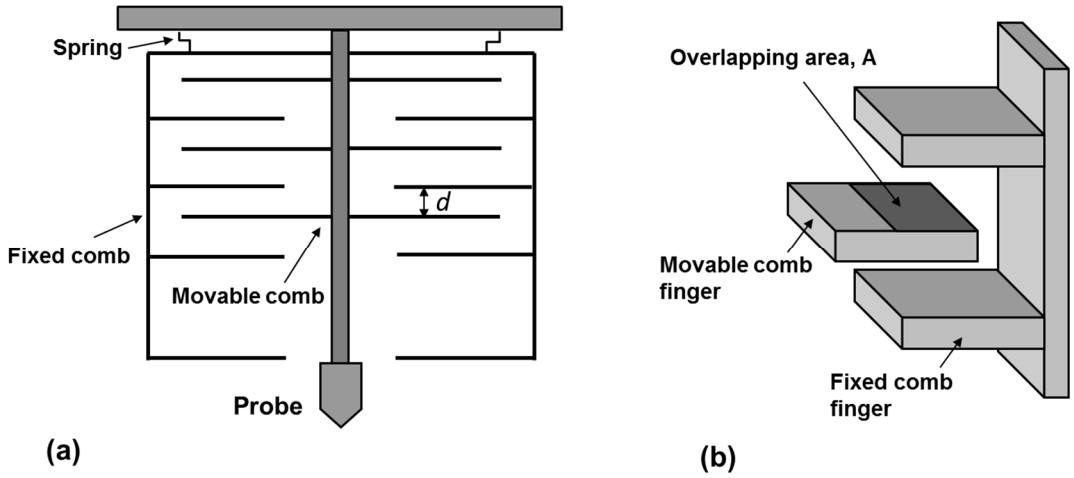

Figure 3.2 Schematic of MEMS-based force transducer showing the comb-drive actuator: (a) movable and fixed comb capacitors; (b) comb fingers and the overlapping area.

Similar to the conventional system, the MEMS transducer actuates the force electrostatically and senses the displacement from capacitive change. To generate a force, a voltage is applied on the fixed comb, resulting in a small voltage difference V between the two neighboring fingers. Referring to Eqn. (3.3), the total electrostatic actuation force is (Oh et al. 2012):

$$F = \frac{N\varepsilon_r\varepsilon_0 AV^2}{2d^2}. \tag{3.4}$$

The displacement sensing also relies on the change of capacitance due to the relative displacement of the movable comb with respect to the fixed comb. Compared to the conventional transducer, the MEMS transduce features a much smaller spacing between the electrode plates. To generate the same amount of actuation force, it requires much less voltage and thus makes the actuation more sensitive. The small spacing between the electrodes also enables high sensitivity for displacement sensing.

Fig. 3.3 shows photographs of the MEMS transducer. The transducer is packaged within a 0.3 mm thick cover made of low-resistivity silicon. The cover protects the transducer from contamination and offers electrical shielding to minimize parasitic capacitance and noise. The overall transducer is assembled on an epoxy frame that is fixed to the scanner.

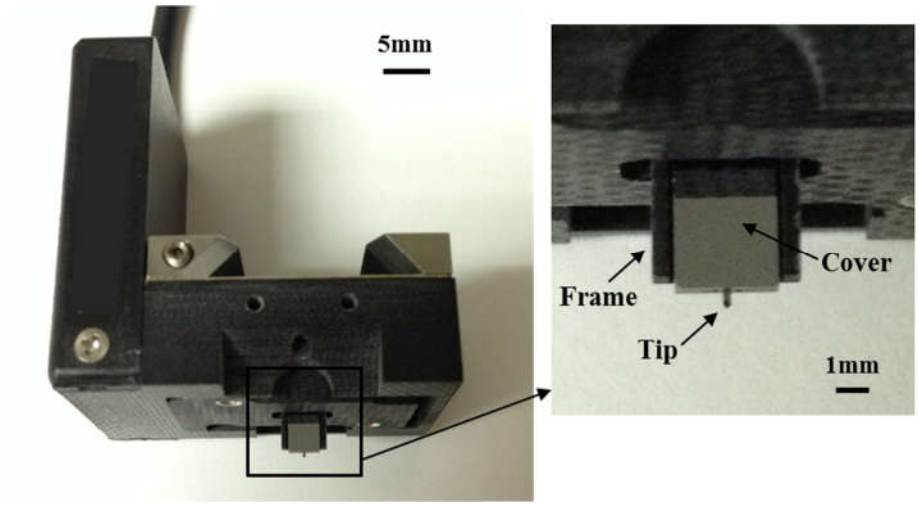

Figure 3.3 Photographs of the MEMS-based transducer and the tip.

3.2.3 Comparison of moving mass

Both conventional and MEMS-based transducers have springs to suspend the movable electrodes. The actuation force applied on the plates should be sufficiently light to make sure it is linear with distance: $F_{spring} = kz$. The indentation force or reaction force from contact between the probe and the sample is given by:

$$F_{indention} = F_{actuation} - F_{spring}. \tag{3.5}$$

The equation of motion for the system in dynamic equilibrium can be expressed as:

$$F_{spring} = m\ddot{z} + c\dot{z} + kz + \left(m\ddot{\delta} + c\dot{\delta} + k\delta\right), \tag{3.6}$$

where m is the moving mass of the indenter, z is the indentation displacement, c is the damping coefficient, k is the spring constant, and δ is the vibration or noise of the displacement. Substitution of Eqn. (3.6) into Eqn. (3.5) yields:

$$F_{indention} = F_{actuation} - (m\ddot{z} + c\dot{z} + kz) - \left(m\ddot{\delta} + c\dot{\delta} + k\delta\right). \tag{3.7}$$

Usually the indentation process is quasi-static and thus $m\ddot{z} + c\dot{z} \approx 0$, so Eqn. (3.7) reduces to:

$$F_{indention} = F_{actuation} - kz - \left(m\ddot{\delta} + c\dot{\delta} + k\delta\right). \tag{3.8}$$

A desirable force actuation system should be able to minimize the difference between the input actuation force $F_{actuation}$ and the output indentation force $F_{indentation}$. Therefore, according to Eqn. (3.8), it is necessary to make $kz + m\ddot{\delta} + c\dot{\delta} + k\delta$ as small as possible, which provides direction for improving the system.

A reduced moving mass can clearly decrease the noise term due to acceleration, $m\ddot{\delta}$ in Eqn. (3.8). The mass here refers to the moving mass that includes the movable electrode plates, any circuits attached to the moving parts, and the probe. The exact mass can be measured by the transducer itself using tare check. The tare check displays the tare value (or mass) of the transducer that is measured by the system from the rest position of the middle fixed plate. Tare check is allowed only when the system is not performing a test or in contact with a sample surface. For comparison, Table 3.1 shows the moving mass of different nanoindentation force transducers. The Triboscope®, TI Premier® standard

and Nanodyne® transducers were all installed with a diamond cube corner probe weighing ~22 mg. The present MEMS-based transducer integrates the probe together with the transducer. Unlike the other instruments, it does not require a separate probe and holder, thus enabling an extremely low moving mass. Note that a disadvantage of the MEMS force transducer is that once the probe tip is damaged, it renders the transducer inoperable. Compared with existing transducers, the present MEMS-based transducer mass is only 5 mg, which significantly increase the dynamic bandwidth of the transducer operation and reduces the force noise.

Table 3.1 Moving masses of different nanoindentation force transducers with probe

Transducer	Triboscope	TI Premier standard	Nanodyne	MEMS-based
Indenter/moving mass, m (mg)	331	225	52	5

3.3 Results and discussion

The practical measurement accuracy of nanoindentation systems depends on systematic measurement errors of the force generation and depth sensing, as well as drift rates. Usually air-indentation experiments are performed to evaluate the force and displacement noise levels, which are typically reported for each instrument. However, such measurements do not provide information on the practical force and displacement noise levels during actual indentation or adhesion experiments, which are typically higher. In this work, we first conduct air-indentation noise experiments, then low load indentation experiments, and adhesion experiments on a standard Fused Quartz sample.

3.3.1 Air-indentation noise measurements

The noise experiments were carried out by setting the load to zero and holding it for a specified time period; thus measuring the noise due to internal electronic noise and external mechanical vibrations. Fig. 4 shows a typical noise experiment using the standard transducer in a state-of-the-art TI Premier (Hysitron) as well as the MEMS-based transducer. Both transducers were tested for 20 s. It is clearly seen that the MEMS-based transducer shows less scattered force and displacement noise, compared to the TI standard transducer. Both measurements were performed using a commercially available passive vibration isolation table in a standard laboratory under ambient environmental conditions.

To quantify the noise level, it is necessary to clarify the term "resolution" that is used in this work. In the present study, we follow ISO 5725 Standard on Accuracy (Trueness and Precision of Measurement Methods and Results) that defines precision as the standard deviation σ (RMS value) of the measurement data (Fleming, 2013). The definition assumes that the random noise is approximately Gaussian distributed and thus there is a 99.7% probability that any data falls within ± 3σ.

$$\sigma = \sqrt{\sum_1^N (x_i - \bar{x})^2 / N} \tag{3.9}$$

where $\bar{x}$ is the mean value and N is the number of data points.

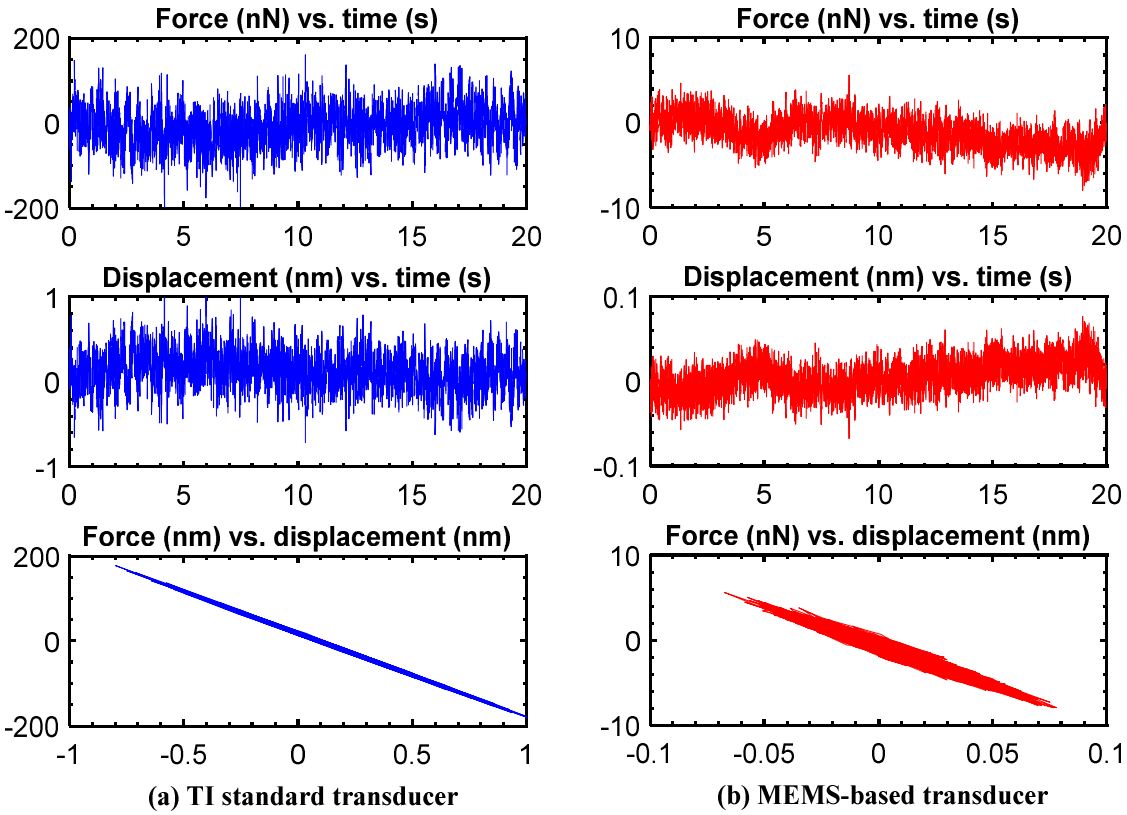

Figure 3.4 Experimental in-situ force and displacement noise data: (a) TI standard transducer, (b) MEMS-based transducer. Note the different scales used.

Fig. 3.5 displays the force and displacement RMS resolution values of the TI standard and the MEMS-based transducers for test time durations varying from 5 s to 40 s. The TI standard transducer reports a force resolution of 45 nN while the MEMS-based transducer reports a significantly lower force resolution of 1.8 nN (25× improvement). Similarly, the TI transducer's displacement resolution is 0.23 nm, compared to 0.019 nm for the MEMS transducer (12× improvement). Note that the resolution values of the present transducer (1.8 nN, 0.019 nm) are lower than the values reported by Yu et al. (2005) by a factor of about 2 (3 nN, 0.05 nm).

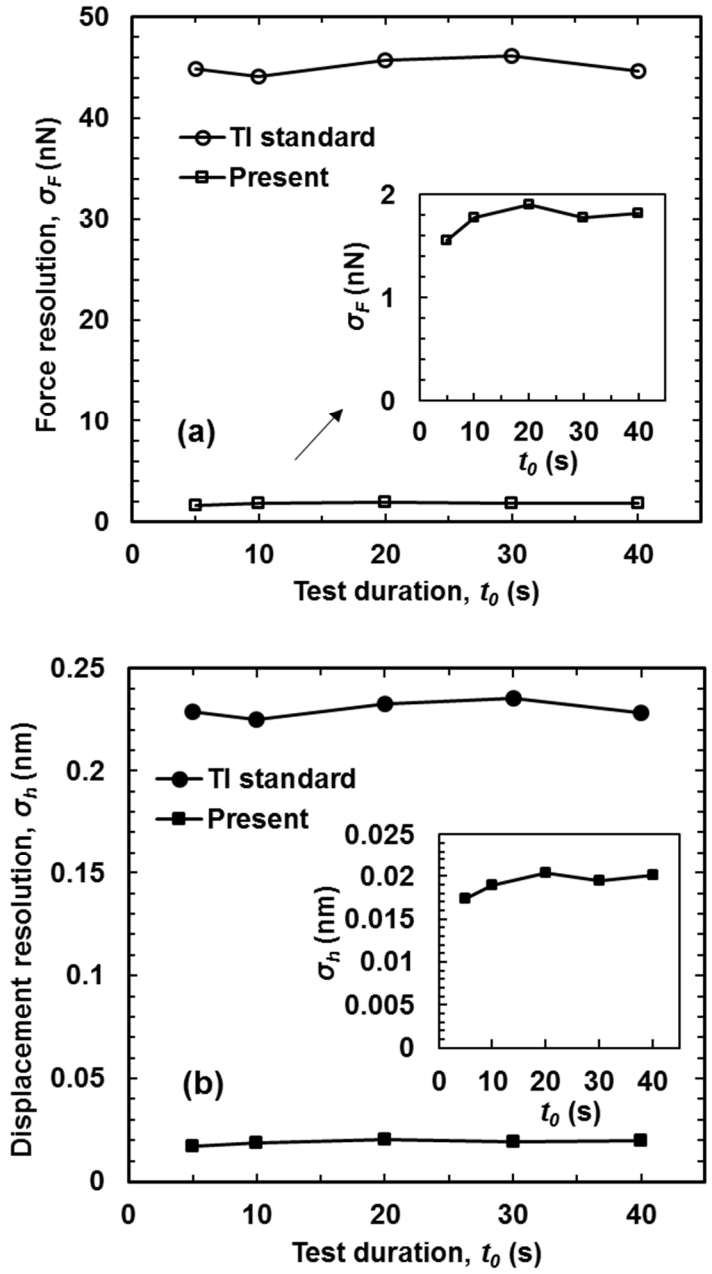

Figure 3.5 (a) RMS force resolution and (b) RMS displacement resolution of conventional (TI standard) and MEMS-based (Present) transducers. Insets show close-ups of the resolutions of the MEMS transducer.

As it was stated, the above force and displacement resolutions are measured from air indentation experiments, where the indenter does not contact the test sample. In regards

to realistic nanoindentation or adhesion/contact experiments, additional vibrations are introduced when the indenter is contacting with the sample and thus force and displacement noise values are typically higher. For example, Yu et al. (2005) showed that their transducer had more than 3 times worse force resolution and 2 times worse displacement resolution when in contact. We will investigate these values for the present transducer in the next section.

3.3.2 In-contact force and displacement resolution

Fig. 3.6 plots loading-unloading curves on a Fused Quartz standard sample using the TI standard transducer and the MEMS transducer. Both transducers are equipped with very sharp cube corner probes with similar tip radii of about 50 nm. The maximum load is 10 μN and it causes a plastic deformation of 2 nm. At such small peak load and displacement, the unloading curve easily mixes with the loading curve if the resolution is not sufficiently low, as is the case for the TI standard transducer. The MEMS-based transducer is capable of providing much clearer identification of the unloading curve because of its higher resolution. No filtering was applied in these measurements.

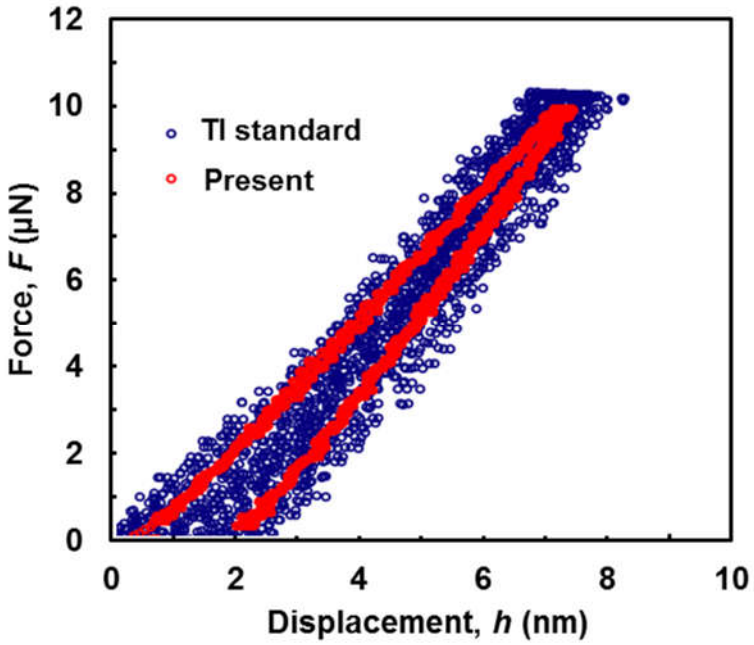

Figure 3.6 Comparison of nanoindentation force-displacement curves at a maximum load of 10 μN.

To quantitatively compare the resolution values during experiments, we performed low load nanoindentation experiments on Fused Quartz using a trapezoidal load function. The loading and unloading steps last 5 s and the holding step at the maximum force lasts 2 s. Fig. 7 shows a typical low load nanoindentation experiment (maximum load of 1 μN). Both force and displacement remain constant during the holding step (i.e., do not exhibit any creep) from which we can calculate the force and displacement resolutions. The data acquisition rate is 500 s^{-1}, resulting in 1000 data points, from which the resolution is calculated by Eqn. (3.9).

Nanoindentation experiments were performed with the maximum indentation load varying from 1 to 40 μN. The loading-unloading curves for the 1 μN load is shown in Fig. 3.7(c), and such a light load leads to a contact depth of 0.5 nm. Despite the very low

nanoindentation experiment, the MEMS-based transducer is sufficiently sensitive to clearly distinguish the loading and unloading curves.

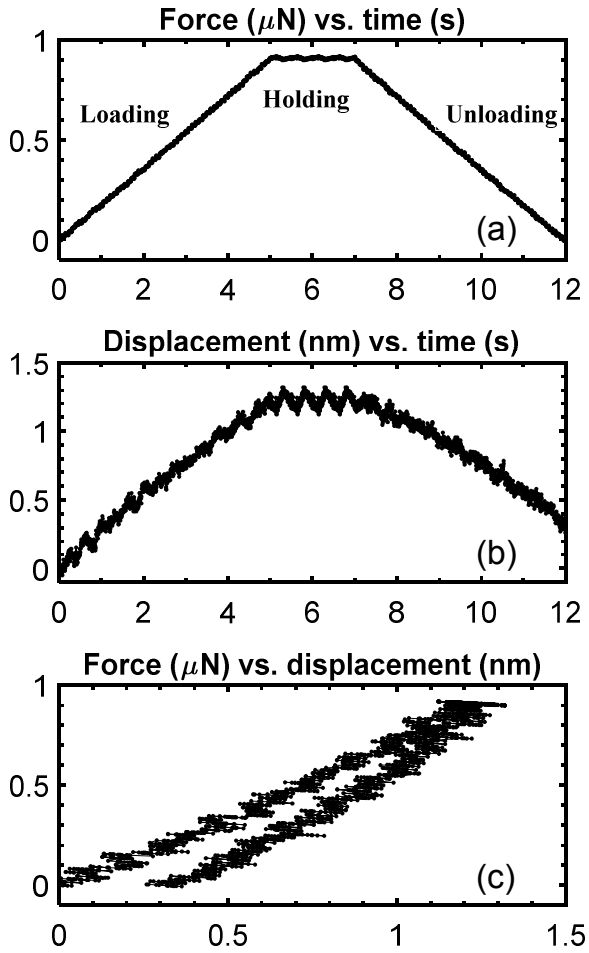

Figure 3.7 (a) In-situ force versus time, (b) in-situ displacement versus time, and (c) force-displacement curve for an extremely shallow (1 μN) nanoindentation experiment on Fused Quartz using the MEM transducer.

Fig. 3.8 (a) and (b) compare RMS force and displacement resolutions using the present MEMS-based transducer and the Nanodyne transducer, Yu et al. (2005) Note that the zero load data point corresponds to the air indentation data. The two transducers show

similar force resolutions for air indentation (~2.5 nN). However, when in contact with the sample, the noise of the transducer by Yu et al. increases with the applied load and reports a resolution of ~20 nN at an indentation load of 40 μN. The MEMS transducer reports a force resolution of 5 nN when in contact and remains almost constant with increasing indentation load.

Regarding the displacement resolution, the transducer by Yu et al. (2005) reported a resolution of 0.05 nm for air indentation and it increased to 0.11 nm for in-contact experiments. The present transducer's resolution remains in the range of 0.045 to 0.06 nm, which is lower than that of Yu et al. (2005).

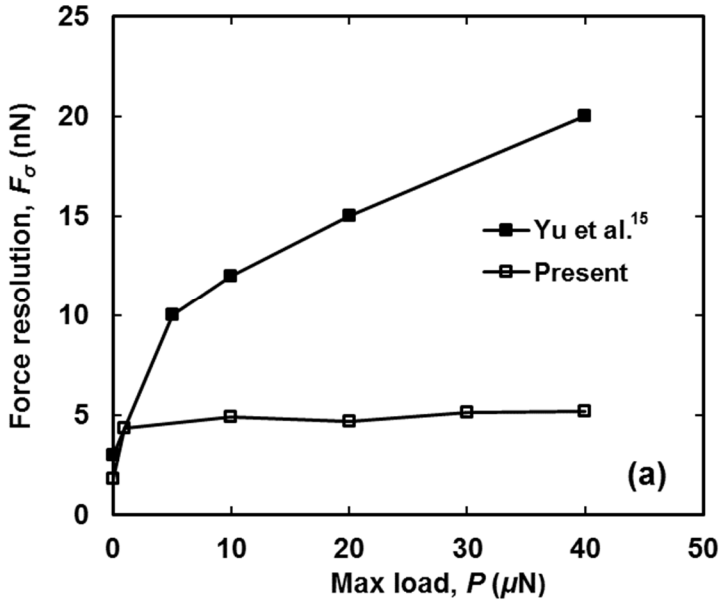

Figure 3.8 Comparisons of force and displacement resolutions during holding steps at different peak indentation loads: (a) load resolution (b) displacement resolution.

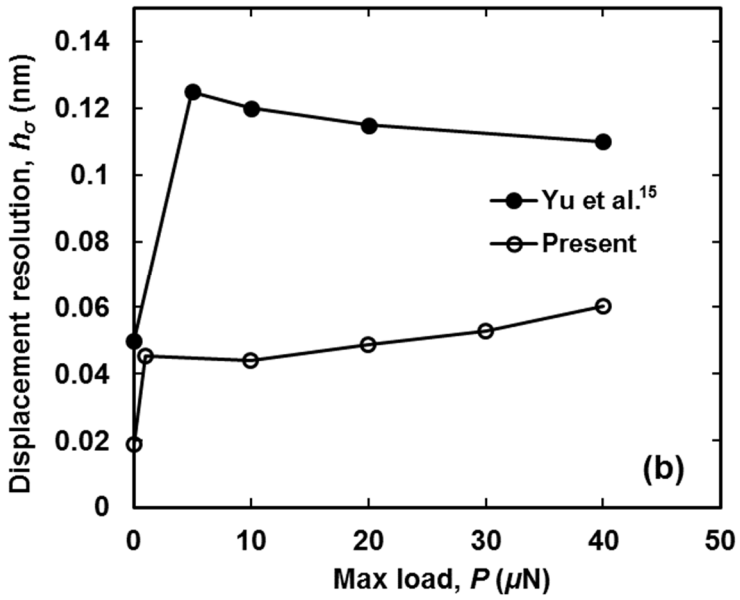

Fig. 3.8 Continued.

Fig. 3.9 shows the extracted nanomechanical properties of the Fused Quartz sample, based on the shallow nanoindentation experiments presented above. The reference mechanical properties for the Fused Quartz (that has no known oxide or hydration layers) are 69.6±5% GPa for the reduced modulus and 9.8±10% for the hardness. Using the MEMS-based force transducer, accurate reduced modulus of elasticity measurements to a minimum contact depth h_c=0.7 nm could be obtained. For hardness measurements, accuracy can be ensured to a minimum contact depth of h_c=2 nm. At contact depth less than 2 nm, the material does not exhibit full plastic deformation, using a tip probe of 47 nm radius. Thus, the measured property is the mean contact pressure and not the intrinsic hardness value, as addressed by Tabor (1956). Yeo and Polycarpou (2007) proposed a correction method to remove the elastic deformation in such shallow regimes and enable the extraction of intrinsic hardness properties.

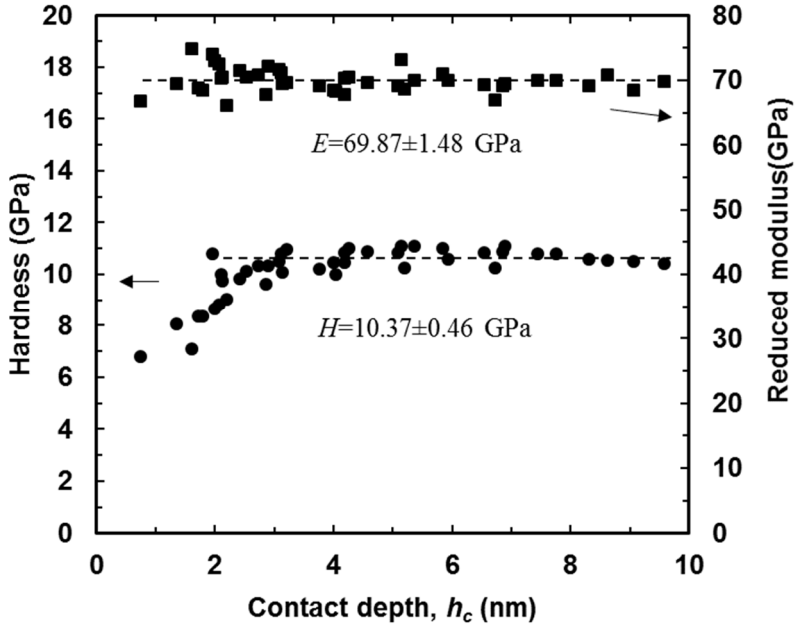

Figure 3.9 Measured nanomechanical properties of Fused Quartz using the MEMS transducer.

3.3.3 Drift rates

The drift rate is another critical measurement parameter to evaluate the performance of a nanomechanical system. Especially for shallow nanoindentation measurements, a low drift rate is essential to ensure measurement accuracy. Both internal electrical noise and external mechanical vibrations contribute to the drift rate. In the present study, we measured the variation of drift rates by the TI standard and MEMS transducers on the Fused Quartz sample, and the results are shown in Fig. 3.10.

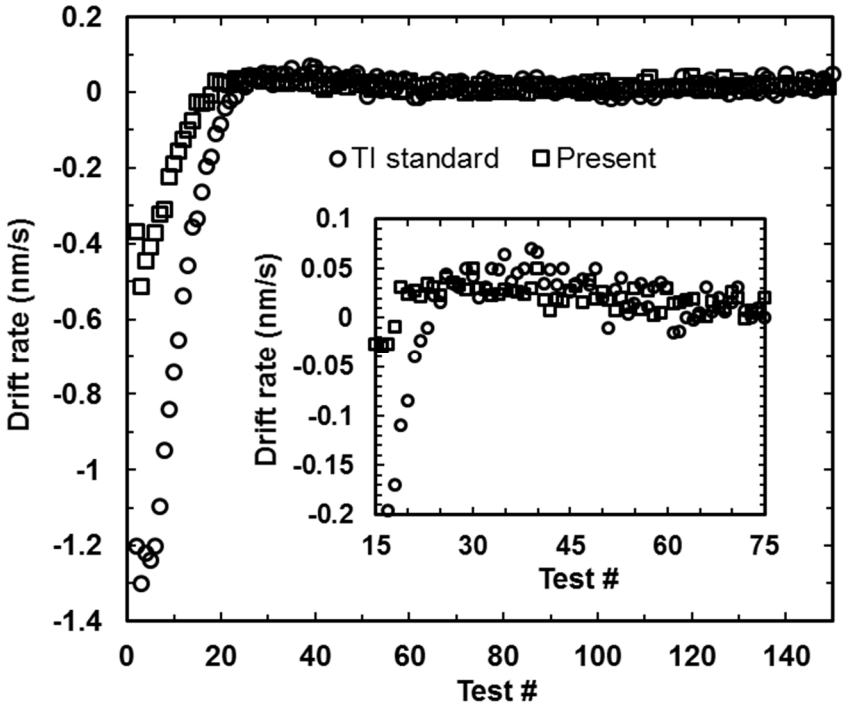

Figure 3.10 Experimental drift rates for indentation experiments on Fused Quartz sample.

Each transducer was used to perform 150 indentation experiments on the same day using the same load function. The time duration between every two nanoindentation experiments is 3 mins. At the beginning of an indentation experiment, both drift rates are high because of temperature differences between the probe and the sample surface or residual vibrations at the beginning of contact. The MEMS transducer begins from -0.5 nm/s, while the TI standard transducer begins from a higher drift rate of -1.3 nm/s. After 10 experiments (30 minutes), the drift rate of the MEMS transducer decreases to -0.19 nm/s, comparing to -0.75 nm/s of the TI Premier transducer. After 20 experiments (60 minutes), the drift rate of the MEMS transducer begins to stabilize and the average absolute value is stable at 0.0172 nm/s (standard deviation of 0.0108 nm/s). It takes about

30 tests for the TI Premier transducer to stabilize and the average absolute values afterwards is 0.0204 nm/s (standard deviation of 0.0161 nm/s). From these comparisons, we can conclude that the MEMS transducer reaches stable drift rates earlier and also has a smaller drift rate with less fluctuation.

3.4 Shallow nanoindentation on 11 nm DLC coating

Fig. 3.11 shows a loading-unloading curve from measurement on a 11-nm DLC coating, using the MEMS transducer developed in this chapter. The maximum indentation depth is about 1.6 nm and the residual depth is about 0.3 nm. The contact depth h_c is about 0.8 nm. Under such small contact force and depth, the transducer still is able to obtain high-resolution force-displacement used for analysis.

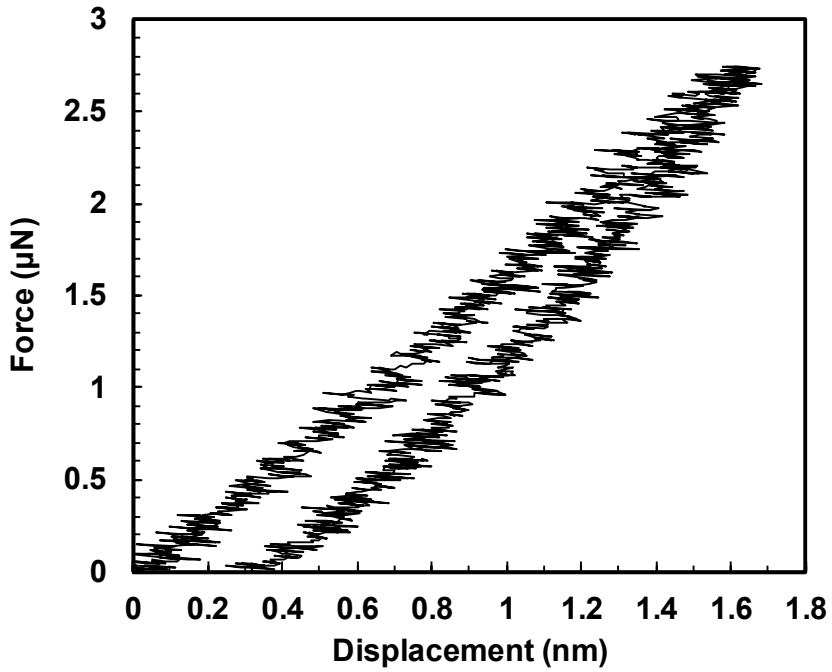

Figure 3.11 Load-displacement response for the peak load of 2.8 μN.

Fig. 3.12 shows the force and displacement signals vs. time for the loading-unloading curve in Fig. 3.11. The force in the unit of μN and the displacement in the unit of nm actually share similarity in terms of orders of magnitude. However, comparison of Fig. 3.12 (a) and (b) leads to the finding that the displacement signal is much scattered than the force signal. This implies that present transducer has excellent performance in force sensing but the displacement sensing still need to be improved if higher resolution of data is desired.

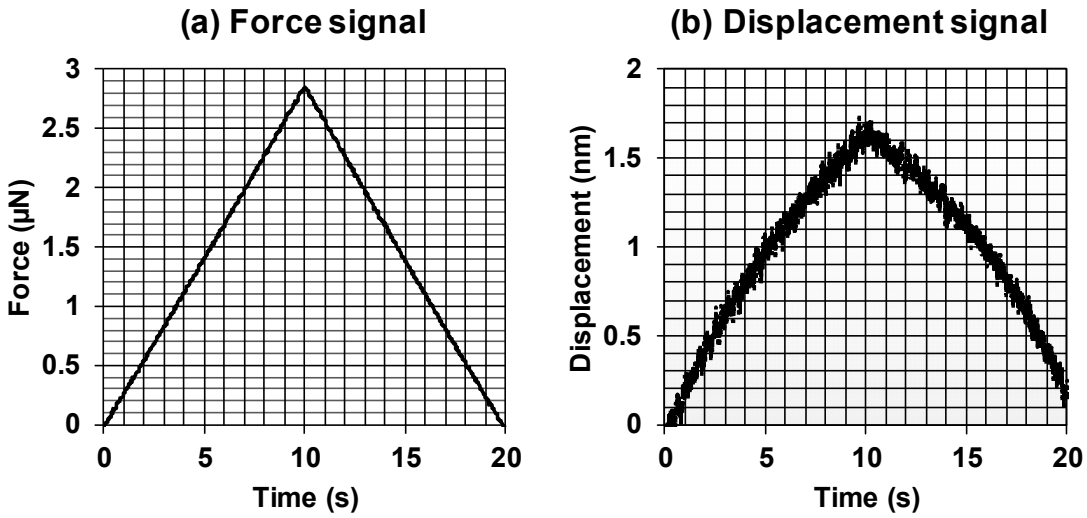

Figure 3.12 Force and displacement signals vs. time for the loading-unloading curve.

3.5 Adhesion measurements

The measurement of adhesion or pull-off force is another common application of force-displacement transducers. In such measurements, a probe is brought to light contact with the sample surface and then retracted from the sample surface, while measuring the in-situ force-displacement. This gives rise to the pull-on and pull-off forces that occur as

the tip sample approach each other and retract from each other, respectively. Because the adhesion force is usually very small and sensitive to the distance/displacement, it requires high transducer sensitivity and fast response, especially at the initial stage of separating the two surfaces.

In the present study, we performed adhesion experiments using the TI standard and MEMS transducers on the same sample (Fused Quartz standard sample), using the exact same set-up, including probe speed and data acquisition rate. The TI standard transducer is installed with a cube corner probe with a tip radius of 50 nm, which is similar to the probe on the MEMS transducer, to minimize probe differences. As shown by Fig. 3.13 (a) the TI standard transducer cannot clearly capture the adhesion force because its magnitude is low, similar to the noise level. On the other hand, the MEMS transducer, shown in Fig. 3.13 (b) clearly captures the pull-on and pull-off forces varying with distance. The measured maximum pull-off force is ~0.3 μN.

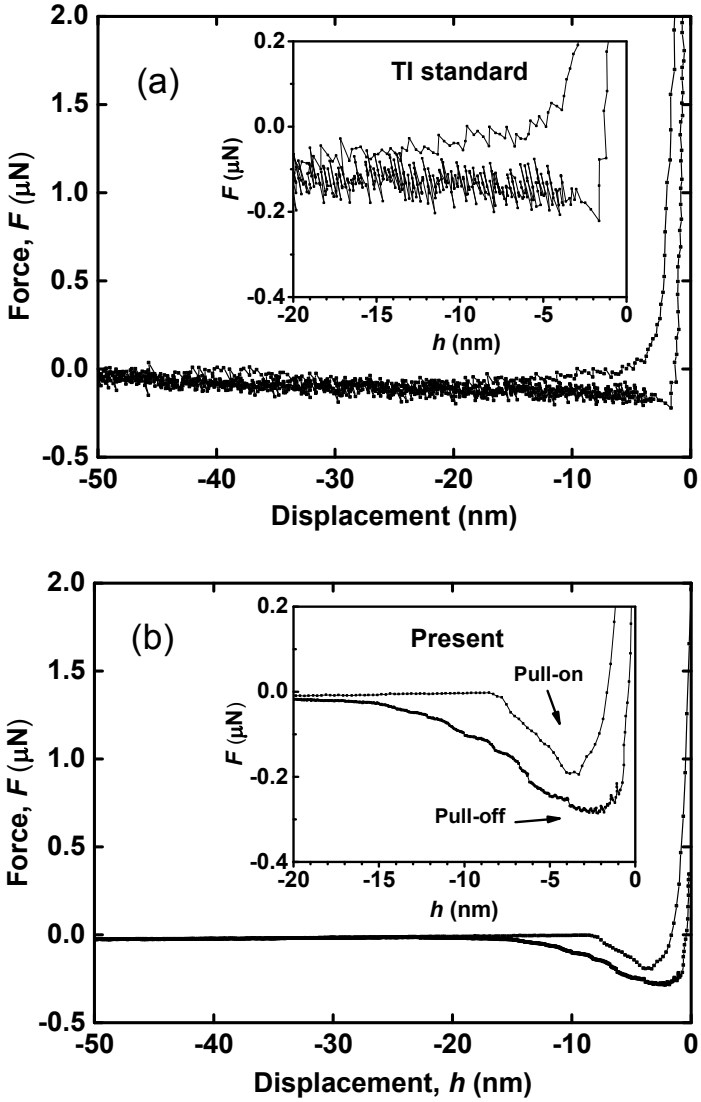

Figure 3.13 Adhesion measurements using the (a) TI standard, and (b) MEMS transducers.

3.6 Summary of Chapter 3

In this chapter, the thesis presents a highly sensitive force-displacement transducer based on MEMS technology for nanomechanical measurements. The transducer features a comb-drive design with very low moving mass of 5 mg. To compare the transducer with two state-of-the-art commercial nanoindentation systems, we performed three types of

experiments: air indentation, indentation on Fused Quartz and adhesion experiments. Experimental data show that the MEMS transducer exhibits significantly lower force and displacement resolutions, enabling the measurements of lower forces and displacements, encountered in shallow indentations. Air indentation experiments using the MEMS transducer report an RMS force resolution of 1.8 nN and RMS displacement resolution of 0.019 nm, compared to 45 nN and 0.23 nm for the TI Premier standard transducer. Nanoindentation experiments on Fused Quartz report in-contact resolutions of 5 nN for force and 0.05 nm for displacement. Such low resolutions ensure quantitatively measuring elastic modulus at very shallow contact depths of 0.7 nm. In addition to shallow nanoindentation experiments, the MEMS transducer was also used to measure very small adhesion forces between a sharp tip and a flat sample, capturing the pull-on and pull-off forces.

4 NANOMECHANICAL AND NANOTRIBOLOGICAL PROPERTIES OF 14-NM COCRPT-SIO_2 COMPOSITE FILMS

4.1 Introduction to tribological characterization of thin films

Solid thin films are widely applied in electronic devises using Micro/Nano-electromechanical systems (MEMS/NEMS). To satisfy needs in the industry, the deposition technology has been managing to make the film thickness smaller and smaller. For example, in order to obtain lower head-media spacing and thus higher areal density, the magnetic storage industry has reportedly reduced the thickness of diamond-like carbon (DLC) coatings deposited on top of the media from ~20 nm in 1998 (Mate, 1998) to ~3 nm in 2016 (Biswas and Knigge, 2016). Film quality is another representative of the level of deposition technology and critical for practical applications (Suh and Polycarpou, 2005). The DLC coating mentioned above has been made molecularly smooth, with a room-mean-square (RMS) roughness of less than 0.2 nm.

As one result of smaller thickness, the DLC becomes less protective of the recording layer. In addition, there is increased probability for occurrence of "head crash" that brings the head and the disk into direct contact and causes tribology induced data erasure (Xu et al., 2009). In another word, increased areal density through shortening the HMS somehow has sacrificed mechanical reliability at the head-disk interface where investigation of tribology becomes increasingly important (Gui, 2003). In the past, much attention has been paid in the literature to investigate the lubricant and the carbon coating in order to characterize and improve their tribological performances as protective layers

(Mate, 1998; Suh and Polycarpou, 2005; Lee et al., 2017). However, it is also important to study mechanical and tribological properties of the sub-20 nm magnetic recording layer itself, as the present study aims to do.

Nanoindentation and nanoscratch techniques are widely means to characterize nanomechanical and nanotribological properties of such nanoscale thin films (Bhushan and Li, 2003). They both relies on a nanomechanical transducer equipped with a rigid probe to perform mechanical testing on the sample. In nanoindentation experiments, the transducer makes a punch vertically on the sample using a rigid probe and records force and displacement responses or called loading-unloading curves. The elastic modulus can be calculated from the slope of the beginning part of the unloading curve, and the hardness can be calculated by dividing the maximum load with the calibrated contact area (Oliver and Pharr, 1992). Nanoscratch is a 2-D test that slides the probe (usually conospherical) laterally on the sample with a controlled normal load on the sample surface. The transducer records responses such as the frictional force and normal penetration depths.

As another result of thinner thin films, there is demand for development of more sensitive transducer in order to be capable of characterizing their material properties. For nanoindentation experiments, according to the literature and ISO standards (Lucca et al., 2010), the maximum permissible error for depth sensing nanoindentation (contact depth, h_c <200 nm) should be less than 1% of the maximum indentation depth. In the past 10 years or so, the root-mean-square (RMS) force resolution of a state-of-the-art nanomechanical system for nanoindentation has decreased from ~15 nN to ~5 nN, and

the RMS displacement resolution has reduced from 0.25 nm to 0.05 nm (Yu et al., 2005; Zhang et al., 2017).

In the present study, we first utilize a state-of-the-art MEMS transducer to perform sub-10 nm indentation experiments and measure nanomechanical properties. Then a regular transducer was used to perform shallow nanoscratch experiments and obtain nanotribological properties. Both nanomechanical and nanotribological properties were correlated with the bias voltage using the curve-fitting method.

4.2 Experimental setup

4.2.1 Sample description and instrumentation

CoCrPt-SiO_2 based materials have been chosen as the recording layer for perpendicular magnetic recording media because of small grain size, high anisotropy and good thermal stability (Piramanayagam, 2007). Fig. 4.1 depicts a cross-sectional view of Perpendicular Magnetic Recording (PMR) disk by Transmission Electron Microscopy (TEM) showing multiple layers of solid films. On the very top, there is a DLC coating of ~3 nm to protect the recording layer from mechanical wear and chemical corrosion. The recording layer is a 14-nm thick CoCrPt-SiO_2 composite. Below the recording layer, there is a Ru based intermediate layer with functions of exchange breaking and inducing texture growth of the recording layer. Below the intermediate layer, there is magnetic soft under layer (SUL) to help writing of data. Except the DLC coatings that is normally fabricated using plasma enhance chemical vapor deposition (PECVD), other films are deposited by magnetron sputtering.

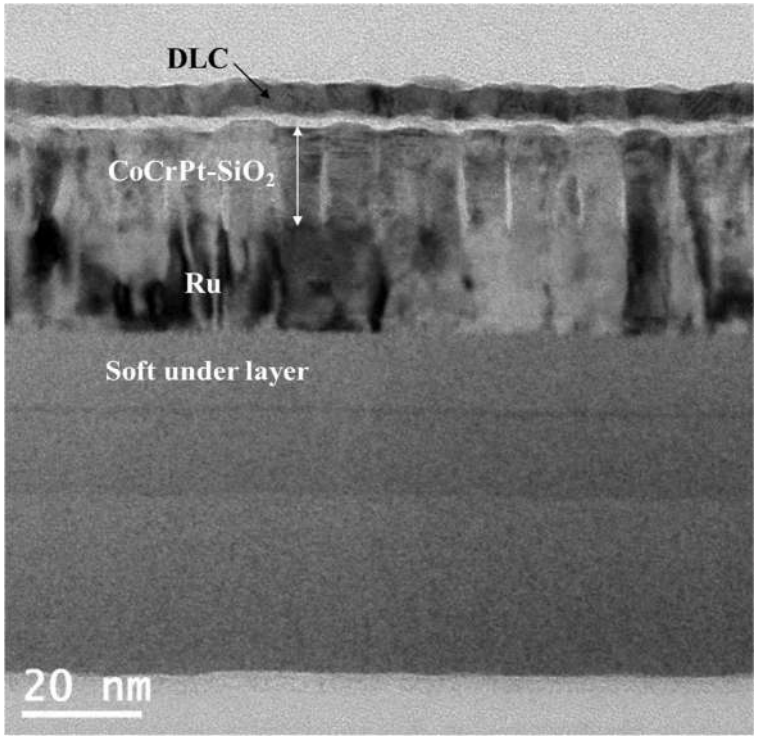

Figure 4.1 TEM images of a full-stack hard disk (cross-section view).

Fig. 4.2 are planar views of the CoCrPt-SiO_2 recording layer under TEM. The dark grains are CoCrPt with sizes varying from 5 to 10 nm. The white filling materials between grain boundaries are SiO_2. Three samples were prepared using different bias voltages when sputtering the CoCrPt-SiO_2 film, sample #1 (400 V), sample #2 (100 V) and sample #3 (0 V).

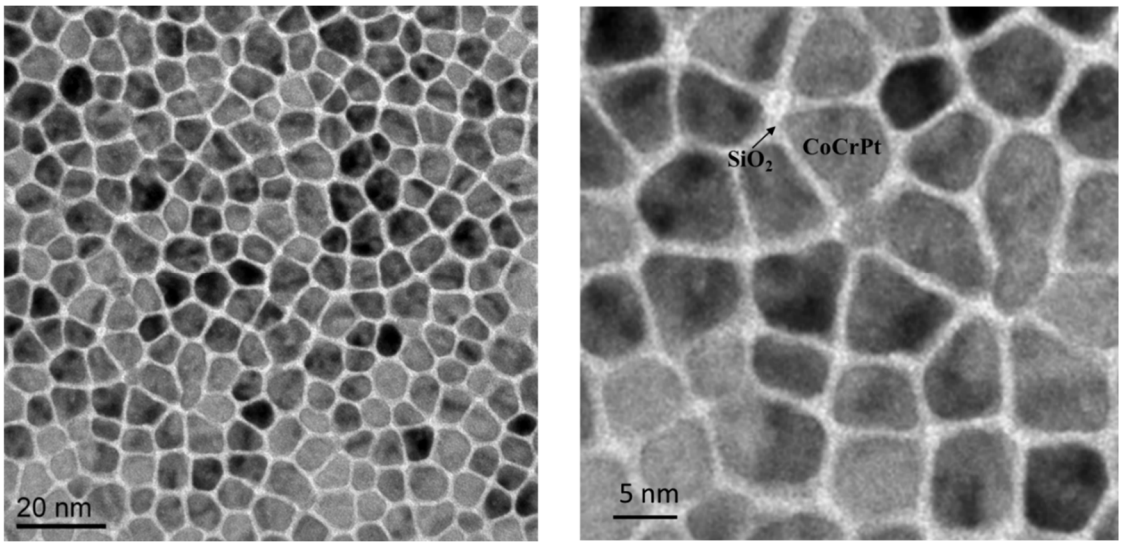

Figure 4.2 TEM planar views of the recording layer.

4.2.2 Instruments and experimental description

Present experiments utilize a 1-axis MEMS-based transducer (Zhang et al., 2017) installed with a cube corner probe with tip radius of 47 nm. The RMS force resolution is ~5 nN and the RMS displacement resolution is about 0.05 nm. Such a sensitive transducer and sharp probe were utilized to make sure the transducer is able to capture elastic and plastic deformations at shallow depths, in order to avoid substrate effects. Calibration experiments were performed on a standard sample (Fused Quartz) with recognized mechanical properties (elastic modulus=~69.6±5% GPa, hardness=~9.5±10% GPa). Calibration tests found the transducer is capable of obtaining accurate mechanical properties for contact depth down to ~2 nm.

The nanoscratch experiments employed a 2-axis standard transducer of TI Premier (Hysitron Inc.) with a RMS force resolution of 45 nN and a RMS displacement resolution of 0.22 nm. The probe for scratch tests is cono-spherical with a tip radius of about 350

nm. Please note that in our nanoscratch experiments, the used transducer is less sensitive and the probe is blunter. This is because for 2-axis scratch experiments, the probe can not made to be too sharp as it will be damaged due to high shear stress when sliding on the sample. So usually a blunter cono-spherical probe is used with a relative larger force to make plastic deformation of the sample. Therefore, it is less demanding of the force and displacement resolutions than nanoindentation.

4.3 Results and discussion

4.3.1 Nanoindentation

To detect mechanical properties of 14 nm media films as in the present study, the indentation depth has to be very small. On the other hand, to avoid substrate effects from the intermediate layer, we limited the contact depth less than 10 nm. We used a trapezoid load function, 5 seconds for loading, 2 seconds for holding and 5 seconds for unloading. On each sample, we performed 20 indentation tests with peak load varying from 30 μN down to 11 μN. Fig. 4.3 (a) displays some of the force-displacement responses. All the loading curves overlap, indicating consistency of measurement. As shown in the residual scanning probe microscopic (SPM) image for sample #1 by Fig. 4.3 (b), the indentation experiments were set up as a 4×5 matrix with a spacing of 0.5 μm between two adjacent indents.

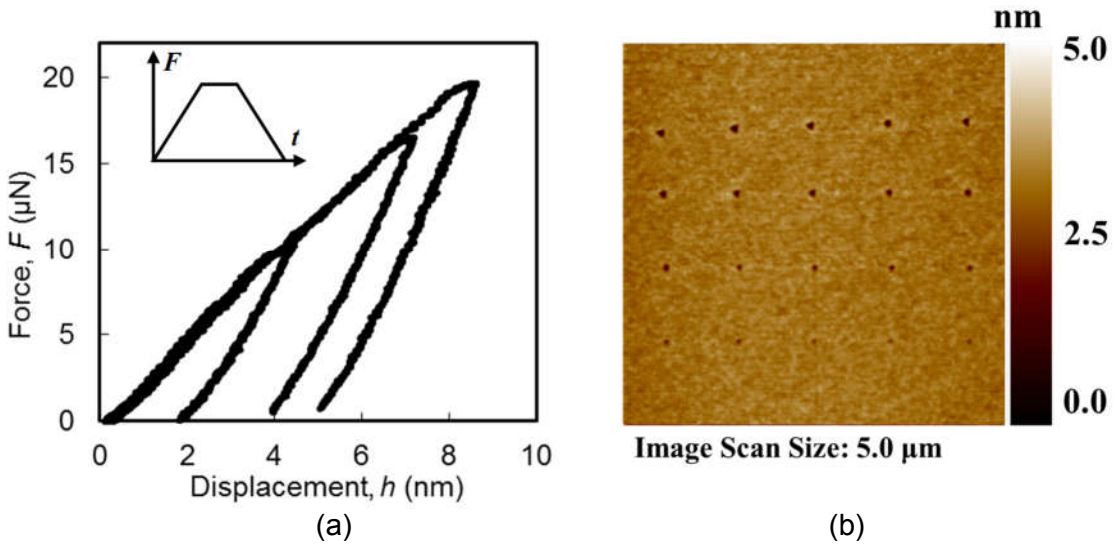

Figure 4.3 Experiment results on sample #1: (a) Force- displacement responses of at the load of 10, 15 and 20 μN; (b) SPM image of the matrix of for tests using indentation forces varying from 30 μN to 11 μN.

Fig. 4.4 shows measured mechanical properties of the sample #1. Measurements for elastic modulus and hardness show different trends, which requires knowledge of contact mechanics to interpret. The famous 10% rule states that the indentation depth should not exceed 10% of the film thickness to avoid substrate effects. It was found this rule has been misused and determination of the substrate effects should be more flexible in practice (Fischer-Cripps, 2006). The rule was proposed to restrict the domain of the plastic zone within the film material, thus has no basis on determination of elastic modulus. Even for indentation hardness, it was found in numerical simulations that the substrate effects are not fixed but greatly dependent on yield strengths of the film/substrate system (Chen and Vlassak, 2001). For a soft film on a hard substrate, the influence of the substrate is not appreciable until the indentation depths reaching almost half of the film

thickness (Chen and Vlassak, 2001). Tayebi et al. (2004) reported similar findings in their nanoindentation and nanoscratch experiments.

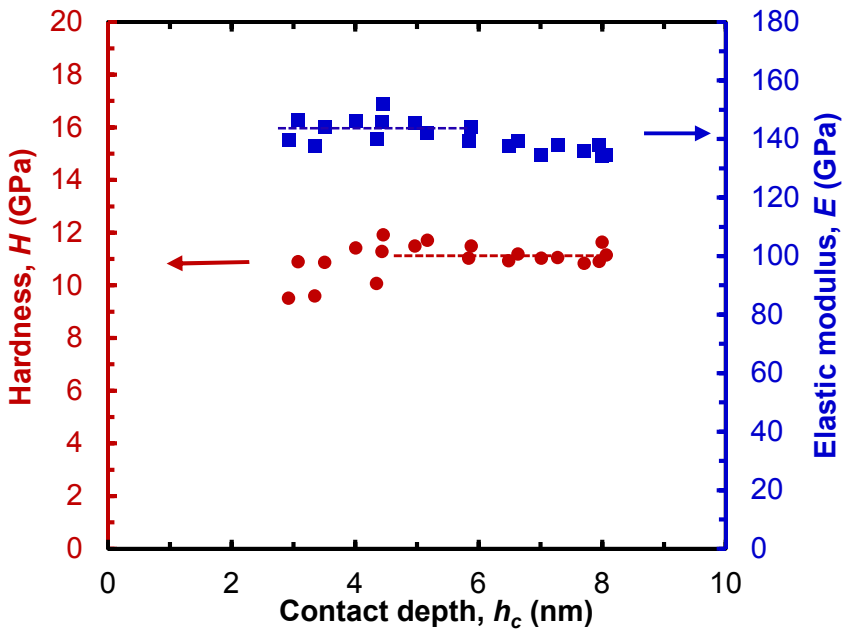

Figure 4.4 Measured mechanical properties of the sample #1.

Calibration experiments were performed based on acknowledgment of elastic modulus of Fused Quartz prior to present nanoindentation experiments. Therefore, the elastic modulus measurement before contact depths of ~4 nm in Fig. 4.4 are real reflection of the 14-nm thin films. After contact depths of larger than ~6 nm, the data begins to decrease and reflect substrate properties. The hardness data shows an increasing tendency at shallow depths, due to insufficient plastic deformation. As the indentation load or depth increases, there is full plasticity and the measurement becomes flat. The plateau segments marked in dash lines are nanomechanical properties for the thin films of the interest. Fig.

4.5 summarizes averages of the three thin films and correlates them with their bias voltages. Both of elastic moduli and hardness increase with the bias voltage but the hardness shows sharper increasing tendency.

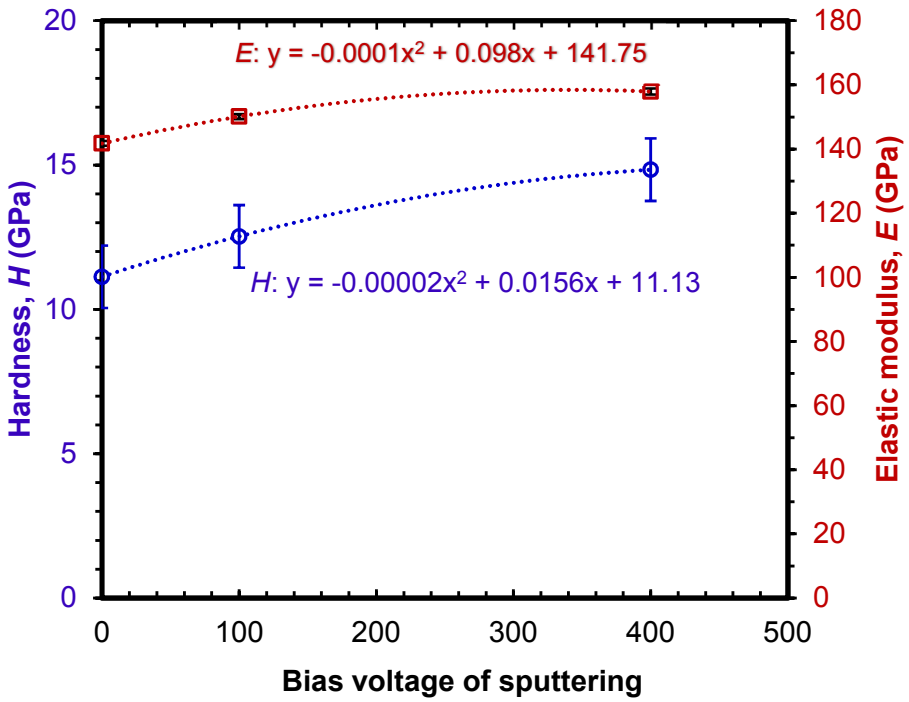

Figure 4.5 Elastic moduli and hardness with sputtering bias voltage.

Hardness is an important mechanical property quantifying the resistance of a material to plastic deformation. Note that hardness is not a fundamental material property but can be related to one, i.e., yield strength. The famous relation proposed by Tabor (2000) correlates it with a yield strength $\sigma_{y,}$ through $H=3\sigma_y$. This relation makes good predictions for very plastic materials ($E/\sigma_y >>1$) such as bulk metals. For nanoscale materials with small E/σ_y ratios, the coefficient for H/σ_y is smaller than 3 and approaches

to 1.7 (Cheng and Cheng, 1998). Johnson (1970) proposed a more flexible relation after considering indenter geometry and material properties:

$$\frac{H}{\sigma_y} = \frac{2}{3}\left[1 + ln\left(\frac{1}{3}\frac{E}{\sigma_y}\tan\beta\right)\right], \tag{4.1}$$

,where β is the equivalent angle between the indenter and the sample surface plane, equal to 47.7° for the cube corner tip used in the present study.

Table 4.1 summarizes yield strengths of the three samples based on Eq. (4.1). The yield strength decreases more sharply with the bias voltage after considering the variation of elastic modulus. Please note that the yield strength is a fundamental material property for deciding onset of plastic deformation. The elastic moduli and yield strengths in Table 4.1 can be used in finite element analysis for hard disks for parametric studies as done in the literature (Ovcharenko et al., 2010; Katta et al., 2010; Liu et al., 2014).

Table 4.1 Measured mechanical properties of different layers in the HDD sample.

Properties	**Elastic modulus, *E* (GPa)**	**Hardness, *H* (GPa)**	**Yield strengths, σ_y (GPa)**
Sample #1 (400 V)	157.94	14.84	7.17
Sample #2 (100 V)	150.11	12.53	5.72
Sample #3 (0 V)	141.75	11.13	4.97

4.3.2 Nanoscratch

In the nanoscratch experiment, the transducer needs input for normal force and lateral displacement vs. time. When the probe is controlled to slide on the sample surface, the transducer records lateral force and normal displacement signals. After the

measurement, friction coefficient can be calculated by diving the lateral force with the normal force. Normal displacement include in-situ and residual displacement can be used to evaluate how much the penetration and residual depths are at certain forces.

Fig. 4.6 are the conno-spherical probes used in the present experiments. The probe is conical with a spherical tip on the top. The tip radius is 357 nm and the half angle of the conical part is 29.6°, making the depth of the spherical top is ~320 nm nm if we use analytical expressions for probe geometry in the literature (Yu et al., 2004). Present experiments are to measure properties of sub-20 nm films so only the spherical part is in contact with the sample. In another word, present scratch experiments can be viewed as a sphere scratching on the sample surface.

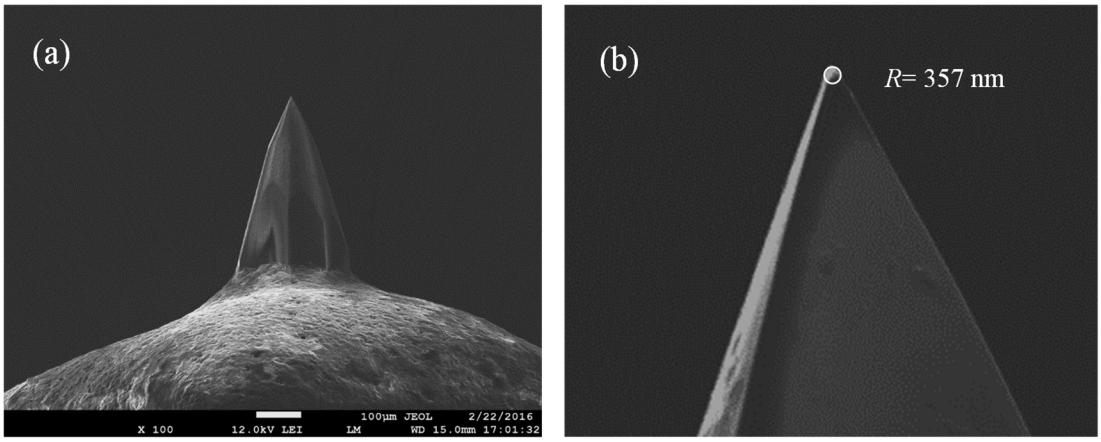

Figure 4.6 SEM images of the cono-spherical probe used for nanoscratch experiments.

The scratch load has to be large enough to ensure the tip leaves material plastic deformation of the layer of the interest, but also small enough so that the plastic deformation does not include much substrate effects. Present study utilizes the TEM-

scratch technique to investigate where the plastic deformation is located in order to determine appropriate values for the scratch load in present experiments.

Fig. 4.7 shows a cross sectional view of the wear track after a nanoscratch test on the sample #3 with a force of 100 μN using the same probe. Referring to Table 4.1, the mean Hertzian contact pressure is calculated to be 10.39 GPa. The maximum wear depth caused by such a high pressure was measured to be 3.54 nm. Moreover, there is no significant displacement between at the boundary between the recording layer and the Ru layer, indicating the wear is mainly from plastic deformation of the recording layer ($CoCrPt\text{-}SiO^2$).

As the sample #3 has the smallest yield strength, we can determine that if we keep the mean contact pressure under 10.39 GPa, it can be inferred that the other two harder samples will have less plastic deformation and the Ru substrate will be protected from plastic deformation as well. Therefore, we selected 90 μN as the maximum scratch force used in the nanoscratch experiments. And the mean contact pressure at 90 μN are 10.03 GPa, 9.70 GPa and 9.33 GPa for sample 1, sample 2 and sample 3, respectively.

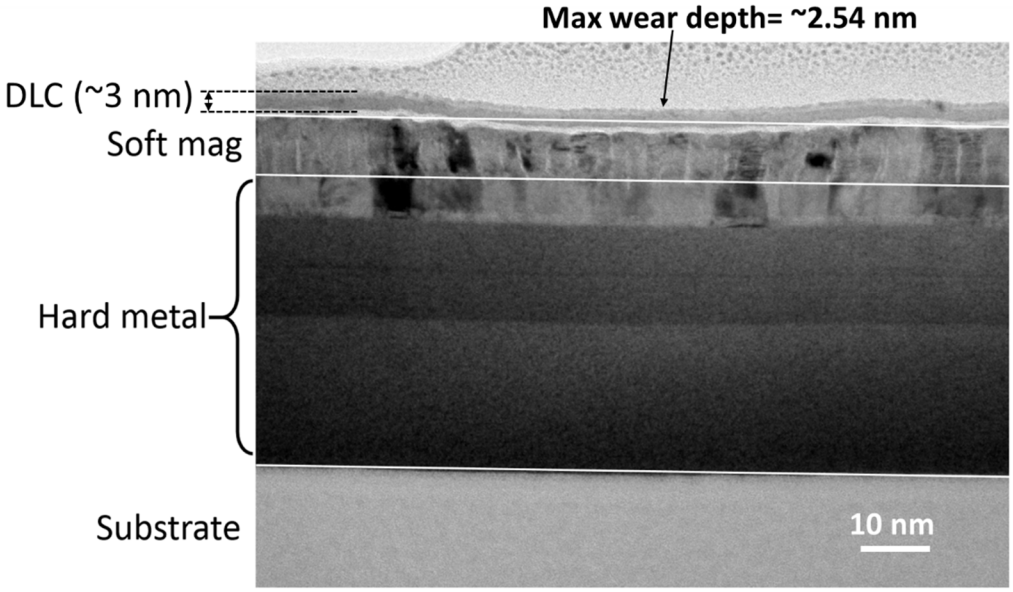

Figure 4.7 TEM cross sectional view of the wear track after a scratch using force of 90 μN on sample #1 (mean contact pressure 10.39 GPa).

In present experiments, we use a load function as shown in Fig. 4.8(a). The experiment can be divided into following three steps: (1) the prescan step from 0 to 20 s for data correction to remove any misalignment of the normal displacement due to tilt or gradient of the sample surface, (2) the loading step from 20 s to 50 s for the tip to scratch laterally on the sample surface with a constant normal load applied vertically and (3) the retrace step for the tip to scratch backward with a light contact force and detect the residual depth of the groove. Three groups of experiments were performed and each group includes seven experiments varying the scratch load from 30 μN to 90 μN with an increment of 10 μN. The residual depth is at the sub-10 nm level while the tip radius is a few hundreds of nanometers. Therefore, the retrace step may not be able to capture the real residual depths. Present study marked the scratched regions of the sample and located the scratch marks

under the Atomic Force Microscopy (AFM) which has higher resolution in terms of characterizing surface morphology.

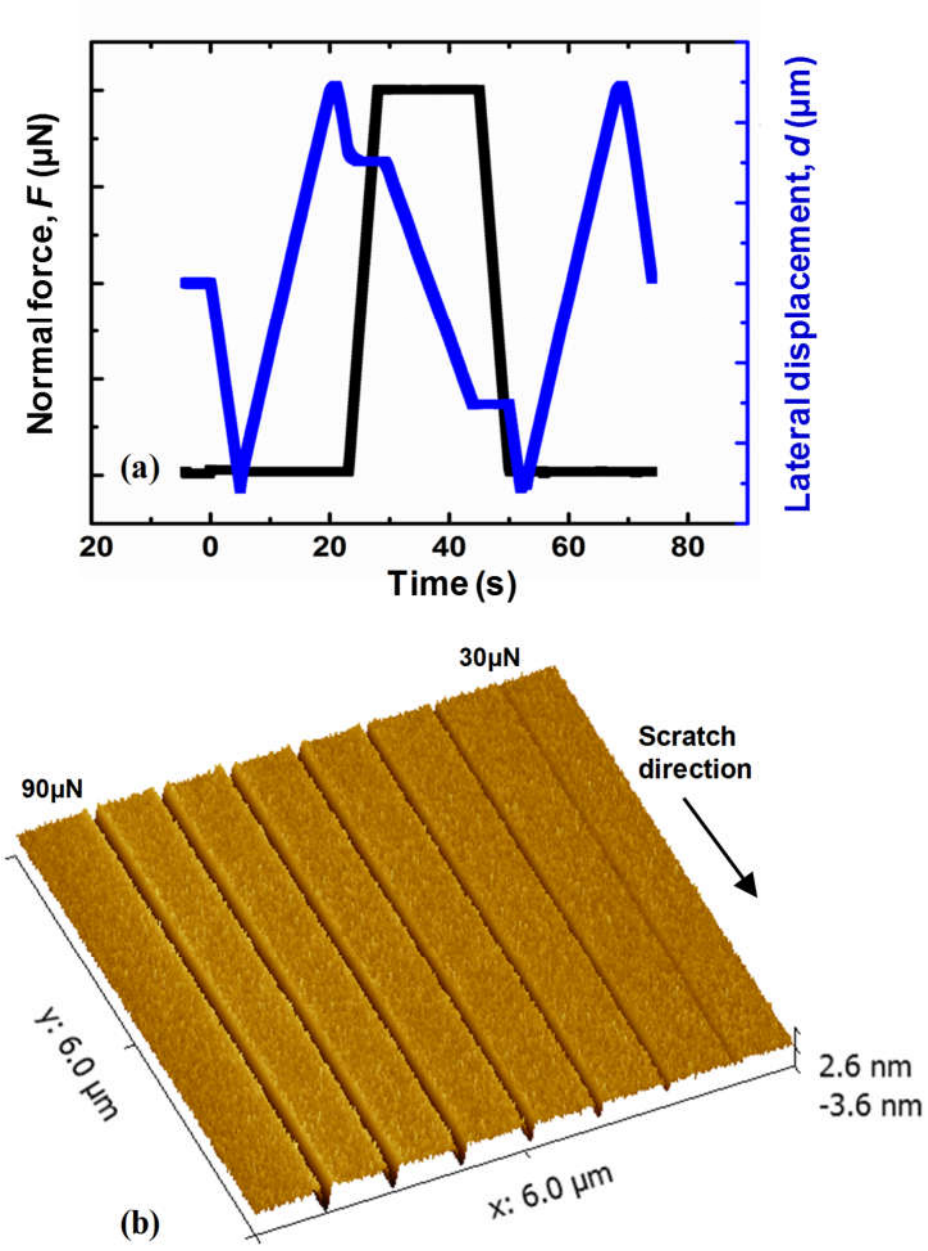

Figure 4.8 (a) Load function and (b) AFM images of the scratch grooves for different forces.

Fig. 4.9 summarizes the in-situ and residual depths from nanoscratch experiments and post-scan AFM images. The in-situ depths of the three sample are very similar, as shown in Fig. 4.9 (a). This is because the in-situ depths are greatly dependent on the elasticity and the three samples have similar elasticity properties, see in Table 4.1. As one result of the similarity in in-situ scratch depths, the measured friction coefficients that are dominated by deformation or plowing are also similar and reported to be around 0.10. Therefore, the stress distribution under the probe should also be similar.

It is also important to discuss the substrate effects to ensure the nanoscratch experiment detects most of tribological behaviors of the recording layer rather than the Ru substrate. The elastic modulus and yield strength of the Ru layer were characterized to be 112.7 GPa and 4.58 GPa, respectively (Zhang et al., 2017). Therefore, all three samples can be taken as a hard film on a soft substrate with $1<\sigma_f/\sigma_s<2$. The contribution from the substrate effects increases with the contact depth (in-situ depth). At the maximum in-situ depths (~11 nm), the substrate effect is about 20% for nanoindentation according to a map for substrate effects by Chen and Vlassak (2001). As for sliding contact, the stress distribution is nearer to the surface due to traction and thus there is less substrate effect. Therefore, we can estimate that even at the case of 90 μN, more than 80% of plastic wear of present scratch experiments is from the recording layer. This percentage should be higher at lower scratch load. However, at the minimum load (30 μN), we also need to consider effects of the 3-nm DLC coating.

Fig. 4.9 (b) depicts residual depths of the three samples after scratch tests using different load. The three samples reports similar residual depths at the load of 30 μN

because of the DLC coating. After that, residual depths of the three increase almost linearly with the applied load. Among them, sample #1 reports the smallest residual depths, with an average of 1.25 nm at the maximum load (90 μN). Other than that, sample #1 and sample #2 report similar residual depths until scratch load of larger than 60 μN. It is possible that their transition layers between the DLC coating and the recording material have similar strengths. Sputtering voltage of 100 V (sample #2) cannot improve much the wear resistance of the transition layer comparing to sample #1 using 0 V.

Residual depths are direct measurement from experiments and dependent on experimental setup such as the scratch load and tip geometry. Another parameter to represent the wear resistance of the material is the reciprocal of the dimensional wear coefficient or the specific wear rate defined by Archard (1953):

$$R_w = 1/k = \frac{Ps}{V_w} \tag{4.2}$$

, where V_w is the wear volume, P is the normal load and s is the sliding distance. Similar calculation of wear resistance from nanoscratch data can be seen in the literature by Hodge and Nieh (2004). For constant-load scratch experiments such as in present work, the wear volume can be approximated as a triangular prism whose volume can be calculated by:

$$V_w = \frac{h_r w_r s}{2} . \tag{4.3}$$

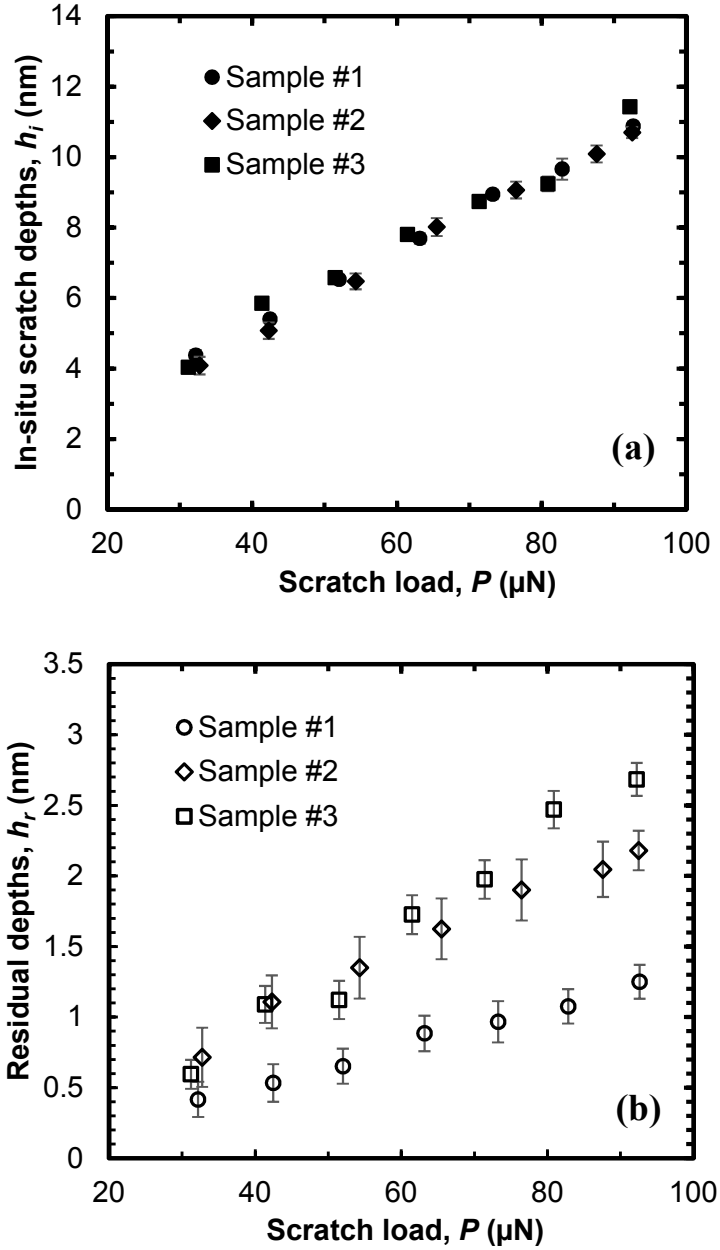

Figure 4.9 (a) In-situ and (b) residual scratch depths of three samples with different porosity

Please note that residual widths w_r are similar to in-situ scratch widths w_i (Komvopoulos and Bogy, 1996). Then from in-situ depths shown in Fig. 4.9 (a), we are able to calculate the wear residual widths using the fitting:

$$w_r \cong w_i = 2\sqrt{Rh_i} \tag{4.4}$$

Substitution of Eqns. (4.3) and (4.4) into (4.2) leads to:

$$R_w = \frac{P}{h_r\sqrt{Rh_i}} \tag{4.5}$$

, which is a function of the hardness, in-situ and residual scratch depths, the stylus tip radius (357 nm) and the normal scratch force. Values of these parameters are available from experimental data in Table 4.1 and Fig. 4.9. Present calculation of wear resistances excludes the first data point at the load of 30 μN as it has much contribution from the DLC coating.

Fig. 4.10 depicts calculated wear resistances of the three samples. The wear resistance in the unit of 10^{11} GPa increases dramatically with the bias voltage. A linear relation is able to fit well the dependence of the wear resistance on the bias voltage.

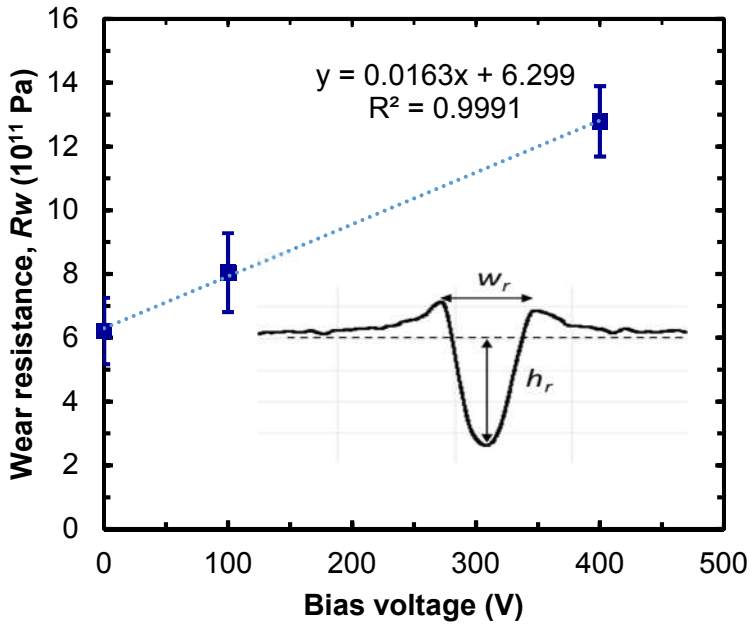

Figure 4.10 Wear resistance R_w vs. bias voltage and the fitting relation.

4.4 Summary of Chapter 4

The present study dedicates to characterizing mechanical and tribological properties of 14-nm thin films through nanoindentation and nanoscratch experiments using state-of-the-art nanomechanical systems. Nanoindentation experiments at the contact depths of less than 10 nm measured mechanical properties including elastic moduli and hardness of the thin films. Indentation data shows the hardness and yield strengths increase significantly with the bias voltage. Nanoscratch experiments captured mechanical behaviors of the thin films under sliding contact with a rigid probe. The degrees of wear represented by residual depths or plastic deformation decreases dramatically as the sputtering bias voltage increases.

5 HIGH-TEMPERATURE NANOTRIBOLOGICAL PROPERTIES OF ULTRA-THIN HYDROGENATED AMORPHOUS CARBON COATINGS

5.1 Introduction to amorphous hydrogenated carbon films

Amorphous Diamond-like carbon (DLC) is widely used in industry as protective coating material because of its high hardness, low friction coefficient and good wear resistance (Robertson, 2002; Erdemir and Donnet, 2006). Composition-wise there are different types of DLC including hydrogen-free amorphous carbon (a-C), hydrogen-free tetrahedral amorphous carbon (ta-C), hydrogenated amorphous carbon (a-C:H) and hydrogenated tetrahedral amorphous carbon (ta-C:H) (Charitidis, 2010). Also, there are amorphous carbon films with metals as additives such as tungsten (a-C:W, a-C:H:W), or with non-metal elements such as silicon (a-C:Si, a-C:H:Si). Their mechanical properties vary to satisfy different industry needs (Bewilogua and Hofmann, 2014).

In some electronic devices with Microelectromechanical systems (MEMS) or Nanoelectromechanical systems (NEMS), amorphous DLC coatings are widely applied to protect functional thin films from mechanical wear and chemical corrosion. For example, in magnetic storage hard disk drives (HDD), a hydrogenated carbon (a-C:H) overcoat with a thickness of about 3 nm is typically deposited above the magnetic media. Comparing hydrogen-free a-C films and hydrogenated a-C:H films, the absence or presence of hydrogen is critical in determining their tribology properties (Erdemir, 2001). It was found

* Reprinted with permissions from "High temperature nanotribology of ultra-thin hydrogenated amorphous carbon coatings" by Y. Zhang, K. Polychronopoulou, M. Humood and A.A. Polycarpou, Carbon 2017, 123, 112-121. Copyright (2017) by Elsevier.

that tribo-chemical wear is more dominant for a-C films where dangling bonds of carbon are saturated by oxygen from environment (Marchon et al., 1990) or gradual graphitization can be induced by shear stress (Ma et al., 2009). Addition of hydrogen in a-C:H films is found to greatly reduce friction and wear, as observed in experiments (Erdemir, 2001; Ma et al., 2009; Agarwal et al., 1993; Grill, 1999). There are debates on mechanisms for how hydrogen reduces friction and wear of amorphous carbons. One explanation, the graphitization mechanism, believes that hydrogen promotes the formation of a self-lubricating graphitized tribofilm under sliding motions (Erdemir, 2001; Grill, 1999). Another one, the passivation mechanism, believes that hydrogen saturates dangling bonds of carbon atoms at the sliding interface that may be otherwise oxidized (Cui et al., 2014; Gao et al., 2002).

Other than investigating effects of hydrogen, extensive research has been carried out to study nanowear and nanomechanical properties as well as wear mechanisms and modelling of the ultra-thin a-C:H coating since its application (Wei and Komvopoulos, 1997; Bhushan, 1999; Lee et al., 2006; Lee et al., 2017). In recent years, durability of ultra-thin a-C:H coatings at high temperature is drawing increasingly more attentions. For example, in the HDD industry, with development of the heat assisted magnetic recording (HAMR) technology (Kryder et al., 2008), there is increasing interest in durability of coatings and thin films at high temperature. Meanwhile, many MEMS/NEMS devices applying a-C:H films are also confronted with challenges at high temperature due to overheat. Experiments using XPS and Raman Spectroscopy on thermally annealed a-C:H films have captured sp^3-to-sp^2 conversion, sp^2 clustering, hydrogen loss and carbon loss

(Mangolini et al., 2013; Wang et al., 2013; Rose et al., 2014; Jones et al., 2014; Zhang et al., 2001). There have been some high-temperature tribology experiments conducted on thicker a-C:H films (150~500 nm) in the literature (Van der Donck et al. 2009; Li et al., 2006; Venkatraman et al. 1999). Van der Donck *et al.* (2009) performed *in-situ* high-temperature tribology experiments up to 150 °C and observed significantly increased wear rate of a-C:H films at 100 °C. Thermal annealing tests found that wear of a-C:H films becomes severe at temperatures of 300°C (Li et al., 2006) and 400 °C (Venkatraman et al. 1999). The above mentioned high-temperature tribology tests were conducted on rougher a-C:H films of ~150-500 nm thickness which are not suitable for MEMS/NEMS applications. In addition, the tribology properties of a-C:H films exhibit thickness dependence (Li et al., 2014; Lemoine et al., 2004; Yeo et al., 2007). Therefore, it is necessary to perform well-designed and independent tribology experiments at high temperatures to measure friction and wear of much thinner a-C:H films (<10 nm).

In this chapter, a high temperature nanomechanical system and its evaluation of thermal drift rates, as well as the geometry of the probe are first presented. Then results from the nanoscratch and nanowear experiments at temperatures ranging from 25 °C to 300 °C are presented and thoroughly discussed. An empirical relationship obtained from curve-fitting of the experimental data is proposed to reveal the temperature dependence of the wear rate. The deterioration of the wear resistance of the films is discussed based on the Raman spectra analysis performed before and after the high-temperature experiments.

5.2 Experimental setup

5.2.1 Samples

The sample is a 3-nm thick hydrogenated amorphous carbon film (a-C:H) deposited on Nickel-Phosphorus (NiP)-plated Aluminum (Al) substrate using the Plasma-Enhanced Chemical Vapor Deposition (PECVD) method. The sample surface is extremely smooth, having an RMS roughness of 0.2~0.3 nm, similar to that reported in the literature (Lee et al., 2006). The PECVD technique uses a hot filament cathode to create a plasma from a hydrocarbon gas precursor. Substrate bias was used to modify the carbon properties during growth.

5.2.2 Instrument and experimental setup

The experiments are conducted on a high temperature nanomechanical stage (TI Premier, Hysitron Inc.). A schematic and a photograph of the stage are shown in Fig. 5.1 (a) and (b) respectively. The probe has a long shaft with a diamond Berkovich tip on the top. Inert gas (Ar) is introduced in the chamber to minimize graphitization of the diamond that becomes significant at temperatures above 400°C (Wheeler et al. 2010). The stage is enclosed with insulator materials to ensure thermal stability. There are temperature sensors, heating and cooling systems on the top and the bottom of the sample which are regulated by a temperature controller to achieve the desired temperature. In the present experiments the heating is retained for about 15 minutes, until the sample is thermally stable. This is because at elevated temperatures, the thermal drift rate is generally higher than at room temperature and it takes a longer time for the contact interface to reach thermal stability.

In the present work, the maximum temperature was limited to 300°C, which is of practical interest and challenging. Tests are conducted successively at room temperature (25°C), 100°C, 200°C, and 300°C and then at room temperature again, after cooling down of the samples.

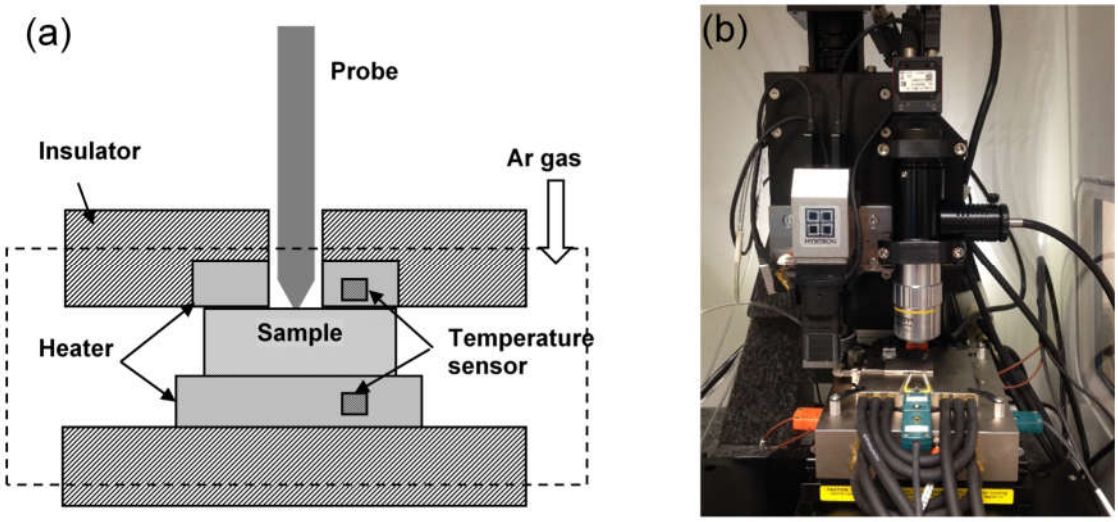

Figure 5.1 (a) Schematic of the high-temperature stage; (b) photograph of the Hysitron xSol^{R} high-temperature nanomechanical system.

Ideally a cono-spherical probe is preferable for 2D-axis experiments such as single scratch and wear scanning experiments. However, the high-temperature cono-spherical probe is too blunt for shallow tribology experiments. As a substitution, the present experiments utilize the spherical part of a Berkovich probe. Theoretically, three-sided pyramidal probes, including Berkovich and cube corner probes, have a spherical part on the top of the tip and a conical part, whose contact areas can be expressed by the following analytical relations (Yu et al., 2004):

$$A_{spherical} = \pi h_c(2R - h_c), 0 < h_c < h_{spherical} \quad (5.1a)$$

$$A_{conical} = \pi tan^2\theta(h_c + \frac{R}{sin\theta} - R)^2, h_c > h_{spherical} \quad (5.1b)$$

For shallow tribological friction and wear experiments on thin films, an advantage of using the pyramidal probe for 2D-axis experiments is that the tip radius is usually smaller than that of a cono-spherical probe. So, the probe can cause wear of the thin film at smaller contact depths and normal forces, and thus less substrate effect contribution is taking place. A similar application was reported in the literature where a cube corner probe was used to perform 2D-axis experiments on sub-10-nm carbon coatings (Lee et al., 2006).

The depth of the spherical part of the probe is very small, approximately 9 nm according to Yu et al. (2004). In order to protect the probe and also avoid directional dependence in the experiments, it is important to limit the contact between the probe and the sample within the spherical part. Therefore, it is necessary to characterize the tip geometry in order to determine how deep the spherical part can penetrate and how much normal force should be applied.

The tip geometry can be determined from the contact area that is obtained from calibration experiments on a standard sample, usually Fused Quartz. Fig. 5.2 shows the experimental tip area function at room temperature. Using Eqns. (1), the tip radius is found to be 124.5 nm and the spherical part of the probe is at contact depths h_c< 8.7 nm. Estimation of the normal force to maintain the contact within the characterized spherical part will be discussed later.

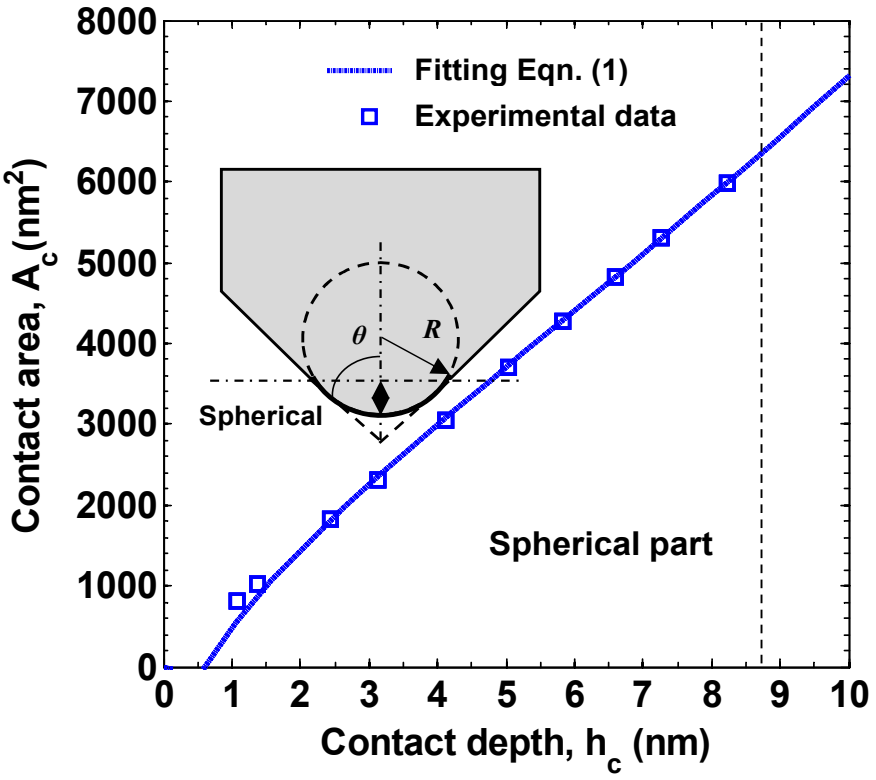

Figure 5.2 Schematic view of a Berkovich tip and its area function fitted by Eqns. (1), with tip radius R=124.5 nm, θ=68°, the resultant spherical part is when contact depth is less than 8.7 nm.

The thermal drift rate in units of nm/s measures the expansion or contraction speed of the sample surface due to temperature changes. For high temperature nanomechanical systems, the thermal drift rate is very important and has to be kept low so that force and displacement responses are not significantly affected by simultaneous thermal deformation. Fig. 5.3 shows the thermal drift rates of the system at temperatures up to 300°C. At each temperature, there were 25 nanoindentation experiments conducted on the standard Fused Quartz sample. The average drift rates increasing with temperature are reported, with the average drift rate at 300°C being less than 0.2 nm/s, which is

significantly lower than values reported in the literature (Schuh et al., 2006; Trenkle et al., 2010).

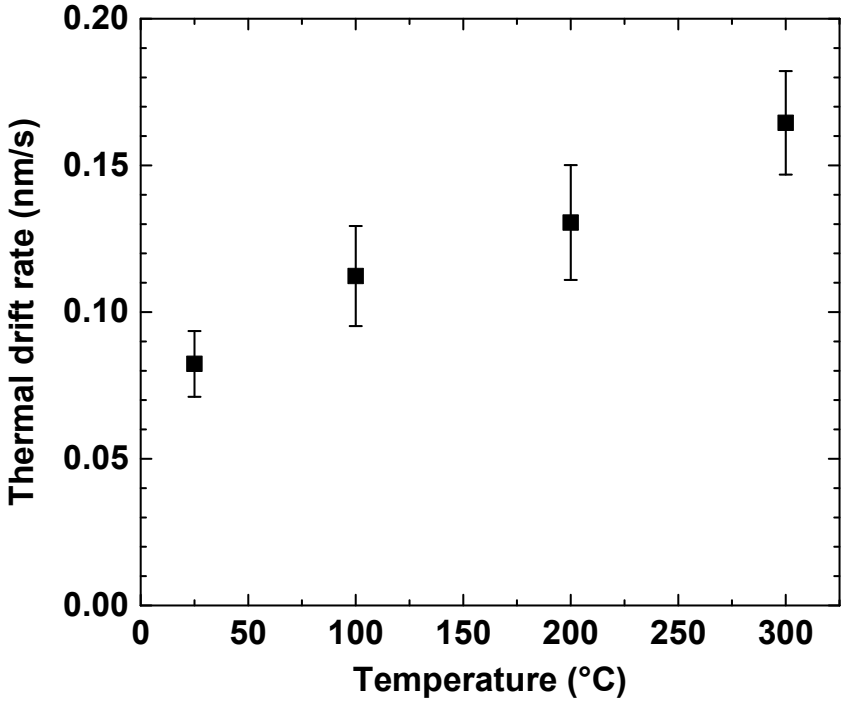

Figure 5.3 Thermal drift rate of the high temperature stage (based on 25 indentation experiments on Fused Quartz sample at each temperature).

The experiments are conducted on a high temperature nanomechanical stage (TI Premier, Hysitron Inc.). Inert gas (Ar) is introduced in the chamber to minimize graphitization of the diamond probe whose tip radius is calibrated as 124.5 nm. The stage is enclosed with insulator materials to ensure thermal stability. The thermal drift rate of the system increases with temperature, with 0.08 nm/s at 25 °C and 0.17 nm/s at 300 °C, according to calibration experiments. Detailed description and calibrations of this instrument are given in the supporting information. Present tribology experiments are

performed at 25 °C, 100 °C, 200 °C, 300 °C and 25 °C. So the sample experiences gradual heating to 300 °C and then cooling down to 25 °C. Between two testing temperature, the sample is retained for about 15 minutes to ensure it is thermally stable.

5.2.3 Raman spectroscopy

A Raman confocal microscope made by Horiba Ltd (Jobin-Yvon LabRam) is used over two a-C:H samples, one pristine and one following heat treatment at 300^{o}C. The laser wavelength is 633 nm and the exposure time is 15 s with 5 accumulations for each test.

5.3 Results and Discussion

5.3.1 Nanoscratch experiments

For hard coatings with weak viscoelasticity, their mechanical behaviors show very small time dependence and thus ramp-load scratch is an effective and convenient method to evaluate their tribology properties. In the literature, there are quite a few applications of ramp-load scratch on investigating tribological properties of carbon coatings (Lee et al., 2006; Huang et al., 2002; Ma et al., 2003).

Fig.5.4 (a) shows a schematic view of the ramp-load scratch experimental set up. The transducer controls both the lateral sliding distance and the normal load that is applied on the diamond probe. In general, there are three steps for the ramp-load scratch experiments, namely: (a) the pre-scan, (b) the scratch and (c) retrace (or post-scan), see Fig. 5.4(b). In the pre-scan step, the probe is moving laterally on the sample surface with a small contact force of 2 μN to ensure contact and trace the surface topography. The pre-scan step is used for data correction that removes any misalignment of the normal displacement due to tilt or gradient of the sample surface. In the scratch step, the transducer

applies the ramp load increasing linearly from zero to the peak load, while moving the probe laterally with a constant speed for a specified sliding distance. The present experiments use a peak load of 30 μN corresponding to a sliding distance of 5 μm, and the duration of the experiment is 15 s. The resulting loading rate is 2 μN/s and the scratch velocity is 0.33 μm/s. The scratch step measures the in-situ scratch depth and the in-situ friction force (converted to friction coefficient). In the retrace step the probe moves backward from the peak-load point back to the beginning point of the ramp-load scratch, with a small contact force (2 μN), in order to measure the residual depth of the scratch groove.

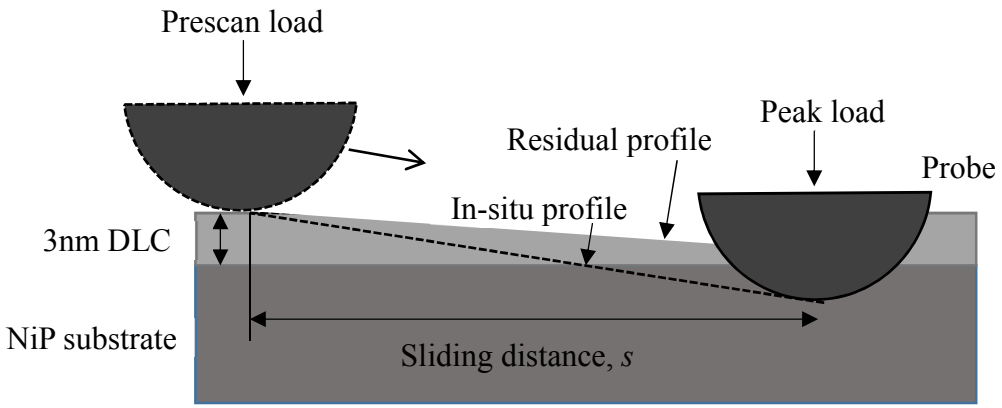

(a)

Figure 5.4 (a) Schematic view of a ramp-load scratch experiment; (b) ramp load function used in the present experiments (scratch distance s=5 μm, scratch peak load, F_{max}=30 μN, loading time=15 s).

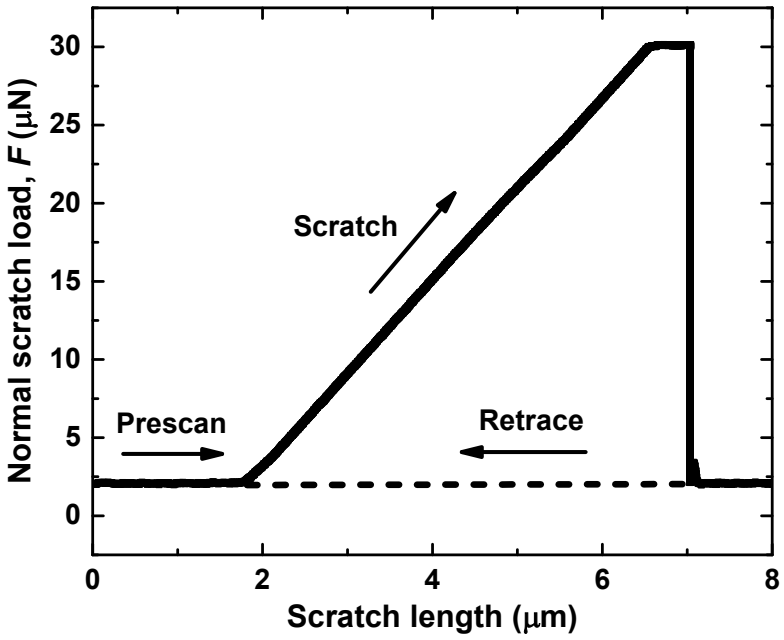

(b)

Figure 5.4 Continued

5.3.1.1. In-situ and residual scratch depths

Fig. 5.5 plots the in-situ scratch and residual depths at room temperature before heating (a), 300 °C (b) and room temperature after heating (c). The in-situ scratch depths increase almost linearly with the load and shows "jump points" at depths of about 3~4 nm where the probe is penetrating through the 3 nm thick coating.

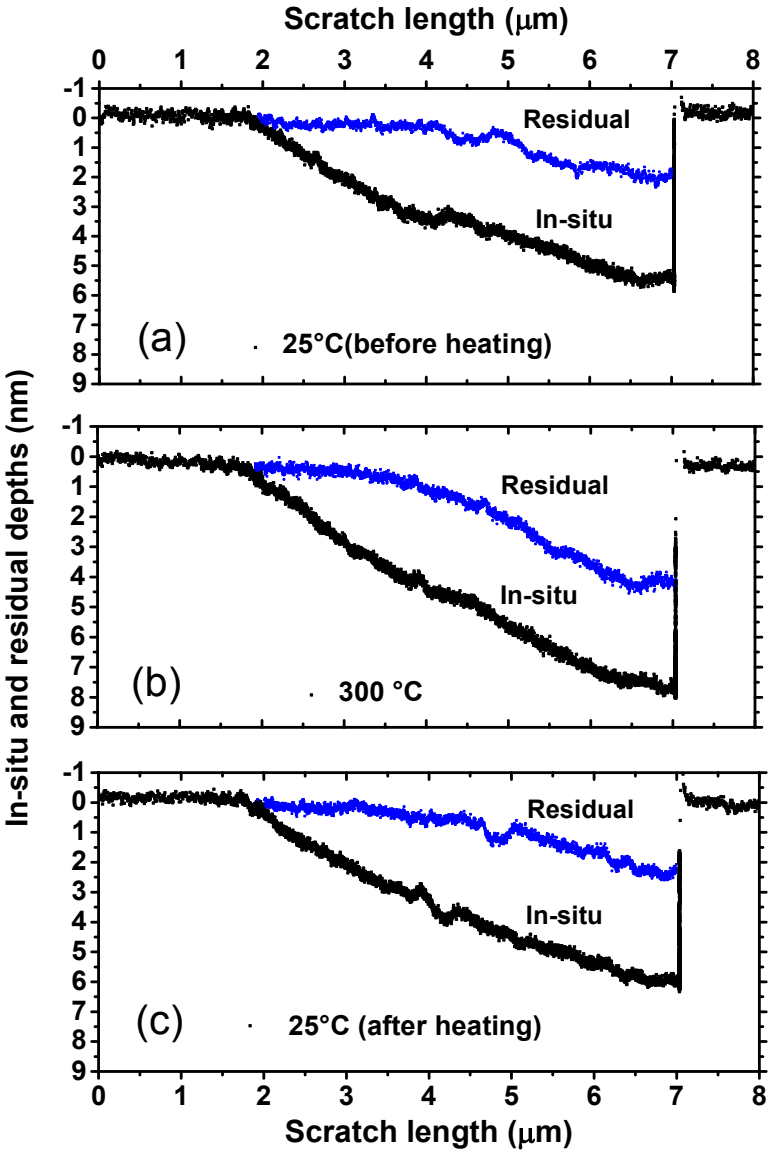

Figure 5.5 In-situ and residual depths versus scratch distance for ramp-load scratch experiments using peak normal load of 30 μN at temperatures of (a) 25 °C before heating, (b) 300 °C and (c) 25 °C after heating; The prescan step corresponds to scratch length from 0 to 2 μm; the scratch step corresponds to the scratch length of 2 μm to 7 μm; the post scan step initiates at 8 μm.

Fig. 5.6 shows the atomic force microscopy (AFM) images for the scratch marks after the scratch experiments at 25 °C (before heating), 300 °C and 25 °C (after heating). The ramp-load scratch experiment causes a groove after the probe plowing on the sample.

With the same height scale, the grooves provide visual characterization of the extent of wear. Before heating, the carbon film shows very slight wear near the peak load, while at 300 °C, the scratch mark is deeper and initiates at much smaller force. Note that in both cases the scratch is initiated at 0.5 μm away from the top of the image and completes at the bottom of the image (5 μm long).

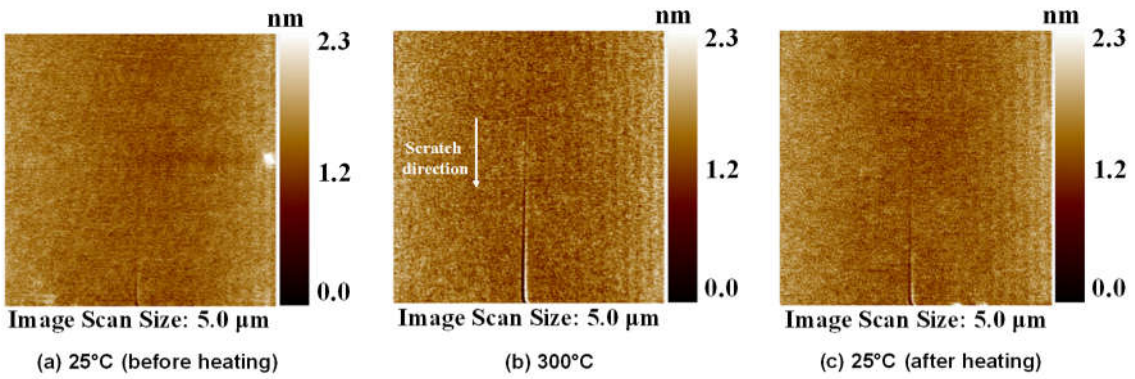

Figure 5.6 AFM images of ramp-load scratches at (a) 25 °C before heating, (b) 300 °C and (c) 25 °C after heating.

Fig.5.7 displays the extracted quantitative results for the in-situ and residual depths at the peak load. Both in-situ and residual depths show similar variation trends. They increase with temperature and cannot recover after heating, implying irreversible reduction of wear resistance. Please note that NiP has a higher hardness and constant elastic modulus at elevated temperature of 400 °C (Higgs, 1974). Thus, the increased in-situ and residual depths could be attributed to softening of the carbon film.

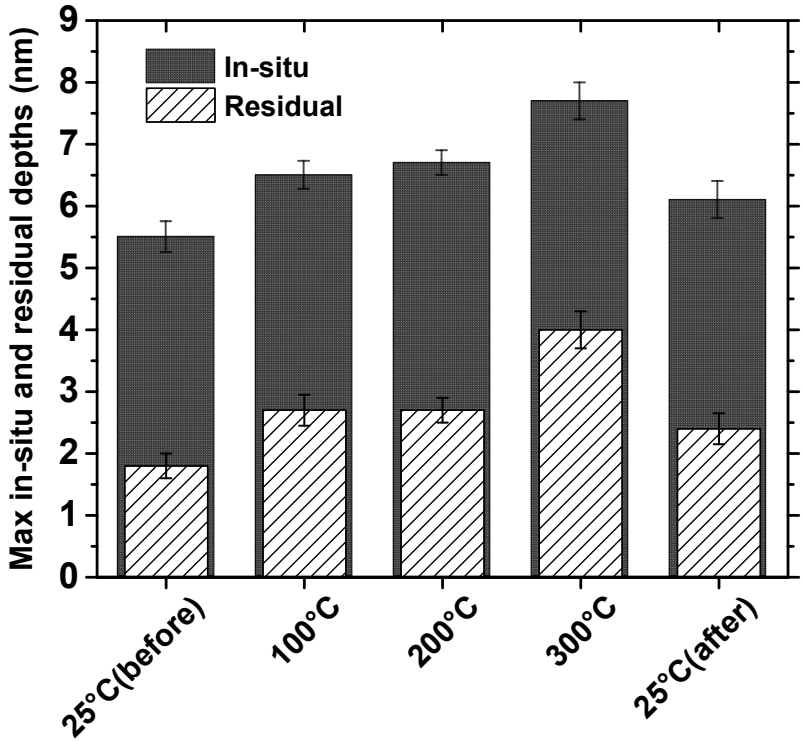

Figure 5.7 Maximum in-situ and residual depths at the peak load of 30 μN at different temperatures.

5.3.1.2 Friction coefficient

Low friction resistance is an important advantage of a:C-H films as coating materials. Fig. 5.8 reports the in-situ friction coefficient during the ramp-load scratch experiments. All friction coefficients are high at the beginning and then tend to be constant. At the initial stage of nanoscratch experiments, the friction coefficient is usually high because of small normal force values (being zero at the initiation of the scratch). As the normal force increases (F > ~10 μN) and the in-situ scratch depth is deeper (h > 2~3 nm), in all cases, the friction coefficient tend to be constant. Another interesting finding is that after heating, as shown by Fig. 5.8 (c), the initial friction is much lower than before heating. Note that during cooling down, the probe is withdrawn from the sample so there is no inert

gas provided on the sample surface. Oxygen in the environment can promotes graphitization on the surface and this low friction region is the indicator of a graphitized surface layer. Also note that such a stronger graphitization only reduces the friction coefficient at the top surface in light contact. As the normal force increases, the friction coefficient increases and converges to a constant value, as shown in Fig. 5.8 (c).

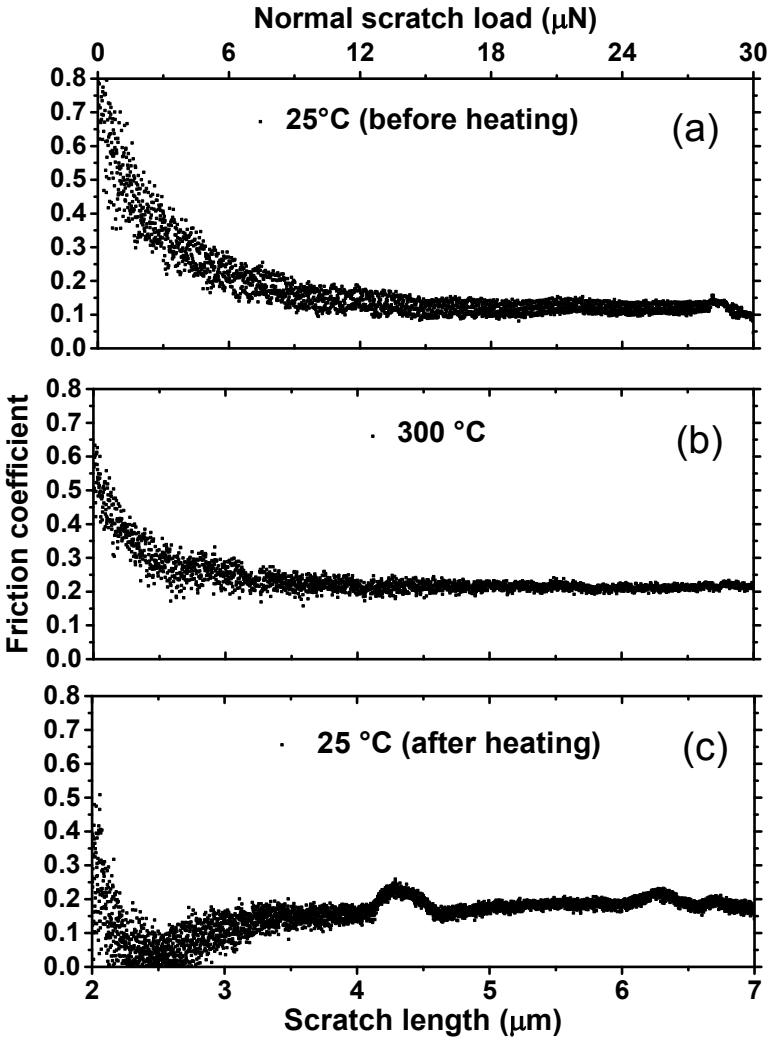

Figure 5.8 In-situ friction coefficient from the ramp-load scratch experiments at temperature of (a) 25 °C before hating, (b) 300 °C and (c) 25 °C after heating.

Fig. 5.9 summarizes the friction coefficients after reaching convergent values. The friction coefficient at room temperature is 0.12, which is in good agreement with the experimental data that reports friction coefficients for ultra-thin amorphous carbon films ranging from 0.1 to 0.16 (Bhushan, 1999; Tsui et al., 1995). As the temperature increases, the friction coefficient increases up to 0.22 at 300°C. After cooling down, the friction coefficient remains at a higher value of 0.17. This finding agrees well with the experiment by Cui *et al.* who observed higher friction coefficients accompanying with higher degrees of graphitization at room temperature (Cui et al., 2014). Based on the phenomenon, Cui *et al.* concluded that passivation of dangling bonds plays a more dominant role in the lubrication mechanism of a-C:H coatings (Cui et al., 2014).

A widely used theory for interpretation of the friction coefficient during sliding was proposed by Bowden and Tabor (2002). The theory attributes the friction coefficient to two components: a deformation friction coefficient μ_{def} and an adhesive friction coefficient μ_{adh}. The deformation term is due to the resistance for ploughing the asperities of the harder surface through the softer. At higher temperature, material softening occurs, as shown by Fig. 5.6, and the deformation friction should be larger. The adhesive friction is due to attractive forces at the asperity contacts.

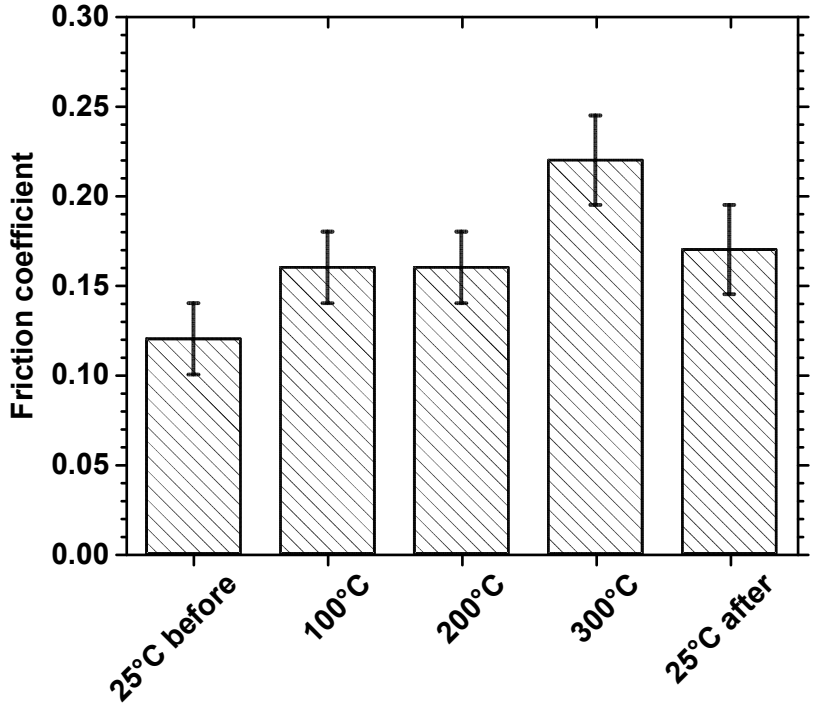

Figure 5.9 Average friction coefficient values of nanoscratch experiments at scratch load of 12 μN at different temperatures.

There are simple analytical expressions for deformation friction coefficient for a rigid stylus/probe plowing on a surface. For a spherical probe, the friction coefficient due to plowing deformation is (Hamilton, 1983):

$$\mu_{def} = \frac{4r}{3\pi R} \; or \; 0.6\sqrt{\frac{h}{R}} \tag{5.2}$$

, where r is the width of the in-situ scratch groove, R is the rigid tip radius and h is the in-situ scratch depth (as shown in Fig. 5.4 (a)). Using Eqn. (5.1), we can estimate that the deformation friction coefficient at the maximum scratch depth (h=5.5 nm) is μ_{def} = 0.126 at room temperature before heating; μ_{def} = 0.137 at 100°C; μ_{def} = 0.139 at 200°C; μ_{def} = 0.149 at 300°C and μ_{def} = 0.133 after heating. The simple friction model given by Eqn.

(5.1) works well in predicting the coefficient at room temperature before heating, but it underestimates the increase of the friction coefficients with temperature. The main reason is that the adhesive friction component increases with temperature, which is additive to the deformation friction coefficient.

From above analysis, it can be seen softening of the material at higher temperature is responsible but not the primary reason for the significant increase of friction at high temperature. The rest of increase of the friction coefficient should be attributed to change of adhesion. Molecular simulations revealed that unsaturated carbon atoms in the a-C:H film (sp^2 carbon) can undergo chemical reactions that lead to adhesion between the diamond tip and the film, increasing the friction (Gao et al., 2002). Addition of hydrogen atoms to the a-C:H film saturates these sp^2 and thus reduces adhesion induced friction.

The hydrogen content is reduced at higher temperature, leading to more unsaturated sp^2 on the surface. In addition, sp^3-to-sp^2 conversion also increases sp^2 on the film surface. The two changes together cause stronger adhesion between the diamond tip and the film, which supports the passivation mechanism. The reduced friction coefficient after cooling down is attributed to the graphitized surface layer, indicated by the low friction region for light contact in Fig. 5.8 (c).

Surface roughness is an important factor determining which of the two mechanisms is more dominant. For smooth samples, there are more asperities concentrated in a similar height and the integrated adhesion force is strong (Chang et al., 1988; Suh and Polycarpou, 2005). Thus, the contribution from adhesion to the friction coefficient is significant, so the passivation mechanism can well explain changes of the

friction coefficients, as shown in present experiments. However, for rough surfaces, the passivation mechanism is less applicable as there adhesion has insignificant effects on the friction coefficient. In such a case, material properties of the surface are dominant in determination of the friction coefficient and the graphitization mechanism can well explain the friction behaviors. In present experiments, a rigid spherical surface is contacting with a deformable smooth surface, which can be taken as a single asperity contact. Results in Fig. 5.8 describe dependence of friction coefficients on temperature and interference depths and would be beneficial to development of contact mechanics at high temperature.

5.3.2 Nanowear experiments

Nanowear experiments (also referred to as wear scanning experiments) are commonly used to determine the wear resistance of DLC coatings (Bhushan, 1999; Lee et al., 2006; Prabhakaran and Talke, 2000). Such experiments utilize a diamond indenter (the same as for the scratch experiments above) to scratch repeatedly over a square area of the sample with a preset normal load to generate wear, as depicted in Fig. 5.10. After a complete wear experiment, the indenter rescans a larger area including the worn region with a light contact force (2 μN) to measure the residual morphology/worn area. The Hysitron Triboview software provides a means to directly calculate the average depth and wear volume. The average wear depth can be measured by subtracting the mean height of the worn square region from the mean height of the unworn region outside of the square. Then the wear volume is given as the square of the scan size multiplied by the measured wear depth. In such a way, nanowear experiments can quantitatively determine and

compare the wear resistance of different samples, at different contact pressures, and different temperatures.

In the present set of experiments, wear scanning tests were conducted over a 2×2 μm square region on the a-C:H coated sample. The wear scans contained 512 consecutive line scratches along one direction with a velocity of 4 μm/s. A full scan test takes 256 s, and after each wear experiment, the indenter rescans a 5×5 μm region with the worn area at the center (using the same probe).

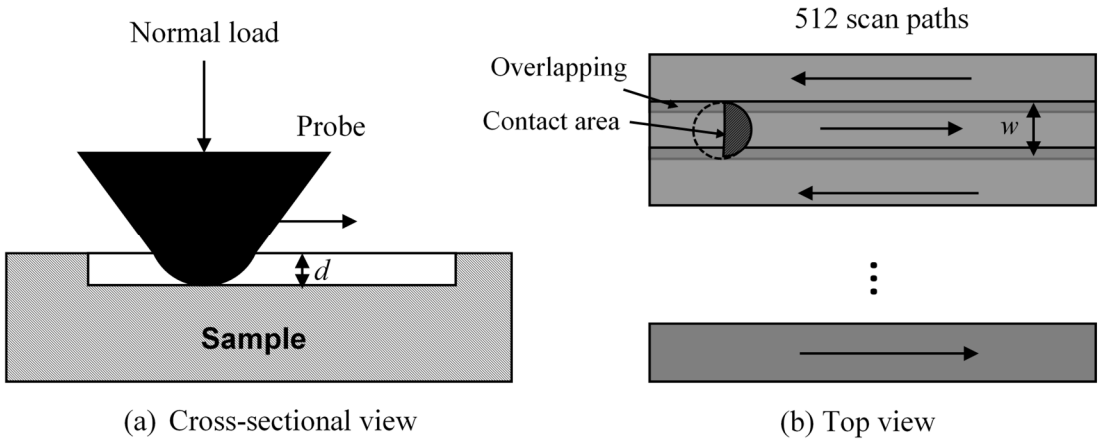

Figure 5.10 Schematic view of nanowear experiments (a) cross-sectional view and (b) top view.

5.3.2.1. Wear analysis

The normal load, and thus the contact pressure is an important parameter for these experiments. It is necessary to ensure that the normal load is sufficiently small so that the probe does not penetrate through the coating but also not too small to ensure causing wear. Referring to the in-situ nanoscratch depths in Fig. 5.7, at 300 °C the scratch depth is the largest and thus it is the most possible one for the probe to penetrate the coating. Thus, we

select a normal force of 10 μN causing an in-situ depth of 2.93 nm at 300 °C to ensure the probe scratches within the coating.

Table 5.1 shows the in-situ scratch depths at 10 μN for all the experiments. Once the in-situ scratch depth is determined, the in-situ scratch width *w* can be readily obtained, using the geometry of the rigid spherical tip of known radius. Further, the mean contact pressure can be estimated by dividing the load with the scratch contact area:

$$p = \frac{F}{\pi w^2/8} \tag{5.3}$$

Note that the scratch contact area is a half circle, as depicted by the shaded area in Fig. 5.10. As the temperature increases, the mean pressure decreases because of deeper scratch and larger contact area. In addition, the mean contact pressure at room temperature in Table 5.1 is similar to the hardness of DLC films measured by nanoindentation experiments (Bhushan, 1999; Lee et al., 2006; Tsui et al., 1995).

Two adjacent scans overlap by an amount that is determined by the scan width, *w*. Because of overlapping, the total scanned area is larger than the worn area (4 μm^2), as shown in Table 5.1. The smallest scanned area is 48.89 μm^2 at room temperature, and the largest is 56.72 μm^2, equivalent to about 12 and 14 repeated full scans respectively.

Table 5.1 Estimated scan depths, mean pressure, scan widths and scanned areas at a scratch force of 10 μN for different temperature (determined from nanoscratch experiments).

Temperature, (°C)	25 (before)	100	200	300	25 (after)
In-situ scratch depth, *d* (nm)	2.31	2.42	2.64	2.93	2.40
In-situ scan width, *w* (nm)	47.74	48.86	51.01	55.39	48.66
Mean pressure, *p* (GPa)	11.18	10.66	9.78	8.30	10.76
Total scanned area, A_s (μm^2)	48.89	50.03	52.23	56.72	49.82

Fig. 5.11 (a) to (e) show residual AFM images after the nanowear experiments. As shown by the arrow in Fig. 5.11 (a), in all tests the probe began scanning left to right from the top and finished at the bottom. The height or z-axis is auto-scaled to cover the minimum to the maximum range, and is thus different in each of the images. The minimum values represent the largest wear depth while the maximum values represent the largest pile-up height. It is observed that before heating, there is very slight wear with a maximum wear depth of 1.97 nm, and as the temperature increases there is significantly more wear within the worn region and more pile-up at the border, denoting that more intense material removal is taking place. After 200 °C, the maximum wear exceeds 3 nm, representing partial removal of the carbon coating material. 300 °C is more aggressive to the substrate or the media material for the case of hard disk drive samples that the carbon coating is designed to protect. The carbon film has a high wear rate even after cooling down to room temperature (annealed sample), as shown in Fig. 5.11 (e), showing that permanent damage had occurred on the DLC with heating to 300 °C.

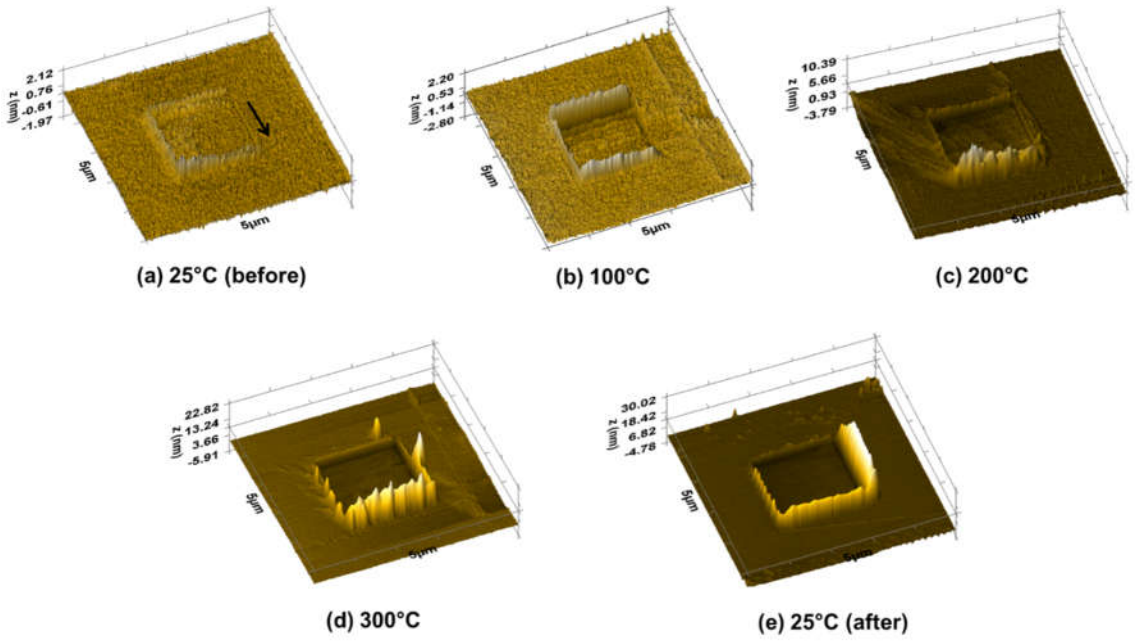

Figure 5.11 AFM residual images after nanowear experiments (10 µN) at different temperatures: **(a)** 25 °C before heating, **(b)** 100 °C, **(c)** 200 °C, **(d)** 300 °C and **(e)** 25 °C after heating/annealed.

Material pile-up is also observed in these measurements, with the height of the pile-up increasing with temperature, indicating more severe wear. During the nanowear experiments, wear debris was swept to the borders and accumulated there. So generally, there is more pile-up at the border where the tests finished, as shown in Fig. 5.11 (a) to Fig. 5.11 (d). The highest pile-up in Fig. 5.11 (e) is at the right border, indicating film delamination in this case. Thus, there are two types of wear mechanisms for the carbon coating studied herein, out of the four different wear mechanisms for ultra-thin carbon films described by Bhushan (1999). At room temperature, before heating, and at high temperature, plastic flow of material is primarily responsible for the wear of the coating, while for the annealed case with more graphitic structure, delamination and bulking are the main reasons for the coating wear.

Fig. 5.12 (a) shows section/line scans of the residual profiles averaged along the scanning direction at different temperatures, and Fig. 5.12 (b) shows the obtained average wear depth values. The wear depth is small (<0.1 nm) below 100 °C, which shows that under nominal operating conditions of room and near room temperatures, the COC is very durable and protects the magnetic media from contact and scratch with the recording head. When the temperature increases to 200 °C, the wear depth increases to about 0.5 nm, and the maximum wear depth (~1.2 nm) is observed at 300 °C. Therefore, the tribology performance of the COC coating was degraded by the elevated temperature and such degradation becomes significant at 300 °C, which correlates with the findings by Rose et al. (2014) who reported that the reduction of sp^3 content becomes rapid at 300 °C. When the sample is cooled down to 25 °C in the chamber without Argon gas, the wear depth still remains large (~1 nm), implying that the wear resistance of the COC film has been degraded irreversibly by high temperature, indicating a permanent change in the structure of the materials. The temperature dependence of wear depths correlates well with that of friction coefficients shown by Fig. 5.12. As discussed before, the increased adhesion is the main contributor to the increase of the total friction coefficient at elevated temperature, and it can be also the primary reason for increased wear.

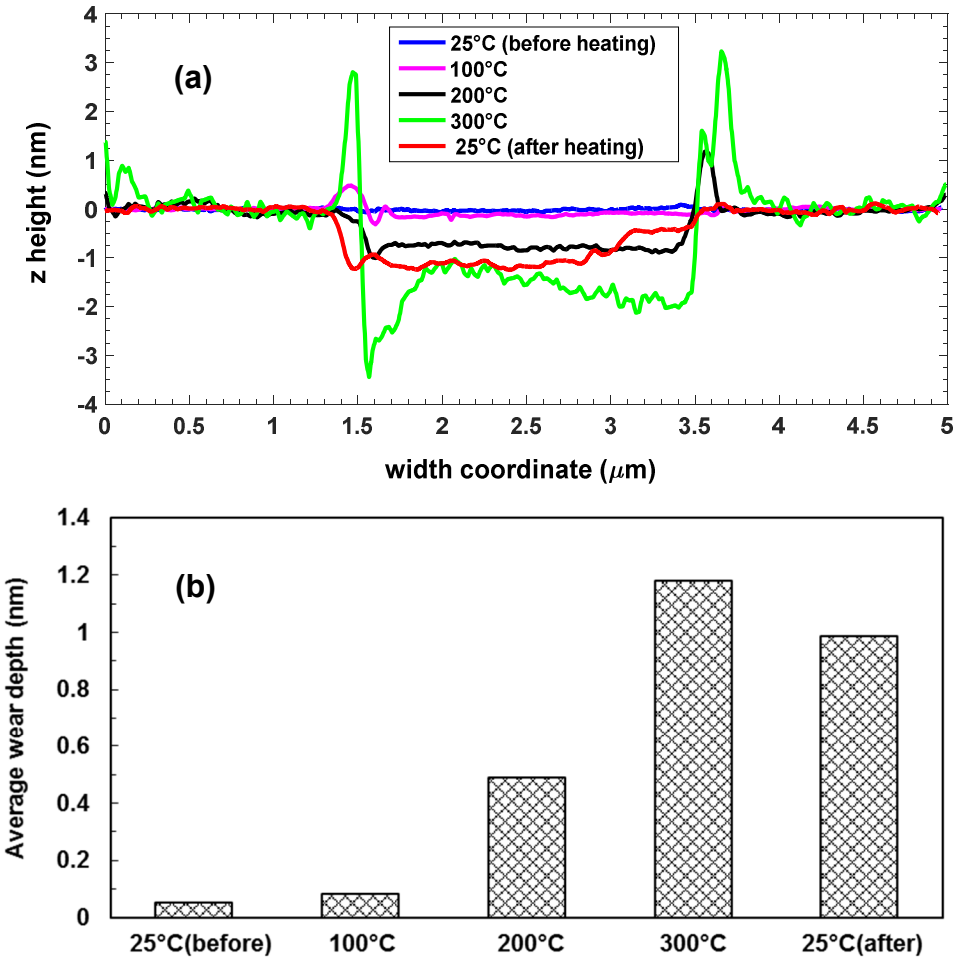

Figure 5.12 (a) Average line scans of residual wear profiles and (b) average wear depth values of the ultra-thin carbon sample at different temperatures.

There are two major mechanisms for degradation of wear resistance of a-C:H films at high temperature: these being the loss of hydrogen and conversion of sp^3 to sp^2 carbon bonding. According to the literature, the critical temperatures for the two mechanisms are reportedly different, namely, loss of hydrogen is reported to initiate at about 100 °C (Van der Donck et al., 2009) and sp^3-to-sp^2 conversion is reported to begin at 300 °C (Wang et al., 2013). Referring to the average wear depths shown in Fig. 5.12 (b), the slight increase

of wear rate at 100 °C is due to loss of hydrogen and the severe wear at 300 °C is attributed to sp^3-to-sp^2 conversion.

5.3.2.2. Wear and activation energy

The wear volume can be calculated by multiplying the wear depth with the worn area of 4 μm^2. The specific wear rate k and the dimensionless wear coefficient K is defined as (Archard, 1953):

$$k = V_w/(F \cdot d) \tag{5.4a}$$

$$K = HV_w/(F \cdot d) \tag{5.4b}$$

, where V_w is the wear volume, F is the normal load (10 μN), d is the total sliding distance equal to 1024 μm (2 μm length ×512 scans), and H is the hardness using values for mean contact pressure in Table 5.1. Based in Eqns. (3), Table 5.2 calculates the wear rates and wear coefficients at different temperatures. The wear rate at room temperature before heating is of the same order of magnitude as the test data for hydrogenated DLC films in the literature (Erdemir, 2001). But the values in the present study are generally higher, the main reason is that in the present study a sharper stylus is used and as a result the contact pressure is higher. Other than that, both the wear rate and wear coefficient increase with test temperature, representing severe wear. A reciprocal Arrhenius equation is widely used to express temperature dependence of the wear coefficient (Quinn, 1967):

$$K_w = Cexp(-E_a/k_bT) \tag{5.5}$$

, where k_b is the Boltzmann constant (8.617×10^{-5} eV/K), E_a is the activation energy and T is the temperature in Kelvin (K). The activation energy describes the minimum energy required to cause a chemical change.

Table 5.2 Wear coefficient values of the a-C:H film at different temperature.

Temperature (°C)	**25 (before)**	**100**	**200**	**300**	**25 (annealed)**
Wear rate, k (mm^3/Nm)	2.04×10^{-5}	3.27×10^{-5}	1.89×10^{-4}	4.54×10^{-4}	3.80×10^{-4}
Wear coefficient, K_w	2.28×10^{-4}	3.49×10^{-4}	1.85×10^{-3}	3.77×10^{-3}	4.09×10^{-3}

Fig. 5.13 plots the natural logarithm of the wear coefficient, $ln(K_w)$, with the reciprocal of the temperature, $1/T$. The linear relationship can be used to fit the data and from its slope the activation energy can be obtained, E_a=2002.1×8.617×10^{-5}=0.1725 eV. This value is much lower than that from laser irradiation experiments by Jones et al. (0.6 eV) (Jones et al., 2014) but agrees very well with that for ordering and clustering of sp^2-hybridized carbon from the XPS study by Mangolini et al. (2013) (0.18 eV). This correlation implies that the ordering and clustering of sp^2 is a gradual process initiating at the very beginning of heating (100 °C) in the present high-temperature experiments.

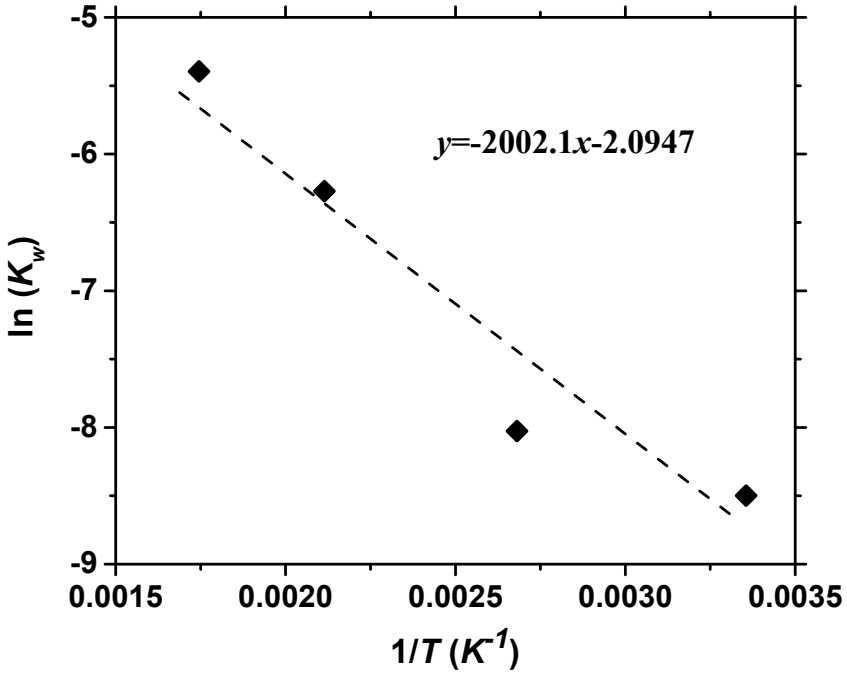

Figure 5.13 Relationship for logarithm of the wear coefficient $ln(K_w)$ with reciprocal of temperature $1/T$, with an R-squared value of 93%. The slope of the fitted linear relation is $-E_a/k_b$.

5.3.3 Structural studies using Raman Spectroscopy

Two key parameters determining the structural properties of DLC films are the fraction of sp^3 and the hydrogen content. Both parameters can be studied using Raman spectroscopy, which is a standard non-destructive and commonly used tool for characterization of carbon-containing materials. In the visible Raman spectra of any carbon material, D (for "disorder") and G (for "graphite") bands are important features containing information about the structural and bonding characteristics of the material of interest. The D mode, with a wave number of about 1350 cm^{-1}, is due to breathing of aromatic (six-fold) rings that exist both in sp^2 and sp^3 sites. The G mode, at a wave number of about 1580 cm^{-1}, is due to stretching modes of sp^2 sites only, whether in C=C chains or

in aromatic rings. Therefore, for highly pure diamond that has a very small fraction of sp^2 sites, the D mode is very intense. While in graphite where sp^2 sites are dominant, the G mode is very strong. Amorphous carbon has both sp^3 and sp^2 hybridization.

For a-C:H films, the C-C bonds network strongly depends on its hydrogen content, which links the sp^2 and sp^3 phases together. This makes possible the sp^3 content to be indirectly derived from the Raman spectrum. Specifically, the sp^3 content can be correlated to the G peak wavenumber and the ratio of D and G peak intensities, I(D)/I(G), of the Raman spectrum (Tamor and Vassell, 1994; Ferrari and Robertson, 2001; Casiraghi et al, 2005; Pardanaud et al., 2012). The hydrogen content can be qualitatively evaluated from the slope of the Photoluminescence (PL) background (Marchon et al., 1997; Adamopoulos et al., 2004; Casiraghi et al., 2005).

In the present study, Raman characterization experiments were performed on two a-C:H films with larger thickness (11 nm) than that used for tribology testing, in order for the Raman spectra to capture enough chemical information. The first sample has no heat treatment and the second sample is heated to 300 °C for 15 mins and then cooled down naturally to 25 °C in the presence of Ar to exclude any oxidation. Raman spectra obtained over the two samples are presented in Fig. 14. There are mainly three variations for the spectrum of the heated sample compared with that of the unheated one: (1) decrease of the PL slope; (2) increase of the I(D)/I(G) ratio; (3) slight shift of the G peak to a higher wave number (red-shifting); (4) decrease of spectrum intensity.

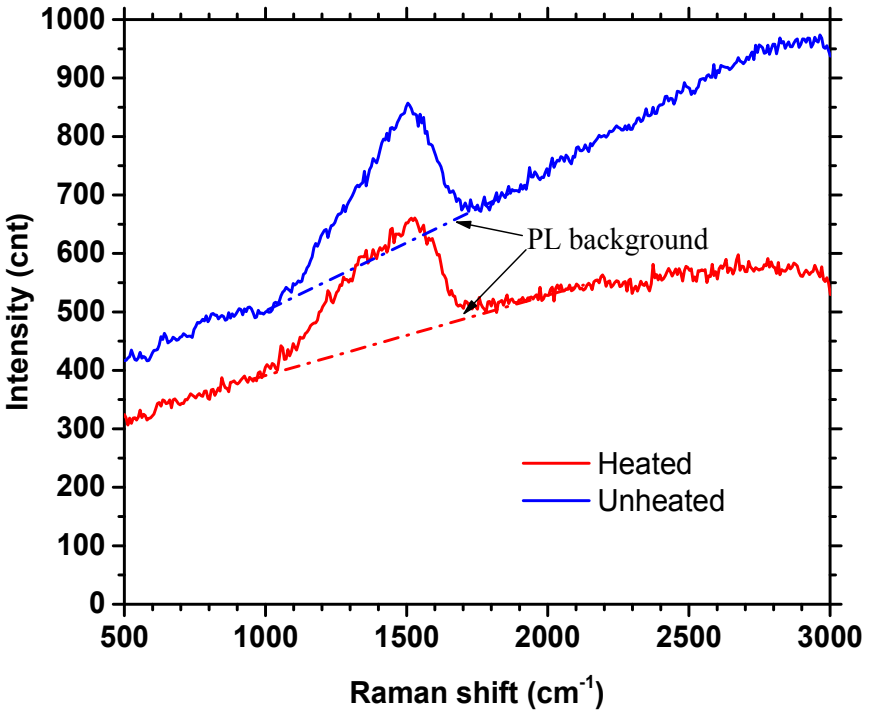

Figure 5.14 Raman spectra of the COC sample before and after annealing to 300 ºC. The G peak shifts from 1504 cm^{-1} to 1528 cm^{-1} after annealing.

Decrease of the PL slope is significant and it is a strong indicator that there is less hydrogen in the sample after heat treatment (Marchon et al., 1997; Adamopoulos et al., 2004; Casiraghi et al., 2005). The intensity ratio of D and G modes, I(D)/I(G), is proportional to the number of aromatic rings at the edge of the graphite domain and thus the size of the domain. Increase of the I(D)/I(G) ratio indicates clustering of sp^2 sites into a bigger domain. Though, it is not evident if there is sp^3-to-sp^2 transformation because ordering of sp^2 sites without reduction of sp^3 is also possible. Slight red-shifting of the G peak can be correlated with reduction of hydrogen content as well as reduction of sp^3 content. In reality, reduction of both hydrogen and sp^3 content occur simultaneously. In conventional PECVD a-C:H films, a higher sp^3 content correlates with a larger hydrogen

content. This is because hydrogen converts sp^2 C sites into sp^3 $=CH_2$ and $\equiv CH$ sites. Therefore, the a-C:H with maximum hydrogen content has a high sp^3 content. On the other hand, loss of hydrogen will cause formation of sp^2-hybridized carbon from sp^3 sites. Therefore, effusion of hydrogen can be another reason for reduction of sp^3 sites. The last change, decrease of intensity, is due to loss of carbon atoms to the environment during heating. Similar phenomenon was observed by Jones *et al*. (2014).

Combined with the curve-fit relation in Fig. 5.13, present Raman analysis indicates at high temperature the carbon film has experienced the following gradual changes/transformations. The first change is hydrogen effusion and emission, as it requires the lowest activation energy and temperature (<150 °C) (Peng et al., 2016). One consequence of hydrogen effusion is sp^3-to-sp^2 conversion given risen by scission of both sp^3=CH_2 and $sp^3\equiv CH$ bonds that subsequently promotes formation of sp^2-hybridized carbon. These changes do not require high activation energy (high temperature) but gradually lead to clustering and ordering of sp^2.

5.4 Summary of Chapter 5

The present chapter investigates nanotribological properties of a 3 nm a-C:H carbon film through nanoscratch and nanowear experiments utilizing a high-temperature nanomechanical system. The nanoscratch experiments capture *in-situ* friction coefficient and deformation of the film under scratching at high temperature. The nanowear experiment measure wear rates of the carbon film under repeated scratches. The findings can be summarized as following:

(a) Through nanoscratch experiments, we present temperature dependence of the friction coefficient of the 3 nm carbon coating. The friction coefficient increases dramatically with temperature and its value almost doubles at 300 °C comparing with that at room temperature. Considering that the present sample is super-smooth, we attribute the increase of friction mainly to stronger adhesion between the probe and the film after hydrogen effusion.

(b) The nanowear experiments reveal that the wear coefficient of the coating increases exponentially with temperature. An activation energy is obtained by fitting temperature dependence of the wear coefficient. The value of the activation energy correlates with that for clustering of sp^2, indicating graphitization in the inert environment at elevated temperature is a gradual process.

(c) The Raman spectra mainly reveal that after heat treatment the carbon coating has experienced increase of sp^2 cluster size, reduction of both hydrogen and sp^3 contents and carbon loss. These changes are all mechanisms to explain degradation of the wear resistance, but the most critical change is hydrogen loss that leads to gradual sp^3-to-sp^2 conversion and graphitization even in an inert environment. Exposure to oxygen at high temperature greatly increases the degree of graphitization on the surface of the a-C:H film to form a low-friction surface layer, as shown by Fig. 5.8 (c).

6 MOLECULARLY THIN LUBRICATION MODEL CONSIDERING RHEOLOGICAL BEHAVIOR AT THE NANOSCALE

6.1 Introduction to molecularly thin lubricants

The spacing or clearance between the read/write elements of the recording head and the disk has decreased to less than 5 nm to increase the areal density of magnetic storage, with current recording densities of the order of 850 Gbit/in^2. As a result, there is a higher possibility of direct contact between the head and the disk. To protect the magnetic media layers from damage, a layer of molecularly thin lubricant is utilized on the disk surface (in addition to the hard protective carbon overcoat). To investigate how lubricant helps protect the media, it is important to study the sliding contact of the head and disk in the presence of a molecularly thin lubricant at the interface. Previous work has addressed the lubricant physical mechanisms and developed the governing equations for the Molecularly Thin Lubricant (MTL) model (Vakis et al. 2011; Vakis and Polycarpou 2012; Vakis and Polycarpou 2013; Chowdhury et al. 2015). The objective for the MTL model is to account for the hydrodynamic forces in the lubricant by combining the point lubrication theory with the Greenwood-Williamson (GW)-type rough surface model (Greenwood and Williamson 1966). The point contact lubrication theory solves for the hydrodynamic pressure and force of liquids under shear, and the GW rough surface model provides a mathematical approximation for asperities on rough surfaces. By integrating

* Reprinted with permissions from "A single asperity sliding contact model for molecularly thin lubricant" by Y. Zhang and A.A. Polycarpou, Microsystem Technologies 2017, 23, 1733-1741. Copyright (2017) by Springer.

the forces in the solid and lubricant contact regimes, the MTL model is able to provide predictions on contact forces including "bearing effects" from the lubricant layers of rough surfaces under relative sliding/shear.

Molecularly thin lubricants on the head-disk interface (HDI) behave differently from their bulk states. Contact and shear motions make the physics more complex. Building on the previous MTL model, the present study improves the earlier model by specifically modeling the nanobehavior of the lubricant under shear. Specifically it includes the MTL bonded ratio, the slip length and shear thinning, which were ignored in the earlier MTL model.

6.2 Behaviors of molecularly thin lubricant under shear

6.2.1 Rheology of polymer lubricant film

Conventional fluid mechanics assume that the lubricant behaves as a Newtonian viscous fluid whose shear stress is linear with the shear rate, i.e., $\tau = \mu\dot{\gamma}$. However, many complex fluids such as polymers show solid-like (elastic) behavior under certain conditions. The Pipkin diagram (Macosko 1994) shown by Fig. 6.1 (Barnes, 2000) qualitatively depicts the rheological mapping of liquids based on two numbers. The Deborah number is defined by the relaxation time λ divided by the characteristic time t_f, i.e., $De=\lambda/t_f$, or $\omega\lambda$, where ω is the excitation frequency. This dimensionless number is meant to quantify that "everything flows" (Reiner 1964). That is, everything, even rocks and steels, have liquid-like properties. The higher the Deborah number, the more solid-like the material is.

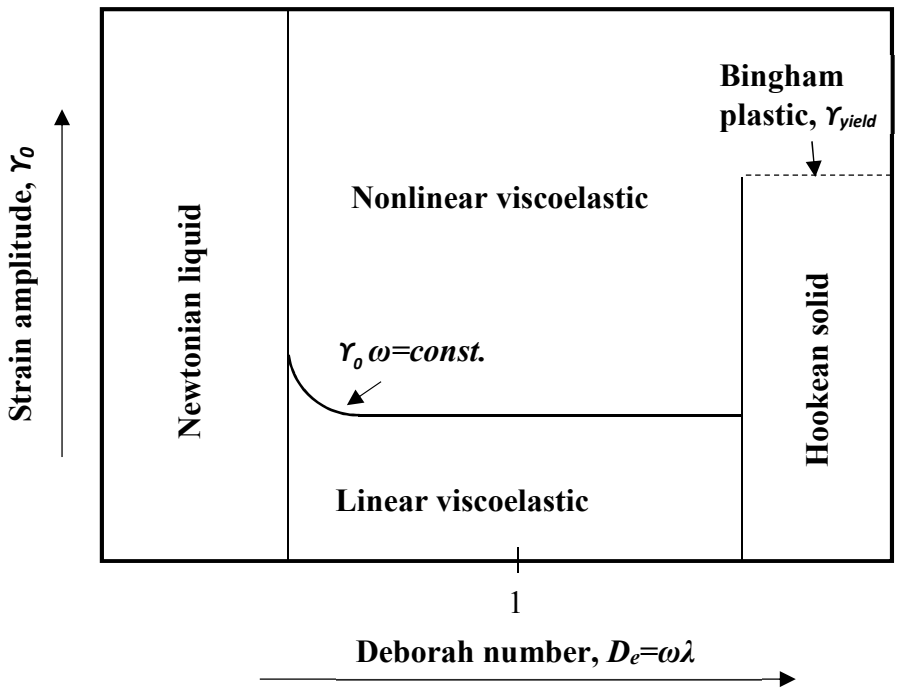

Figure 6.1 Pipkin diagram for different flow regimes of visco-elastic liquids (adapted from Barnes, 2000). When D_e is small, the shear stress is linear with the strain and the material is considered as Newtonian liquid; When D_e is very large the material is showing linear elastic behavior but Bingham plastic materials behaves as a viscous fluid as the strain is larger than γ_{yield}. Between the Newtonian and Hookean regimes the material shows viscoelastic behavior. The visco-elasticity is linear at low strain values and nonlinear at high strain values.

Table 6.1 gives the visco-elastic properties and relaxation times of some common materials (Barnes 2000; Hirz et al. 1992). The PFPE type lubricants are reported to have a relaxation time of ~10^{-7} s or smaller (Hirz et al. 1992; Kausik et al. 2006). The Deborah number increases with the relaxation time, corresponding to a higher likelihood of solid-like behavior. As two extremes in Table 6.1, water is the least solid-like material and glass is the most solid-like material. However, most polymers are neither pure liquid-like nor solid-like, but show characteristics of both. As for PFPE type lubricants, the Deborah

number, $\omega\lambda$, is far less than 1 provided with an excitation frequency of the HDD spindle (100~200 Hz), which implies that the PFPE lubricants on HDD should behave more liquid-like according to the Pipkin diagram.

Table 6.1 Relaxation times of different materials, λ (Barnes, 2000 and Hirz et al., 1992).

Liquid	Water	Oil	Polymer solution[1]	Polymer melt[1]	Glass	PFPE Z
Relaxation time, λ(s)	10^{-12}	10^{-9}	0.1	10	10^{5}	3.4×10^{-7}

Note that the Pipkin diagram cannot provide any quantitative analysis for a certain rheology problem, e.g., the head sliding through a monolayer lubricant on the disk surface. To achieve that, experimental works have been done to measure the visco-elastic properties of liquids. Gee et al. (1990) experimentally observed the transition between liquid-state and solid state of polymers under shear, leading to the stick-slip phenomenon. Ruths and Granick (1999) experimentally measured the viscosity and elasticity of PFPE Z-type lubricants. Experiments by Itoh et al. (2008; 2014) reveal that viscosity is still more dominant than elasticity in a nanonarrow gap filled with PFPE lubricant. Molecular dynamics (MD) simulations by Persson et al. (2002) also show that molecularly thin lubricants between two relatively sliding rough surfaces behave more liquid-like. These experiments and MD simulations provide the foundation for the current model that considers the lubricant as a liquid. Up-to-date modeling work on lubricant flow of HDI also assumes the lubricant as a continuum liquid and makes reliable predictions (Mate et al. 2010; Li et al. 2011).

6.2.2 Lubricant structure

Before further discussion of the Molecularly Thin Lubrication (MTL) model, it is necessary to introduce the polymer-based lubricant used in hard disk drives. Perfluoropolyether (PFPE) lubricants are widely applied in micro devices for several reasons: low surface tension so it can easily spread on solid surfaces; good chemical and thermal stability to minimize degradation; low vapor pressure; strong adhesion to the substrate through functional bonds; and good lubricity for protection against contact and wear. PFPE lubricants share similar structures as:

$X\text{-}O\text{-}[OCF_2\text{-}CF_2]_m\text{-}[OCF_2]_n\text{-}X$ (m/n~2/3).

They all have $\text{-}[OCF_2\text{-}CF_2]_m\text{-}[OCF_2]_n\text{-}$ as backbone structure and the difference relies on the X which is the end group. PFPE Z has CF_3 as the end group and PFPE Zdol has CF_2CH_2OH end group. Zdol has two hydroxyl groups (-OH) that promote bonding to the substrate. Researchers have developed PFPE Z type lubricants with more hydroxyl groups at the ends, such as Ztetraol and ZTMD. The chemical formulas for the three types of PFPE lubricants are listed in Table 6.2.

Table 6.2 Three types of PFPE lubricants

Type	Backbone	End groups (X)	Solid interaction
Z	$\text{-}[OCF_2\text{-}CF_2]_m\text{-}[OCF_2]_n\text{-}$	$\text{-}CF_3$	Weak
Zdol		$\text{-}CF_2CH_2OH$	Moderate
Ztetraol		$\text{-}CF_2CH_2OCH_2CHCH_2OH$ | OH	Strong

6.2.3 Bonded ratio

There are two layers of the lubricant film coated on the solid surface. The layer near the solid surface is strongly bonded with the substrate while the top layer is mobile, as depicted schematically in Fig. 6.2. The immobile layer is called bonded layer and the fraction of the bonded layer thickness to that of the total thickness is called the bonded ratio. The bonded ratio plays an important role in the lubricant's performance. Kato et al. (2004) experimentally investigated effects of the bonded ratio on the friction coefficient and durability of PFPE lubricants. Their experiments revealed that a higher bonded ratio helps the lubricant last longer. Li et al. (2011) and Waltman et al. (2010) found that a lower bonded ratio causes more lubricant transferred to the slider. The present analysis assumes that the bonded layer is strongly attached to the solid substrate through strong bonding, so the no-slip boundary condition is valid. Based on this assumption, the difference between the mobile and bonded layers will be discussed in later sections.

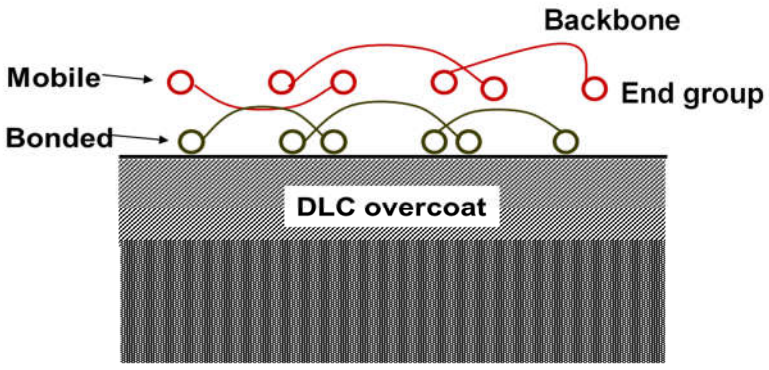

Figure 6.2 Chemical structure of the PFPE lubricant.

6.2.4 Shear thinning

Luengo et al. (1996) proposed a viscosity map with shear rate as shown in Fig. 6.3. In very narrow liquid gaps, solidification transition usually occurs, according to observations in the literature. Confined thin films also show higher viscosity than that in the bulk state. Itoh et al. reported an increased viscosity for Zdol 2000 in a confined liquid gap (Itoh 2008). On the disk surface, the shear rate, defined as velocity over the liquid gap, is very large. In such cases, the lubricant under shear experiences a viscosity drop due to the phenomenon called "shear thinning."

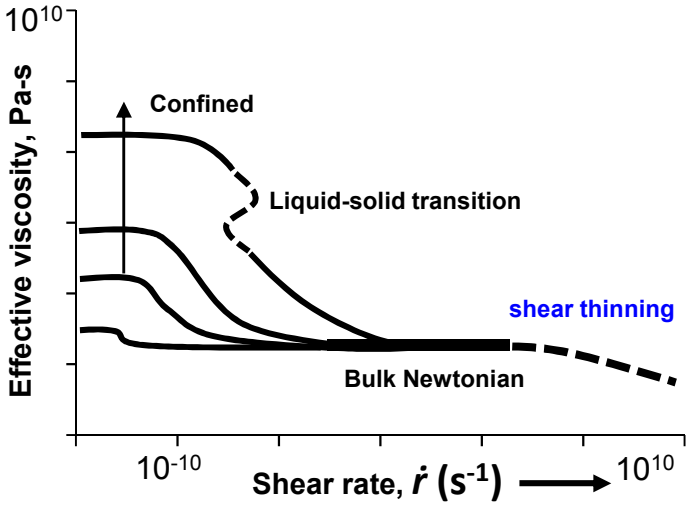

Figure 6.3 Viscosity mapping with the shear rate (adapted from Luengo et al., 1996)

6.2.5 Slip length

The concept of slip length is schematically depicted in Fig. 6.4. Zhu and Granick (2002) found that on very smooth surfaces, there is an obvious slippage on the solid-liquid interface and the conventional no-slip boundary conditions are not valid. They also found

that the slip length that denotes the extent of slippage varies with the shear rate and lubricant type.

Table 6.3 Literature test data for slip length values.

Surface	Liquid	Roughness, R_q (Å)	Shear rates (s^{-1})	Slip length (nm)	Ref.
Sapphire	Hexadecane	4	2- 10^4	175	Zhu and Granick, 2002; Pit et al., 1999
Sapphire+OTS				400	
Sapphire+STA				350	
Mica +HDA	Tetradecane	~1	10- 10^5	0- 1000	Luengo et al., 1996; Pit et al., 2000; Zhu and Granick, 2001; Zhu and Granick, 2002
Mica+OTE	Tetradecane			0- 1500	
Mica+2 PPO	Tetradecane	20		0-40	
Mica+OTE	Tetradecane			0-40	
Silica+gold+thiols	Sucrose sol.	6	10- 10^6	0-15	Zhu and Granick 2002; Craig et al., 2001
Mica/glass	1-propanol	10	10^2 - 10^6	10- 14	Neto et al., 2003
Borosilicate+HTS	Tridecane	3	10^2 – 10^5	10	Sun et al., 2002
	Tetradecane			15	
	Pentadecane			10	
	Hexadecane			20	
	Cyclohexane			10	
	Benzene			50	
	Aniline			50	
	Benzaldehyde			20	

Table 6.3 summarizes experimental data in the literature on the slip length of some fluids on smooth surfaces. The effects of slip length will be discussed later.

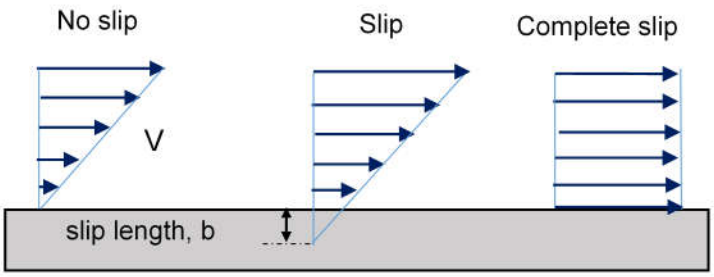

Figure 6.4 Velocity profiles for slip and no-slip conditions.

6.3 Theory

6.3.1 Effects of the shear thinning and slip length

Yamada et al. (2002) obtained a relationship between effective viscosity and shear rate from experiments for six different liquids. Cantow (1986) found a critical shear rate of 10^6 s^{-1} for the onset of shear thinning, of a PFPE Y-type lubricant. Hahm and Bhushan (1997) conducted similar experiments for PFPE YR and Z3 but did not find any shear thinning up to shear rates of nearly 10^6 s^{-1}. Itoh et al. (2014) proposed a model for shear thinning of PFPE lubricants based on measurements using a FWM (Fiber Wobbling Method) instrument. The present work summarizes the test data in the literature for shear thinning of PFPE lubricants, as shown in Fig. 6.5, and we propose a shear thinning relation by curve-fitting the data:

$$\mu / \mu_0 = (\bar{\gamma} / \bar{\gamma}_0)^{-0.9} \tag{6.1}$$

μ_0 is the viscosity at bulk state and $\bar{\gamma}_0$ is the critical shear rate where shear thinning begins to occur. The bulk viscosity μ_0 depends on the lubricant type and the critical shear rate is 10^6 s^{-1}.

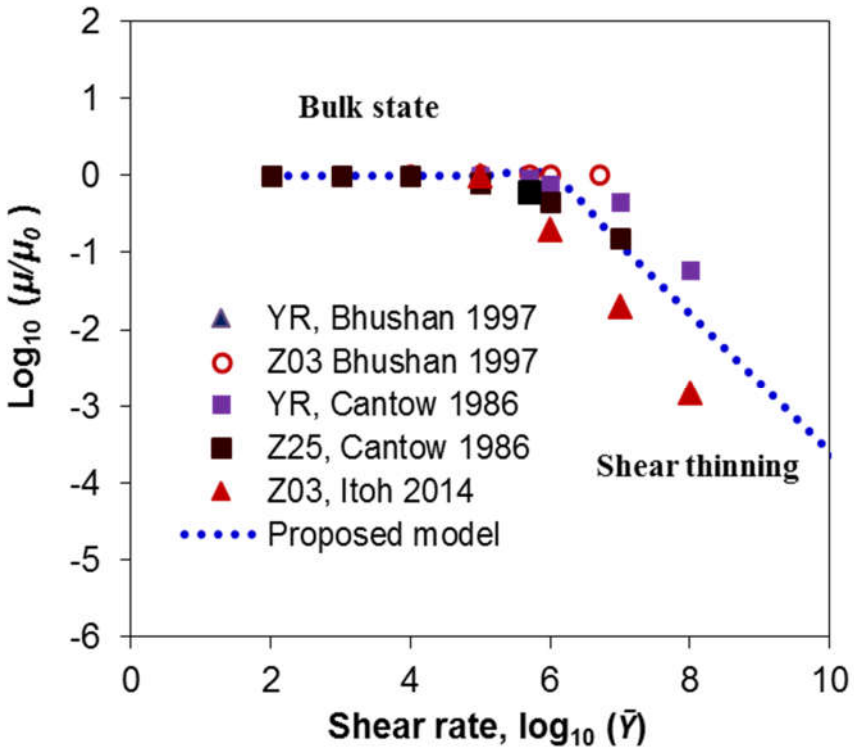

Figure 6.5 Effective viscosity values with shear rate.

Compared to shear thinning literature, there is very limited information in the literature about slip length of PFPE lubricants. The slip length is affected by many factors such as chemical structure, surface roughness and shear rates. Table 6.3 summarizes experimental data for some complex liquids on surfaces of similar roughness as the head disk interface. Since there is no specific test data for slip lengths of PFPE lubricants, estimation from other similar complex fluids is the most applicable method to use. The test data for slip lengths in Table 6.3 vary from 10 to 100's of nanometers, influenced by factors including surface roughness, liquid type and shear rates. In the present study, the roughness of the hard disk surface is small (< 1 nm), and the shear rate is very high (>10^{10} s^{-1}). And the slip length was found to increase with the shear rate by Zhu and Granick

(2002). Based on the measurements for complex fluids on similarly smooth surfaces with relatively smaller shear rates, it is assumed that the slip length of PFPE is above 10 nm.

6.3.2 Modified governing equations

The governing equation of the lubricant flow is a modified Reynolds equation with a slip factor f^* so as to both satisfy the continuity equation and account for the wall slippage. The detailed derivation is given in Appendix B. The modified Reynolds equation originates from the conservation of momentum and mass. The slippage factor is added on the RHS to account for flow rate due to slippage boundary condition. It varies between 1 and 0, corresponding to no-slip boundary and complete slip boundary, respectively.

$$\frac{\partial}{\partial x}\left(\frac{h^3}{12\mu}\frac{\partial p}{\partial x}\right)+\frac{\partial}{\partial x}\left(\frac{h^3}{12\mu}\frac{\partial p}{\partial y}\right)=\frac{\partial}{\partial x}\left[\left(1-\frac{f^*}{2}\right)h\right]U \tag{6.2}$$

, where

$$f^*= (U-U_W)/U= h/(b+h). \tag{6.3}$$

In Eqn. (6.2) and Eqn. (6.3), h, p, μ, and f^* represent film thickness, pressure, viscosity, and slip factor respectively. The present study investigates the lubrication for a single asperity, which is simplified as a plane sliding over a lubricated spherical surface, as shown in Fig. 6.6. Slippage is considered to exist on only one solid surface since the lubricant is designed to bond tightly with the disk surface. The minimum film thickness varies with the interference depth ω (penetration distance).

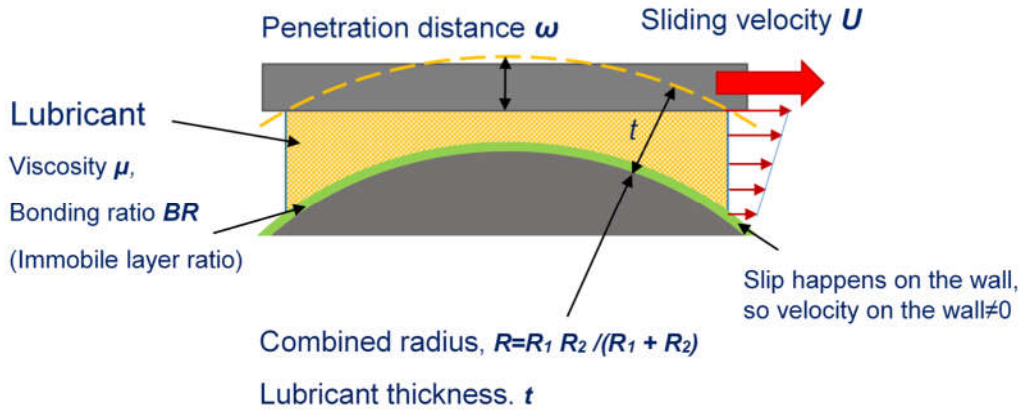

Figure 6.6 Geometry of a single-asperity model.

6.4 Results and Discussion

Numerical solution of Eq. (6.2) obtains the pressure distribution p, then the normal force P and the shear force Q. Fig. 6.7 depicts how the three variables change with the slip length ranging from 0 to 50 nm; the other parameters and their values are as listed in Table 6.4. The predicted values are asymptotically constant at slip length values larger than 10 nm, i.e., b>10 nm. Table 6.3 implies that for all tested complex fluids over smooth surfaces, the slip lengths are all larger than 10 nm. Therefore, it can be inferred that although the slip lengths for PFPE lubricants are not known precisely, the effect of slip length is conclusive based on the assumption that the slip length of PFPE lubricants is larger than 10 nm. The reason for this convergence is that the slip is complete, as shown in Fig. 6.4, when the slip length is larger than 10nm. In such a case, the slippage factor f^* is nearly zero, and the flow rate due to relative shearing between the two solid surfaces reaches maximum. Accordingly, the normal pressure increases but the shear force decreases.

Table 6.4 Parameters used in the simulation for the head-disk interface.

Parameters	Values
Relative sliding velocity, *m/s*	15
Radius of the protrusion tip, μm	0.7
Disk mean asperity radius, μm	0.43
Lubricant film thickness, *nm*	2
Bonded ratio	0.5
Minimum film thickness, *nm*	0.5
Lube (Zdol) bulk viscosity, *Pa-s*	0.3

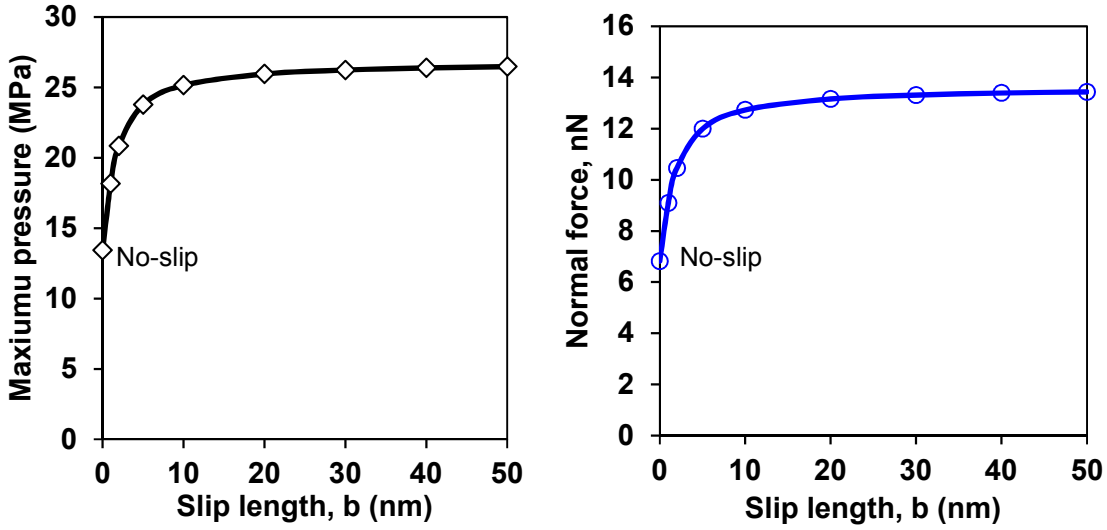

(a) Max pressure (b) Normal force

Figure 6.7 Calculated forces and pressure in the bonded and mobile layers as a function of slip length: (a) maximum pressure, (b) normal hydrodynamic force, (c) friction force.

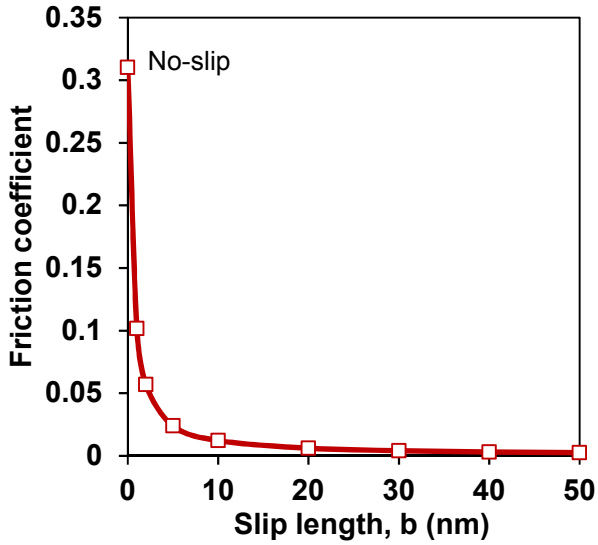

(c) Friction coefficient

Figure 6.7 Continued.

The effect of the lubricant bonded ratio has been considered to have a significant impact on HDI failures. Durability of disks with diamond-like carbon coated sliders is found to decrease with increasing bonded ratio, because the mobile lubricant helps to replenish the lubricant displaced during contact (Chen et al. 2001). Another explanation is that the severity of contact (or contact duration) increases as the bonded ratio increases (Karis et al. 2001). Experiments also reveal that the friction coefficient is higher in the bonded layer, which can induce mechanical wear (Kato et al. 2004).

Fig. 6.8 shows predictions for the maximum pressure and the friction coefficient for a fully mobile lubricant and a fully bonded lubricant, respectively. Because of slippage, the pressure is higher in the case of the mobile lubricant and the friction coefficient is almost zero. Thus, it can be concluded from the experimental literature (Chen et al. 2001;

Karis et al. 2001; Kato et al. 2004) that lower bonded ratio leads to lower friction coefficient, which is in agreement with the present simulation work.

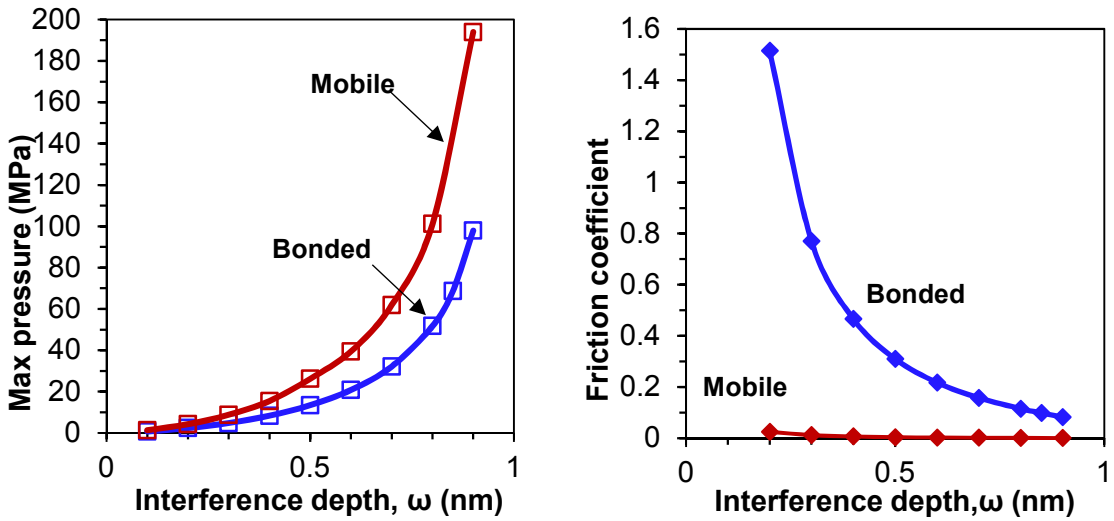

(a) (b)

Figure 6.8 Maximum pressure and friction coefficient versus interference depth.

Classical lubrication theory assumes pure viscous lubrication. This assumption may fail in the case of polymer lubricants that exhibit viscoelastic behavior. The present study discussed the viscoelastic mapping through the Pipkin diagram and then determined the influence of viscous effects through experiments in the literature. This discussion is important and paves the way for the proposed lubrication model considering the behavior of lubricant at the nanoscale, i.e., slip length, bonded ratio and shear thinning. Among the three phenomena, precise data on bonded ratio and shear thinning exist in the literature, but not for slip length. Based on the proposed model, variation of the slip length found that the hydrodynamic forces converge when the slip length is larger than 10 nm, which

is the case for PFPE lubricants. The proposed model relies on continuum mechanics theory, which is grounded on conservation of mass and momentum.

Recall that one objective of the current study is to investigate lubricant effects in the HDI. Results shown in Fig. 6.8 are examples of normal and shear forces between the slider and the disk asperities when they are contacting in the lubricant regime. The bonded and mobile layers show significantly different performance under sliding. The present theory would be instructive on evaluation of mechanical performances of different types of lubricants.

6.5 Summary

Dealing with molecularly thin films is challenging because: (a) the lubricant shows complex behavior at the nanoscale; and (b) certain assumptions in the classical mechanics literature are not valid. The present work tackled these complexities and proposed an improved model for bearing and shear forces for molecularly thin lubricants by: (a) using a logarithmic curve-fit relation between the viscosity and shear rate to account for shear thinning phenomena; (b) assuming validity of no-slip boundary conditions in the bonded lubricant; and (c) by applying a slip factor f^* to consider the slippage effects in the mobile lubricant. The present model relies in continuum mechanics theory, which is based on mass and momentum conservations. The improvement made in this work quantify the nanobehavior of lubricants and brings them into the continuum mechanics.

When dealing with the slip length, the present work found that the forces tend to converge if the slip length is larger than a certain value. This finding is important for the present analysis to ignore inconclusive information on slip lengths of lubricants used in

magnetic storage disks. The bonded ratio is another uncertain factor. The present work uses two extreme values for the bonded ratio (0 and 1). Comparison of the two extreme cases reveals that the friction coefficient increases with the bonded ratio, correlating with experimental observations. However, the present work is a model for a single asperity so it is unrealistic to benchmark exact values with test data, which tend to include surface roughness.

7 ADHESION INDUCED LUBRICANT TRANSFER AT THE HEAD-DISK INTERFACE OF MAGNETIC STORAGE DEVICES

7.1 Introduction to lubricant transfer at the head-disk interface

For protection against contact and corrosion both the disk and slider in a magnetic hard disk drive are coated with 1~2 nm thick diamond-like carbon layer (DLC), as shown by Fig. 7.1 (a). On top of the DLC, the disk is coated with an ultra-thin perfluoropolyether (PFPE) lubricant film. PFPE Zdol was selected as the lubricant of choice since the 1990s until recently when Zdol was replaced by PFPE Ztetraol and Ztetraol multidentate (ZTMD) that have more functional end groups, and thus offering stronger bonding with the carbon substrate (Kim et al., 1999; Watlman et al., 2010). Initially the slider has no lubricant, however it picks up PFPE molecules either from interaction with the disk surface during near-contact flying or from lubricant vapor during non-operation (slider parked off the disks). The net effect is that a thin lubricant film of similar thickness is formed on the slider as the one on the disk (Gao et al., 1999). Although the air-bearing flow may blow away the lubricant on the slider shortly after loading, its effect on the HDI (Head Disk Interface) is important before its removal.

Bonding ratio is also an important factor, affecting the occurrence of lubricant pick-up. Spacing is reportedly increased due to the lubricant accumulating on the slider, by an amount equal to the thickness of the mobile fraction of the lubricant (Mate et al.,

* Reprinted with permissions from "Lubricant Transfer Model at the Head-Disk Interface in Magnetic Storage Considering Lubricant–Lubricant Interaction" by Y. Zhang and A.A. Polycarpou, Tribology Letters 2016, 62(3), 38. Copyright (2016) by Springer.

2010). The flow rate for lubricant pick-up is found to decrease with the bonding ratio from both simulations (Ma et al., 2007) and experiments (Waltman et al., 2010; Li et al., 2011).

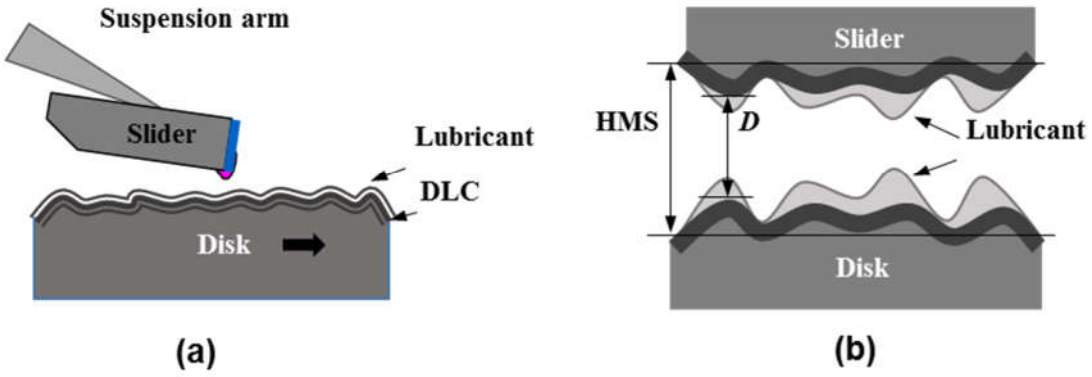

Figure 7.1 Schematics of (a) head-disk interface and (b) definition of head-media-spacing (HMS), solid distance and flying clearance. HMS is the distance between the mean planes of the surfaces of the head transducer layer and the disk magnetic media; solid distance *D* is defined as the closest distance between the two solid surfaces; clearance is the closest distance between the two surfaces considering lubricants, representing margin in flying height for the slider to fly before significant contact with the disk.

Another important characteristic of the lubricant is that it is not uniformly thick across the disk surface, as shown schematically in Figure 7.1(b). The literature reports such lubricant distribution behavior, which is also seen experimentally. For example, Pit et al. (2001) observed that the lubricant is thicker on the asperity peaks and thinner on the valleys, which is recognized as "moguls." Ma et al. (2002) found that the lubricant film under a flying head is depressed locally (reduced film thickness) due to the air pressure and air shear, to a magnitude that is balanced by the disjoining pressure. Recently, with the intensification of research in heat assisted magnetic recording (HAMR) technology, understanding of molecularly thin lubricants in disks has come to the forefront. In HAMR

the lubricant near the heated spot has lower lubricant viscosity and higher lubricant mobility. The thin film is deformed locally due to thermocapillary shear stress and evaporation, referred as depletion (Tagawa et al., 2010).

In the present work, we propose a lubricant pick-up model that accounts for lubricant-lubricant interaction, bonding ratio and lubricant roughness and investigate their combined effects.

7.2 Modeling in the literature

First of all, it is necessary to introduce and clarify some terminology of surface forces in lubricants. There are mainly three components for the surface forces in lubricants: (1) van der Waals force, which is the attractive or repulsive force between molecules or atom groups, and includes the London force (dispersive force), the Keesom force and the Debye force; (2) electrostatic "double layer" force, which arises from electrostatic or polar interactions; and (3) solvation force (structural force) arising from structuring or ordering of liquid molecules confined between two surfaces. Besides, there are a few important theories to calculate these forces, including the Lifshitz theory and its derivative work for predicting the attractive van der Waals force, the Leonard-Jones potential model for approximating the total van der Waals, and the DLVO theory for the van der Waal force and the electrostatic (double layer) force.

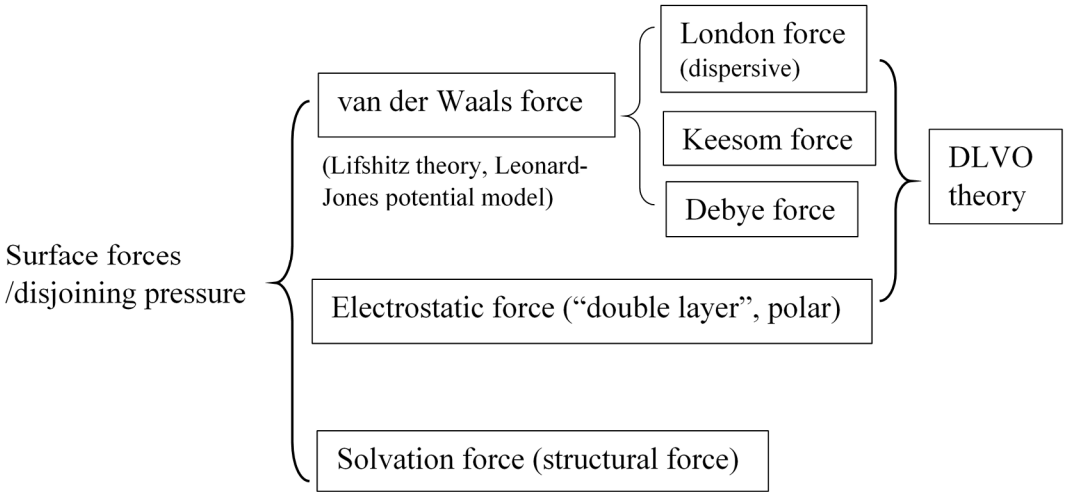

Figure 7.2 Main contributors of surface forces in lubricants and their components.

7.2.1 Van der Waals Force

If we employ the Leonard-Jones potential model (6-12 potential), strength of the attractive van der Waals force can be expressed by the 6th power term with a Hamaker constant, and the repulsive component can be expressed by the 12th power term. For a lubricated disk surface and a dry slider surface with vapor as the medium, by integrating the net potential energy over the domain and assuming the lubricant molecules can approach the solid molecules as close as possible, then the intermolecular pressure on the lubricant surface is calculated by

$$P = \frac{A_{VLS}}{6\pi h^3} - \frac{B_{VLS}}{45\pi h^9} - \left(\frac{A_{LVS}}{6\pi (D-h)^3} - \frac{B_{LVS}}{45\pi (D-h)^9} \right) \tag{7.1}$$

, where the positive terms with Hamaker constants A_{VLS} and A_{LVS} denote attractive forces from the solid disk and the slider, and negative terms with B_{VLS} and B_{LVS} represent corresponding repulsive forces from them. Note that in Eq. (7.1), if the repulsive forces

are negligible, summation the two attractive forces from the disk and the slider will decide the critical clearance for lubricant transfer, as to be discussed in the section 2.3.

Figure 7.3 depicts the intermolecular pressure variation with the solid-liquid distance *D-h*. As the solid distance *D* decreases closer to the film thickness *h*, the separation between solid and liquid surfaces drops to near zero. Then the last two terms of Eq. (7.1) become dominant and the intermolecular pressure can be written as

$$P \cong -\frac{A_{LVS}}{6\pi(D-h)^3} + \frac{B_{LVS}}{45\pi(D-h)^9}. \tag{7.2}$$

The corresponding equilibrium separation d_0 can be obtained by equating the RHS of Eq. 7.2 to zero

$$d_0 = D_0 - h = \left(\frac{6B_{LVS}}{45A_{LVS}}\right)^{1/6}. \tag{7.3}$$

Note that the equilibrium separation also refers to the equilibrium intermolecular distance (Stanley et al., 1990) or equilibrium spacing (Suh and Polycarpou, 2005) in the Lennard-Jones potential pressure model. Furthermore, by taking the derivative of Eq. 7.2, it can be found that a critical separation of $1.2d_0$ is needed to satisfy $\partial P_a / \partial h = 0$, where the attractive force reaches maximum. If the liquid-solid separation is larger than $1.2d_0$, the attractive force is dominant and the repulsive force is negligible. A corrected method to calculate d_0 can be found in (Yu and Polycarpou, 2004). Since d_0 is usually very small, most lubricant transfer models neglect the repulsive force component.

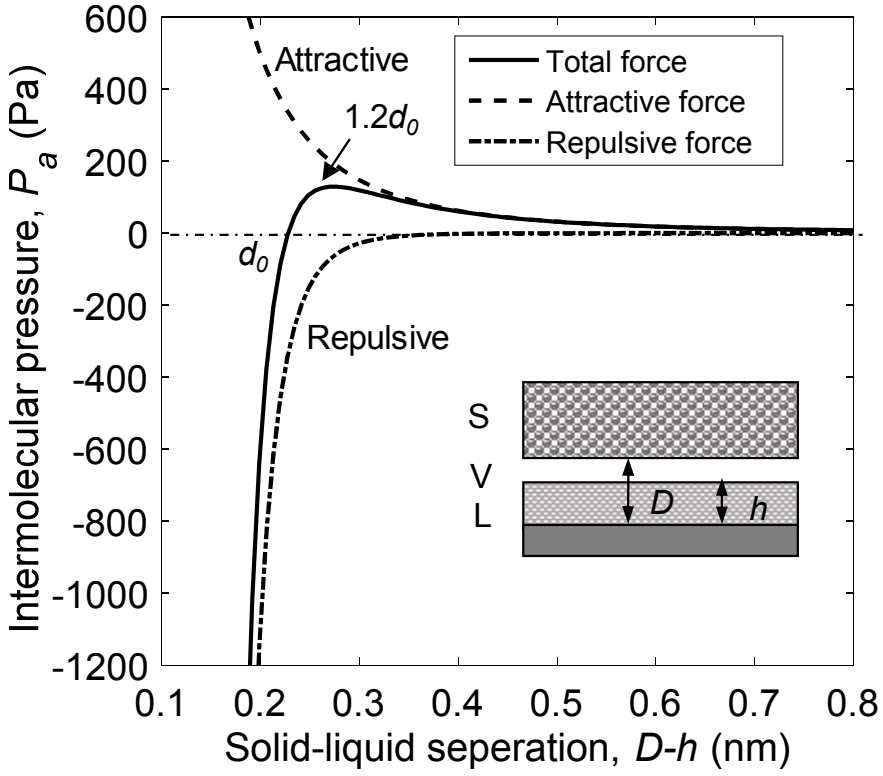

Figure 7.3 Van der Waals force per unit area with separation between the solid and liquid surfaces using Eq. 7.1 and parameters values from Table 7.2. The interaction force between the liquid and solid molecules transitions from attraction to repulsion as the separation is decreased to less than d_0.

7.2.2 Disjoining Pressure of Lubricant Film

The concept of disjoining pressure was introduced by Derjaguin in 1936, and defined as the negative derivative of the Gibbs free energy per unit area, with respect to film thickness. Considering a liquid film on a solid surface, disjoining pressure measures the net attractive interaction between the liquid and the solid surface. The concept of disjoining pressure has been widely used for determining the critical fly-height or clearance in HDIs, e.g., (Tyndall et al., 1999; Karis, 2000; Waltman, 2004; He et al., 2007). Disjoining pressure has three components: Van der Waals force, electrostatic force

and solvation force (Derjaguin and Churaev, 1974), as shown by Figure 7.1. For the lubricant on a disk surface, there is no confinement between two surfaces so no solvation force arises. Considering forces on liquid-solid and liquid-vapor interfaces, disjoining pressure is defined to be composed of dispersive pressure π_d and polar pressure π_p and expressed as:

$$\pi_{Disk} = \pi_d + \pi_p = \frac{A_{VLS}}{6\pi(h+d_0)^3} + \frac{\pi\gamma_0}{h_m}\sin\left(\frac{2\pi h}{h_m} + \alpha\right)\exp(-h/h_m) \qquad (7.4)$$

, where A_{VLS} is the Hamaker constant for vapor-liquid-solid system that measures the interaction strength between the vapor-liquid interface and the liquid-solid interface. A positive sign for A_{VLS} designates attraction while a negative sign designates repulsion. d_0 is the closest approach distance between the liquid surface and the solid substrate; γ_0 is the oscillatory amplitude of the polar component of the surface energy; h_m is the dewetting thickness; α is the phase shift. For PFPE Ztetraol lubricants on CN_X carbon coatings, the parameters used are obtained by curve fitting Eq. 7.4, and are listed in Table 7.1.

Table 7.1 Parameters for dispersive and polar components of disjoining pressure.

Parameters	A_{VLS} (J)	A_{LVS} (J)	d_0 (nm)	γ_0 (mJ/m^2)	h_m (nm)	α
Ztetraol+ CN_x	1.9×10^{-19}	$1\sim 4\times10^{-19}$	0.29	5.5	2.2	-0.4π

Note that the dispersive pressure π_d (also called London force) refers to the total Van der Waals force although it should only be the name for a major part of the Van der Waals force. The polar pressure π_p measures the strength of bonds formed between the

liquid and solid molecules, namely the electrostatic force. As an example, PFPE Zdol lubricant has hydroxyl groups at two ends and forms hydrogen bonds with carbon on the DLC coated disk surface, the strength of the bonding is expressed by the polar pressure, π_p.

Figure 7.4(a) depicts the total disjoining pressure and its Van der Waals and polar components with film thickness for Ztetraol lubricant on a CN_X solid (DLC) substrate. Figure 7.4(b) depicts the stable and unstable zones based on the disjoining pressure gradient. A lubricant coated on a solid surface always tries to form films of stable thicknesses in order to minimize its surface energy.

7.2.3 Existing Models for Lubricant Pick-up

Based on existing conventional magnetic storage technologies, higher areal density requires lower HDI spacing. An HMS of less than 5 nm is desirable for 4 TB/in^2, as predicted by Marchon et al. (2013). A simplified schematic view for the HDI is shown in Fig. 7.5(a). As the spacing decreases to a critical distance, the lubricant films on the disk and slider begin to make contact, as shown in Fig. 7.5(b).

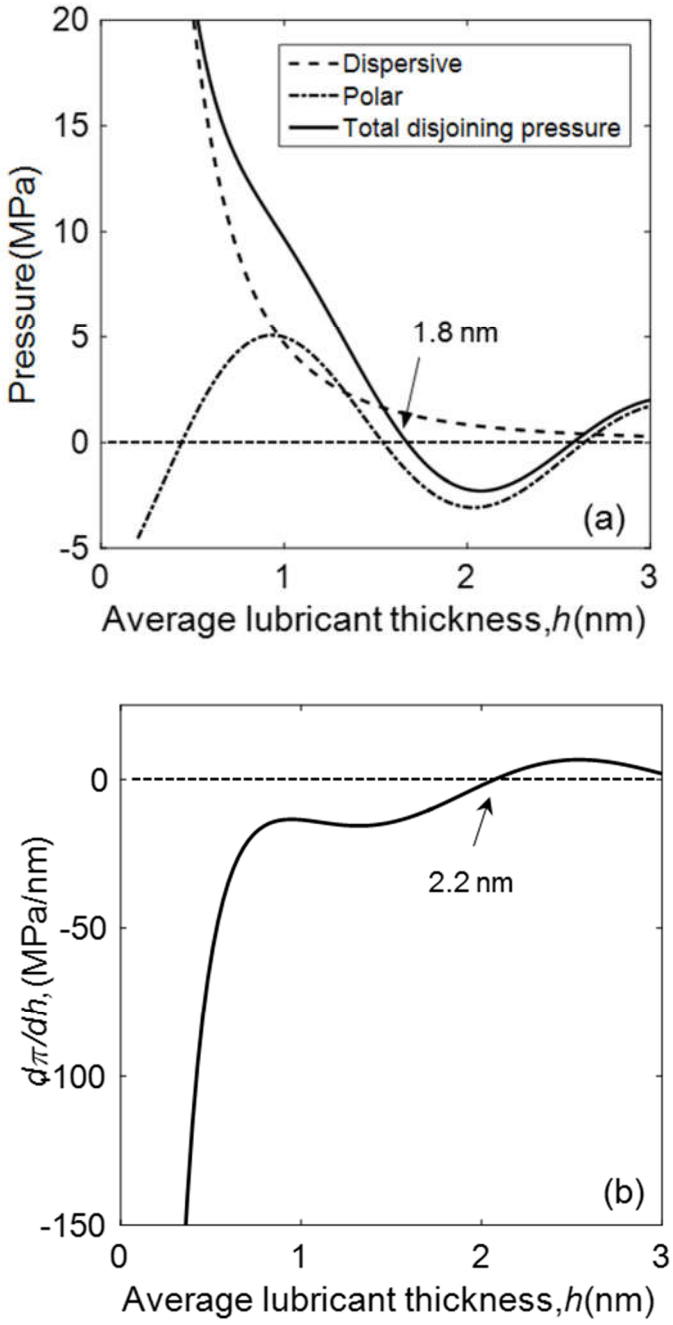

Figure 7.4 (a) Disjoining pressure π and (b) pressure gradient $d\pi/dh$ of PFPE Ztetraol with film thickness h. The critical film thickness for a total disjoining pressure $\pi = 0$ is 1.8 nm and the critical film thickness for $d\pi/dh=0$ is 2.2 nm. For h < 1.8 nm (π >0, $d\pi/dh$<0), the lubricant is stable; for 1.8 nm<h<2.2 nm (π<0, $d\pi/dh$<0), the lubricant becomes unstable; for h>2.2 nm (π<0, $d\pi/dh$>0), dewetting begins to occur (Tyndall et al., 1999).

To find out the critical clearance, it is necessary to investigate the equilibrium of the liquid-vapor interface. The lubricant is subjected to three forces, two from the solid surfaces and one from the lubricant layer. As for the lubricant on the disk surface, the attractive force from the solid disk substrate is trying to keep the lubricant attached to its surface; the attractive forces from the lubricant layer and solid surface of the slider are trying to drag the lubricant off the disk surface. Neglecting the repulsive forces, as discussed before, the total force per unit area can be expressed as

$$\sum \pi = \pi_{Disk} - \pi_{Slider} = \pi_{Disk} - \frac{A_{LVS}}{6\pi(D-h-d_0)^3} \tag{7.5}$$

, where π_{Disk} is the attraction force from the disk given by Eq. 7.4; π_{Slider} and is the attraction force from the slider.

There are two widely used models to determine the critical clearance for lubricant pick-up: (1) the first model uses the derivative of the disjoining pressure $d\Sigma\pi/dh$ and checks if it is negative or positive. If $d\Sigma\pi/dh > 0$, the lubricant is unstable and prone to dewetting (Ambekar et al., 2008; Mate, 2011). The second model proposes that the critical clearance should be decided directly from the disjoining pressure π. If $\sum\pi < 0$, there is a net attractive pressure of the lubricant toward the slider and thus possibility for the lubricant to be picked up (Waltman et al., 2010; Li et al., 2011).

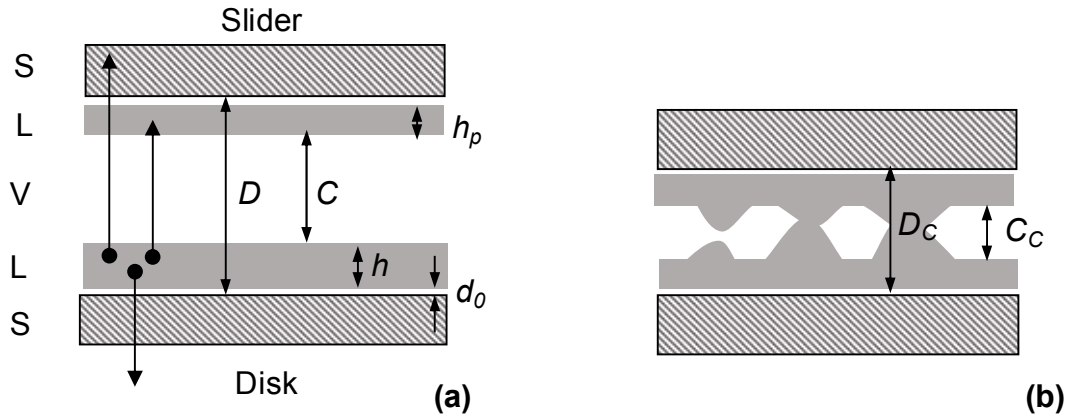

Figure 7.5 Schematics of disk and slider with lubricant layers: (a) Non-contact and (b) Contact conditions; h is the average film thickness; h_p is the thickness of the lubricant picked up by the slider, $h_p=h$ in the present work; D is the solid distance; C is the clearance, which is the margin in spacing before slider-disk contact. S, L, V represent Solid, Liquid and Vapor phases respectively. The Hamaker constant for LVL system is $3\text{x}10^{-20}$ J (Israelachvili, 1972).

7.3 Proposed Improved Lubricant Pick-up Model

Israelachvili proposed that the Hamaker constant for liquid-vapor-liquid system is usually 3×10^{-20} J (Israelachvili, 1972). It was found that the lubricant accumulated on the slider is approximately as thick as the lubricant on the disk, i.e., pick-up lubricant thickness $h_p=h$ (Gao et al., 1999). This implies that the lubricant-vapor-lubricant system may contribute to the total force or disjoining pressure, which however has been neglected by the two models described in Sec. 7.3. This interaction between two lubricant layers is added to Eq. 7.5 and yields the improved lubricant pick-up model:

$$\begin{aligned}\sum \pi &= \pi_{Disk} - \pi_{Slider} - \pi_{Lube} \\ &= \pi_{Disk} - \frac{A_{LVS}}{6\pi(D-h-d_0)^3} - \left[\frac{A_{LVL}}{6\pi(D-2h-2d_0)^3} - \frac{A_{LVL}}{6\pi(D-h-2d_0)^3}\right]\end{aligned} \tag{7.6}$$

, where π_{Lube} is the net force per unit area on the disk lubricant surface that is the attraction force from the lubricant layer on the slider and its mathematical derivation can be seen in the Appendix C.1; π_{Disk} is given by Eq. 7.4.

After accounting for this lubricant-lubricant interaction, present work believes at a certain clearance, the lubricant surface on the disk loses its stability as the total force becomes negative ($\sum\pi<0$), and vice versa. The lubricant on the slider experiences the same amount of force. The two lubricant layers break the equilibrium and begin to contact each other, forming meniscus bridges between them, as shown in the schematic of Fig. 7.5(b).

Figure 7.6 shows comparisons between the existing and the proposed improved models. The critical solid distance is located by crossing points of the intermolecular force $\sum\pi$ (per unit area) or its derivative $d\sum\pi/dh$ with the zero value, shown by Figs. 7.6(a) and 7.6(b). Please note that the proposed model does not use the derivative $d\sum\pi/dh=0$ to determine the critical distance, but instead uses $\Sigma\pi=0$ after adding new term π_{lube} to $\Sigma\pi$. Thus, it is not necessary to list its derivative $d\sum\pi/dh$. After considering the lubricant interaction, the proposed model predicts the maximum critical solid distance because it introduces more attractive force applied on the disk lubricant from the slider after considering the lubricant-lubricant interaction. The conventional #2 model predicts the minimum and the model utilizing $d\sum\pi/dh$, corresponding to the conventional #1 model introduced in section 2.3, is in the between.

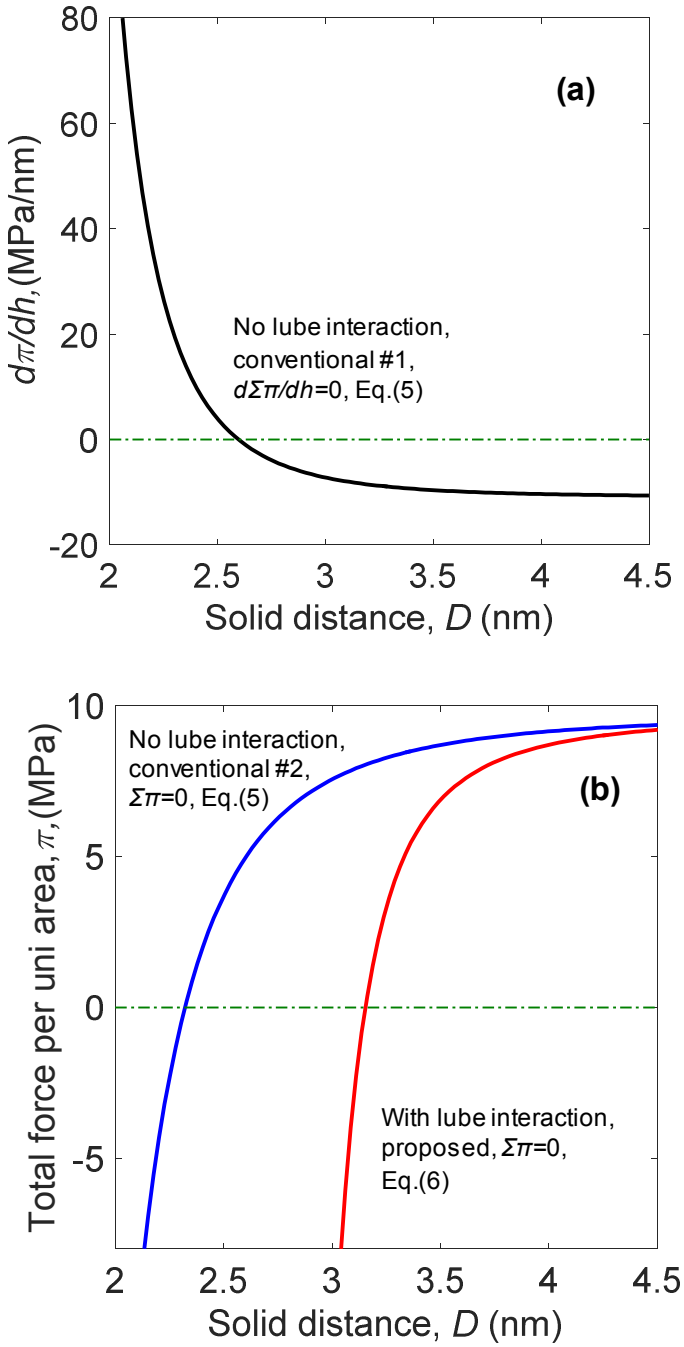

Figure 7.6 (a) Conventional model #1, determination of the critical solid distance by setting $d\Sigma\pi/dh = 0$, without lube-lube interaction; (b) determination of the critical solid distance without lube-lube interaction by the conventional model #1 and with lube-lube interaction proposed by present study, both $\Sigma\pi$=0, while conventional model #2 uses Eq. (7.5) and the proposed model uses Eq. (7.6) to calculate $\Sigma\pi$,. With film thickness h= 1nm, lubricant roughness σ=0, bonding ratio=0, other parameter values are from Table 7.1.

7.4 Results and Discussion

7.4.1 Comparison with Molecular Dynamics Simulations

The MD simulation results by Wong et al. (2011) only considers Van der Waals forces, with no contribution from the polar component. The equilibrium separation is calculated by Eq. 7.3 and the picked-up lubricant thickness (designated as h_P) is assumed as half of that on the disk. Table 7.2 lists the parameters cited from publications studying HDI using MD simulations.

Table 7.2 Parameters used in Molecular Dynamics simulations.

Parameters	A_{VLS} (J)	B_{VLS} (J-m^6)	A_{LVS} (J)	B_{LVS} (J-m^6)	A_{LVL} (J)	h_P (nm)	d_0 (nm)
Values	1.0×10^{-19}	1.0×10^{-76}	7.5×10^{-20}	7.9×10^{-77}	3.0×10^{-20}	*h/2*	0.23

Figure 7.7 depicts the critical solid distance for lubricant transfer using the existing and proposed models shown in Figure 7.6 and also compared with MD simulation results. Note that the MD simulation only considers the Van der Waals force (or the dispersive pressure) and so does the three models for this comparison, i.e., the polar component π_p of π_{Disk} is neglected. The conventional model #1 marked as $d\sum\pi/dh=0$ was used in the literature (Wong et al., 2011) to compare with the MD simulations. The conventional model #2 labeled as $\sum\pi=0$ (without lube int.) is commonly seen in the literature (Waltman et al., 2010; Li et al., 2011). The present work proposes the model designated as $\sum\pi=0$(with lube int.). Compared with the other two models, the present model shows

better agreement with the MD model at lubricant thickness less than 1.4 nm, which is desirable in the hard disk drive industry. Clearly, even though the effect of the lubricant interaction is small, compared to solid interactions, its effect cannot be neglected.

7.4.2 Effect of Lubricant Roughness

The lubricant roughness adds to the critical clearance where lubricant pick-up happens. It is reported that the contribution from the lubricant and lubricant roughness takes up one third of a 10 nm spacing budget (Mate et al., 2011). To account for the effects of lubricant roughness, the present work first calculates the critical distance for the case of smooth lubricant and then adds to the solution 6σ, i.e., $D_c(\sigma)=D_c(0)+6\sigma$, where σ is the lubricant RMS roughness. The lubricant roughness here means the roughness of the lubricant surface with respect to the mean plane of the solid surface as the reference (Pit et al., 2001). Measurements of the lubricant roughness can be achieved using Optical Surface Analyzer (Pit et al., 2001) or X-ray reflectivity (Mate et al., 2001). As the lubricant surface can be taken as within mean plane±3σ, then 6σ is used to account for maximum contribution from both lubricant roughness of the disk and the slider if assuming the lubricant roughness on the slider is the same as that on the disk.

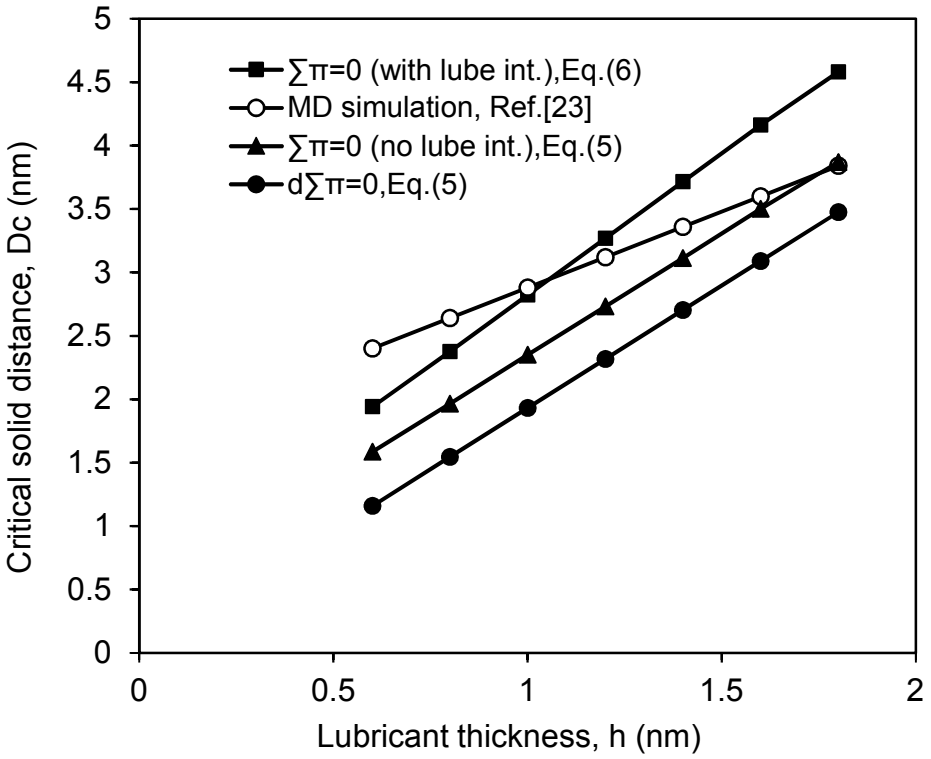

Figure 7.7 Critical solid distance D_C for lubricant transfer predicted by different models and MD simulations. The present model considers lube-lube interaction marked as $\sum\pi$=0(with lube int.). Bonding ratio and lubricant roughness are neglected.

Figure 7.8 shows the critical solid distance at two different values of the Hamaker constant $A_{LVS,}$ varying with lubricant roughness and average thickness. Note that A_{LVS} denotes strength of attractive force on the disk lubricant layer from the slider solid surface. Comparing the A_{VLS} values of 1×10^{-19} J and 4×10^{-19} J, the difference between the two cases is very small. Both of them predict a minimum of about 2.5 nm and a maximum of about 7nm. This implies that the lube-slider interaction is playing a lesser role than the lube-lube interaction in determining the critical conditions for the lubricant transfer. Examining Figure 7.7, at small film thickness values (h<1 nm), the critical solid distance is increased

by less than 1 nm as the roughness increases from 0 to 0.4 nm; but for a thicker lubricant film, this increment adds up to 2 nm or more. This implies when the lubricant goes thicker the lube roughness play much stronger role in determining the critical solid distance. Therefore, lubricant of sub-monolayer thickness (<1.8 nm) is not enough to avoid occurrence of pick-up. The criterion should be reduced to around 1nm after consideration of lubricant roughness.

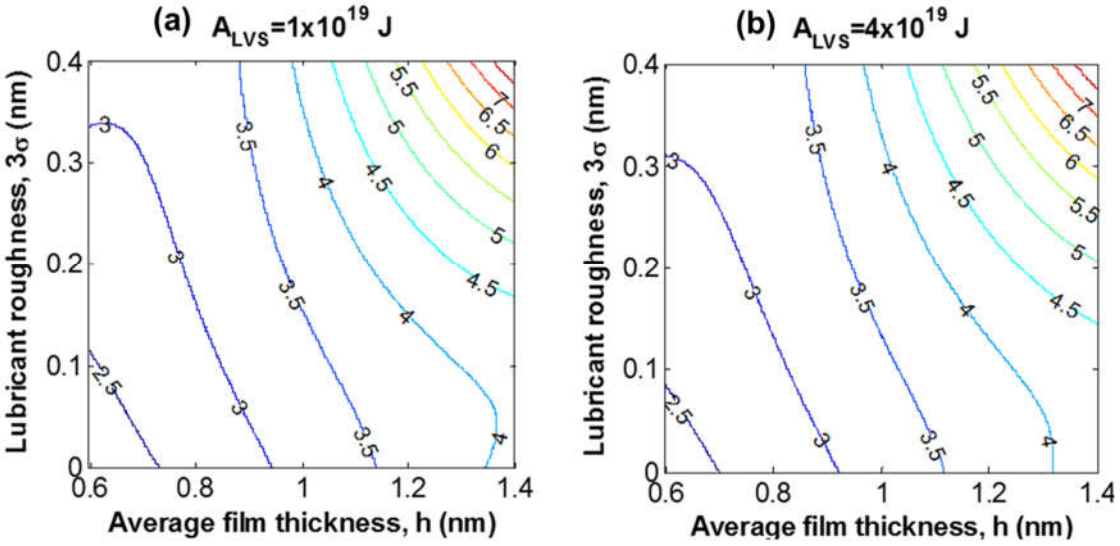

Figure 7.8 Critical solid distances D_C (nm) with film thickness and lubricant roughness 3σ at Hamaker constants A_{VLS} for Liquid-Vapor-Solid systems of (a) 1×10^{-19} J and (b) 4×10^{-19} J. The A_{VLS} constant has a small effect in decreasing the critical solid-distance. The total lubricant thickness at the present simulations is up to the critical thickness for instability (1.8 nm). Bonding ratio is 0 and the other parameters are given in Table 7.1.

7.4.3 Effect of Lubricant Bonding Ratio (BR)

Another important factor for lubricant transfer is lubricant bonding ratio. Lubricant transfer is reported to decrease almost linearly with the bonding ratio (Li et al., 2011), for reasons that are not entirely clear. The work above has not taken into account bonding

ratio of the lubricant, i.e., the bonding ratio was taken as zero (namely that lubricant is all mobile) in the previous analysis, which is not realistic in practice. A bonding ratio of one is also not realistic, as it implies that all the lubricant is fully bonded to the surface and not allowed to move. Considering a lubricant where the BR varies from 0 to 1, the last term on the RHS of Eq. 7.6 can be modified as follows:

$$\pi_{Lube} = \frac{A_{LVL}}{6\pi}\left\{\frac{1}{\left[D-h\left(1-BR\right)-h-2d_0\right]^3}-\frac{1}{\left(D-h-2d_0\right)^3}\right\} \tag{7.7}$$

Based on Eq. 7.7, the present work captures the case of any BR value and also proposes a linear relationship between the critical solid distance and the bonding ratio using the two extreme solutions at BR=0 and 1. The detailed derivation is given in the Appendix C.2.

$$\mathrm{D}_C\left(BR\right) = \left(h+d_0\right)\left[\left(\sqrt[3]{\frac{A_{LVS}}{A_{VLS}}}-\sqrt[3]{\frac{A_{LVL}}{A_{VLS}}}-1\right)BR+2+\sqrt[3]{\frac{A_{LVL}}{A_{VLS}}}\right] \tag{7.8}$$

Correspondingly the critical clearance is obtained from $C=D-2h-2d_0$.

$$C_C\left(BR\right) = \left(h+d_0\right)\left[\left(\sqrt[3]{\frac{A_{LVS}}{A_{VLS}}}-\sqrt[3]{\frac{A_{LVL}}{A_{VLS}}}-1\right)BR+\sqrt[3]{\frac{A_{LVL}}{A_{VLS}}}\right]+d_0$$

$$C_C\left(BR\right) = \left(h+d_0\right)\left[\left(\sqrt[3]{\frac{A_{LVS}}{A_{VLS}}}-\sqrt[3]{\frac{A_{LVL}}{A_{VLS}}}-1\right)BR+\sqrt[3]{\frac{A_{LVL}}{A_{VLS}}}\right] \tag{7.9}$$

Figure 7.8(a) shows how the total interfacial force calculated from Eq. 7.6 and Eq. 7.7 varies with the bonding ratio: The critical solid distance decreases with the bonding ratio, and this is because when the bonding ratio is small, there is stronger interaction between the lubricant on the slider and the disk. When the bonding ratio is equal to 1, there

is no mobile fraction for the lubricant and thus no lubricant pick-up happens, leading to a small critical solid distance. Figure 7.8(b) shows the critical solid distance and clearance calculated by Eq. 7.8 and Eq. 7.9. As the bonding ratio increases to 1, the critical clearance decreases to almost 0, implying direct contact between two solid dry surfaces.

From Figure 7.8, it seems that a larger bonding ratio is desirable to shorten the spacing between the disk and the slider. However, it is meaningless to have a lubricant with bonding ratio of 1 because the role of the lubricant is to decrease friction when contact happens and the friction coefficient increases with increasing bonding ratio. Note that in practice a BR of around 0.5 is typically used.

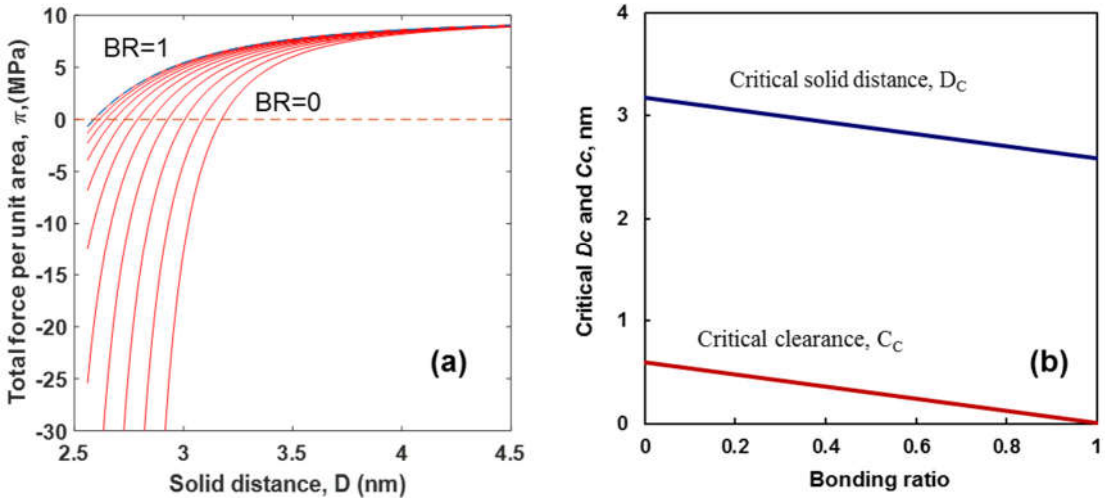

Figure 7.9 (a) Total interfacial force for different levels of BR, (b) Critical solid distance determined from Eq. 7.8 and proposed linear model from Eq. 7.9 for critical clearance at different BR values, using parameters from Table 7.1 and lubricant thickness of 1 nm. Lubricant roughness is 0.

7.5 Summary of Chapter 7

The present chapter proposes an improved lubricant pick-up model accounting for (a) the interaction between lubricants on the slider and the disk, (b) lubricant bonding ratio, and (c) lubricant roughness. Compared with two different currently used lubricant pick-up models, the proposed model predicts a larger critical solid distance and thus less clearance for lubricant pick-up. In other words, the present study shows that the critical clearance accounting for lube-lube interaction is smaller than what is predicted by the two conventional models that ignore lube-lube interaction. The present work also found that the lube-slider interaction is playing a lesser role than the lube-lube interaction in determining the critical conditions for the lubricant transfer. Finally, the present study proposed a linear relationship between the clearance and the lubricant bonding ratio. This model can be used for the design of head-disk interface systems, as far as the molecularly thin lubricant properties are concerned.

8 SUMMARY OF THESIS RESEARCH AND RECOMMENDATION FOR FUTURE WORK

8.1 Summary of the thesis

As outcome of a research project sponsored by the magnetic storage hard disk industry, present work initially aims to investigate tribology issues at the head-disk interface. However, the hard disk drive is a very typical Micro-electro-mechanical system (MEMS) which involves applications of thin film deposition, material science, chemistry and mechanics. These elements are included in an interdisciplinary subject, tribology, which are critical for durability of hard disk drives. In the field of IT (information technology) hardware, placing higher density of units in a device of smaller volume is one of the primary goal to pursue. A famous indicator should be the Moore's law observing the number of transistors in an integrated circuit doubles every two years. Similar trend has also been seen in the HDD industry. The areal density of a HDD enlarged 100 times in 10 years, from ~10 Gb/in^2 in 2000 to ~1 Tb/in^2 in 2010. As stated in the Chapter 1, one sacrifice for the increased areal density is shrinkage of the head-media spacing (HMS), which brings the head closer to the disk. Current technology for PMR (Perpendicular Magnetic Recording) hard disks has achieved an areal density of more than 1Tb/in^2 which demands a HMS of less than 10nm and a clearance of near 1 nm. Such a small clearance leads to higher probability of direct contact between the slider and the disk, which gives rise to more risk of media demagnetization due to contact induced plastic deformation, frictional heating and grain tilting. On the other hand, such direct contact also causes

mechanical failure of the writing/reading head. For the sake of protection, above the recording layer there is deposited with amorphous diamond-like carbon (DLC) coatings with thickness of 2~4 nm to prevent mechanical damage. Besides, a mono-layer of PFPE lubricant with thickness of 1~2 nm is applied on the disk. Present work dedicates to investigating tribological properties of the three: the recording layer, the DLC coating and the lubricant. Contributions and new findings of the investigation can be summarized as below:

(1) Characterization of nanomechanical properties of ultra-thin films is challenging. The conventional Oliver-Phaar method may not be applicable because of substrate effects. Thus, many previous work dedicates to remove substrate effects using different means. One of the most used means is to combine nanoindentation technique with Finite Element Analysis, i.e., FEA-nanoindentation method. But for thin films for the recording layer dealt with by the present study, the thickness is only 14 nm and it requires more an accurate Finite Element Model for the probe especially for the top contacting at shallow depths. The research in Chapter 2 first uses SEM to zoom-in the tip top and it is found the tip top is truncated or flattened due to mechanical wear. Present study performs an elastic punch on a standard sample (Fused Quartz) to quantitatively characterize the flatness which is used in the finite element model. Then the proposed blunt tip model is validated with experiments using larger force on Fused Quartz sample. Then the model is applied to measure the nanomechanical properties of a 90 nm thick metal alloy layer and a 14 nm thick magnetic layer sandwiched between a carbon overcoat and a metal alloy.

(2) In the Chapter 3, the thesis proposed another means to directly characterize nanomechanical properties by developing a highly sensitive force-displacement transducer capable of performing ultra-shallow nanoindentation. The transducer utilizes electrostatic actuation and capacitive sensing combined with microelectromechanical systems fabrication technologies. Air indentation experiments report a root-mean-square (RMS) force resolution of 1.8 nN and RMS displacement resolution of 0.019 nm. Nanoindentation experiments on a standard Fused Quartz sample report a practical RMS force resolution of 5 nN and RMS displacement resolution of 0.05 nm at sub-10 nm indentation depths, indicating that the system has a very low system noise for indentation and adhesion experiments. The high sensitivity and low noise transducer is capable of obtaining high-resolution nanoindentation data at sub-5 nm contact depths. In addition, the sensitive force transducer is also used to perform adhesion measurements, clearly capturing the pull-on and pull-off forces during approach and separation of two contacting surfaces. This feature can also be useful for adhesion tests.

(3) With the highly sensitive transducer introduced above, Chapter 4 performs shallow nanoindentation on three HDD samples with different sputtering voltages for the 14-nm recording layer. The present thesis demonstrates capability of directly characterizing nanomechanical properties of the three nanocompsite films. And also, the Chapter 4 uses a sharp cono-spherical probe installed on a regular 2-D transducer to perform nanoscratch experiments. The two types of experiments revealed dependence of nanomechanical and nanotribological properties on the bias voltage.

(4) From the Chapter 2 to Chapter 4, conventional PMR (Perpendicular Magnetic Recording) hard disk drives are investigated. As the HMS has been reduced to a limit for the PMR technology, the HAMR (Heat Assisted Magnetic Recording) technology has been taken as one of the two most promising technologies for the next-generation hard disks with higher areal densities, besides BPM (Bit Patterned Media). The work in the Chapter 5 focus on tribological investigation of the DLC coating at high-temperature conditions through shallow tribology experiments on an ultra-thin (3 nm) hydrogenated amorphous (a-C:H) coating at elevated temperatures up to 300 °C. The nanoscratch experiments (single scratch) provide in-situ measurement of the friction coefficient and material deformation of the carbon film. The nanowear experiments (repeated scratches over an area) investigate the extent of wear under multiple scratches. The two groups of experiments reveal the temperature dependence of the tribological behavior of the coating. Raman analysis was performed to compare the chemical structure of the carbon film before and after heating. The spectrum reveals both the hydrogen and sp3 content of the carbon film decrease after the high-temperature experiments, which contribute to deterioration of the wear resistance of the coating.

(5) Previous chapters dedicates to tribological studies of solid thin films and coatings of the magnetic storage device. The molecularly thin lubricant addressed by Chapter 6 is also important in protecting both the head and the disk from mechanical damage induced by contact of the two. Direct contact is more likely to occur at smaller HMS (Head-media spacing) as is always desired by the industry for higher areal density. Solid contact mechanics on the HDI (head-disk interface) has been well addressed through

extensive experiments and modeling. However, the contact happening in the lubricant remains unknown or not clearly investigated. Considering the important role of the lubricant, it is quite necessary to investigate the forces due to contact in the lubricant so as to understand the protection mechanism of the lubricant. Chapter 6 develops a mechanics model to account for nano phenomenon including slippage, nonlinear viscosity and bonded fraction, potentially bridging the hydrodynamic lubrication and solid contact regimes at the nanoscale.

(6) Chapter 7 is an extended work of Chapter 6. In the HDD industry, the critical HMS is determined by the onset of lubricant transfer from the disk to the head as lubricant loss is taken as the first step of weakening of protection layers. Interactions among molecularly thin lubricant-solid and lubricant-vapor interfaces become increasingly strong when the slider approaches closer to the disk (or media) surface, which is desirable for higher storage areal densities. Lubricant transfers from the disk to the slider as the head-media spacing decreases below a critical value, leading to loss of protection for the solid thin films. Chapter 7 proposed a new criteria for lubricant pick-up to occur by considering interactions between the lubricant films, in addition to lubricant-solid interaction. The effect of lubricant roughness is also included in the proposed model, which is then used to predict critical solid distances as a function of lubricant roughness and average lubricant thickness. It is found that the interaction force between the slider solid and the disk lubricant plays a weaker role than that between the lubricant on the slider and the lubricant on the disk in determining the critical solid distance. The physics for the dependence of the critical clearance on the bonding ratio is explained and a linear model is developed.

8.2 Recommendations for future work

The future work can focus on the next-generation technologies for HDDs and extension of nanotribology to other engineering applications. As stated before, there are two major solutions to overcome the bottleneck of areal density: BPM and HAMR.

(1) The BPM focus on construction of featured media grains in order to decrease the SNR (Signal Noise Ratio). The grains of the recording layer are nanopillars deliberately made by fabrication. However, the recording layer's tribological properties will be highly dependent on designs of the pattern, such as spacing between two adjacent pillars and geometrical parameters of the pillars. Therefore, future work can be conducted to correlate the nanotribological properties of the media layer with the bit pattern design, referring to the research done in Chapter 4.

(2) Present thesis only includes one chapter of work regarding high-temperature tribological studies of the carbon film. With the advanced high-temperature nanomechanical stage (Hysitron Xsol), much more exciting work can be done in the future. Tribological properties of the amorphous hydrogenated carbon film depend on many factors, including chemical compositions of hydrogen, sp^2 and sp^3, presence or absence of oxygen, environment temperature and humidity. Future work can look into effects of these factors on nanotribological properties of ultra-thin carbon films systematically as there has been insufficient work done in the literature. Research in tribological properties of carbon materials at high temperature can also help the work to extend to broader applications as the carbon coating has been widely used in many MEMS devices.

(3) Another interesting work can be done in the future is also about high-temperature tribology but more relevant to modelling. In the field of contact mechanics, much work has been done in building models to predict contact forces between two rough surfaces. However, contact mechanics at high temperature is still a new area. We can find out temperature dependence of mechanical properties such as softening of materials through nanoindentation experiments. And also we can perform high-temperature adhesion experiments to find out temperature dependence of surface energy. With these temperature dependence relations, we are able to extend the current contact mechanics from room temperature to high temperature. Lastly, we can perform high-temperature nanoscratch experiments to obtain experimental data to validate the high-temperature modelling.

BIBLIOGRAPHY

Acharya, B.R., Zhou, J.N., Zheng, M., Choe, G., Abarra, E.N., Johnson, K.E., 2004. Anti-parallel coupled soft under layers for high-density perpendicular recording. IEEE Trans. Magn. 40, 2383–2385. doi:10.1109/TMAG.2004.832165

Al-Azizi, A.A., Eryilmaz, O., Erdemir, A., Kim, S.H., 2015. Surface structure of hydrogenated diamond-like carbon: Origin of run-in behavior prior to superlubricious interfacial shear. Langmuir 31, 1711–1721. doi:10.1021/la504612c

Albrecht, T.R., Arora, H., Ayanoor-Vitikkate, V., Beaujour, J.M., Bedau, D., Berman, D., Bogdanov, A.L., Chapuis, Y.A., Cushen, J., Dobisz, E.E., Doerk, G., Gao, H., Grobis, M., Gurney, B., Hanson, W., Hellwig, O., Hirano, T., Jubert, P.O., Kercher, D., Lille, J., Liu, Z., Mate, C.M., Obukhov, Y., Patel, K.C., Rubin, K., Ruiz, R., Schabes, M., Wan, L., Weller, D., Wu, T.W., Yang, E., 2015. Bit-patterned magnetic recording: Theory, media fabrication, and recording performance. IEEE Trans. Magn. 51. doi:10.1109/TMAG.2015.2397880

Anders, S., Diaz, J., Ager III, J.W., Lo, R.Y., Bogy, D.B., 1997. Thermal Stability of Amorphous Hard Carbon Films Produced by Cathodic Arc Deposition. Appl. Phys. Lett. 7, 3367–3369. doi:10.1063/1.120339

Anders, S., Ager III, J.W., Pharr, G.M., Tsui, T.Y., G. Brown, I., 1997. Heat treatment of cathodic arc deposited amorphous hard carbon films. Thin Solid Films 308–309, 186–190. doi:10.1016/S0040-6090(97)00385-4

Antunes, J.M., Menezes, L.F., Fernandes, J. V., 2007. Influence of Vickers tip imperfection on depth sensing indentation tests. Int. J. Solids Struct. 44, 2732–2747. doi:10.1016/j.ijsolstr.2006.08.017

Archard, J.F., 1953. Contact and rubbing of flat surfaces. J. Appl. Phys. 24, 981–988. doi:10.1063/1.1721448

Asif, S.A.S., Wahl, K.J., Colton, R.J., 1999. Nanoindentation and contact stiffness measurement using force modulation with a capacitive load-displacement transducer. Rev. Sci. Instrum. 70, 2408. doi:10.1063/1.1149769

Asif, S. a S., Wahl, K.J., Colton, R.J., 1999. Nanoindentation and contact stiffness measurement using force modulation with a capacitive load-displacement transducer. Rev. Sci. Instrum. 70, 2408. doi:10.1063/1.1149769

Bewilogua, K., Hofmann, D., 2014. History of diamond-like carbon films - From first experiments to worldwide applications. Surf. Coatings Technol. 242, 214–225. doi:10.1016/j.surfcoat.2014.01.031

Bhatia, C.S., Anders, S., Brown, I.G., Bobb, K., Hsiao, R., Bogy, D.B., 1998. Ultra-Thin Overcoats for the Head / Disk Interface Tribology. J. Tribol. 120, 795–799.

Bhattacharya, A.K., Nix, W.D., 1988. Finite element simulation of indentation experiments. Int. J. Solids Struct. 24, 881–891. doi:10.1016/0020-7683(88)90039-X

Bhushan, B., Li, X., 2003. Nanomechanical characterisation of solid surfaces and thin films. Int. Mater. Rev. 48, 125–164. doi:10.1179/095066003225010227

Bowden, F.P., Tabor, D., 2002. Friction, lubrication and wear: a survey of work during the last decade. Br. J. Appl. Phys. 17, 1521–1544. doi:10.1088/0508-3443/17/12/301

Brizmer, V., Kligerman, Y., Etsion, I., 2007. Elastic – plastic spherical contact under combined normal and tangential loading in full stick. Tribol. Lett. 25, 61–70. doi:10.1007/s11249-006-9156-y

Cahoon, J.R., Broughton, W.H., Kutzak, A.R., 1971. The determination of yield strength from hardness measurements. Metall. Trans. 2, 1979–1983. doi:10.1007/BF02913433

Chang, S.Y., Lee, Y.S., Hsiao, H.L., Chang, T.-K., 2006. Mechanical properties and deformation behavior of amorphous nickel-phosphorous films measured by nanoindentation test. Metall. Mater. Trans. A 37, 2939–2945. doi:10.1007/s11661-006-0175-y

Chappell, P.H., Elliott, J. a, 2003. Contact force sensor for artificial hands with a digital interface for a controller. Meas. Sci. Technol. 14, 1275–1279. doi:10.1088/0957-0233/14/8/312

Charitidis, C.A., 2010. Nanomechanical and nanotribological properties of carbon-based thin films: A review. Int. J. Refract. Met. Hard Mater. 28, 51–70. doi:10.1016/j.ijrmhm.2009.08.003

Chen, F., Chang, R., 2007. Study of the effect of imperfect tips on nanoindentation by FEM. J. Mech. Sci. Technol. 21, 1471–1476.

Chen, X., Vlassak, J.J., 2001. Numerical study on the measurement of thin film mechanical properties by means of nanoindentation. J. Mater. Res. 16, 2974–2982. doi:10.1557/JMR.2001.0408

Cheng, Y.T., Cheng, C.M., 1998. Scaling approach to conical indentation in elastic-plastic solids with work hardening. J. Appl. Phys. 84, 1284–1291. doi:Doi 10.1063/1.368196

Chowdhury, S., Polychronopoulou, K., Cloud, A., Abelson, J.R., Polycarpou, A.A., 2015. Nanomechanical and nanotribological behaviors of hafnium boride thin films. Thin Solid Films 595, 84–91. doi:10.1016/j.tsf.2015.10.030

Christopher, I., Dennison, R., Ca, V., Wild, P.M., Ca, V., Wilson, D.R., Ca, V., Cripton, P.A., 2012. (12) Ulllted States Patent 2. doi:10.1197/jamia.M1139.Adar

Cui, L., Lu, Z., Wang, L., 2014. Probing the low-friction mechanism of diamond-like carbon by varying of sliding velocity and vacuum pressure. Carbon 66, 259–266. doi:10.1016/j.carbon.2013.08.065

Dahl, J.B., Bogy, D.B., 2013. Simulation of lubricant recovery after heat-assisted magnetic recording writing. Tribol. Lett. 52, 163–174. doi:10.1007/s11249-013-0203-1

De Hosson, J.T.M., Soer, W.A., Minor, A.M., Shan, Z., Stach, E.A., Asif, S.A.S., Warren, O.L., 2006. In situ TEM nanoindentation and dislocation-grain boundary interactions: a tribute to David Brandon. J. Mater. Sci. 41, 7704–7719. doi:10.1007/s10853-006-0472-2

Doerner, M.F., White, R.L., 2017. Materials Issues in Magnetic-Disk Performance.

Donnet, C., Erdemir, A., 2008. Diamond-like carbon films: A historical overview, Tribology of Diamond-Like Carbon Films: Fundamentals and Applications. doi:10.1007/978-0-387-49891-1

Doyle, I.M.P., Dale, G., Choi, H., City, B., Schutt, C., Staples, P.E., 2012. (12) UnIted States Patent 2, 293–298. doi:10.1126/science.Liquids

Engineering, C., 1998. .. .. :5 10 368–372.

Erdemir, A., 2001. The role of hydrogen in tribological properties of diamond-like carbon films. Surf. Coatings Technol. 146–147, 292–297. doi:10.1016/S0257-8972(01)01417-7

Erdemir, A., Donnet, C., 2006. Tribology of diamond-like carbon films: recent progress and future prospects. J. Phys. D. Appl. Phys. 39, R311--R327. doi:10.1088/0022-3727/39/18/R01

Eryilmaz, O.L., Erdemir, A., 2007. Investigation of initial and steady-state sliding behavior of a nearly frictionless carbon film by imaging 2- and 3-D TOF-SIMS. Tribol. Lett. 28, 241–249. doi:10.1007/s11249-007-9268-z

Fässler, M., 2010. Force Sensing Technologies. Stud. Mechatronics , ETH 1–49.

Ferrari, A.C., Robertson, J., 2001. Resonant Raman spectroscopy of disordered, amorphous, and diamondlike carbon. Phys. Rev. B 64, 75414. doi:10.1103/PhysRevB.64.075414

Ferrari, A.C., 2004. Diamond-like carbon for magnetic storage disks. Surf. Coatings Technol. 180–181, 190–206. doi:10.1016/j.surfcoat.2003.10.146

Fischer-Cripps, A.C., 2006. Critical review of analysis and interpretation of nanoindentation test data. Surf. Coatings Technol. 200, 4153–4165. doi:10.1016/j.surfcoat.2005.03.018

Fleming, A.J., 2013. A review of nanometer resolution position sensors: Operation and performance. Sensors Actuators, A Phys. 190, 106–126. doi:10.1016/j.sna.2012.10.016

Gadelrab, K.R., Bonilla, F.A., Chiesa, M., 2012. Densification modeling of fused silica under nanoindentation. J. Non. Cryst. Solids 358, 392–398. doi:10.1016/j.jnoncrysol.2011.10.011

Gao, G.T., Mikulski, P.T., Harrison, J. a, 2002. Molecular-Scale Trobology of Amorphous Carbon Coatings: Effects of Film Thickness, Adhesion, and Long-Range Interactions. Jacs 124, 7202–7209. doi:10.1021/ja0178618

Gao, S., Li, Z., Herrmann, K., 2010. Development of a micro-miniature nanoindentation instrument with a force resolution of 1 nN. Optoelectron. Instrum. Data Process. 46, 347–352. doi:10.3103/S8756699010040072

Gong, Z., Shi, J., Zhang, B., Zhang, J., 2017. Graphene Nano Scrolls Responding to Superlow Friction of Amorphous Carbon. Carbon N. Y. 116, 310–317. doi:10.1016/j.carbon.2017.01.106

Grannen, K.J., Thangaraj, R., Rauch, G.C., 2000. Ion beam deposition of carbon overcoats for magnetic thin film media. IEEE Trans. Magn. 36, 120–124. doi:10.1109/20.824436

Grill, a, Patel, V., Meyerson, B., 1990. Optical and tribological properties of heat-treated diamond-like carbon. J. Mater. … 10598, 2531–2537. doi:10.1557/JMR.1990.2531

Grill, A., 1999. Diamond-like carbon: state of the art. Diam. Relat. Mater. 8, 428–434. doi:10.1016/S0925-9635(98)00262-3

Gui, J., 2003. Tribology challenges for head-disk interface toward 1 Tb/in2. IEEE Trans. Magn. 39, 716–721. doi:10.1109/TMAG.2003.808999

Han, S.M., Guyer, E.P., Nix, W.D., 2011. Extracting thin film hardness of extremely compliant films on stiff substrates. Thin Solid Films 519, 3221–3224. doi:10.1016/j.tsf.2010.12.167

Han, S.M., Saha, R., Nix, W.D., 2006. Determining hardness of thin films in elastically mismatched film-on-substrate systems using nanoindentation. Acta Mater. 54, 1571–1581. doi:10.1016/j.actamat.2005.11.026

Hay, J.C., Bolshakov, A., Pharr, G.M., 1999. A critical examination of the fundamental relations used in the analysis of nanoindentation data. J. Mater. Res. 14, 2296–2305. doi:10.1557/JMR.1999.0306

Herrmann, K., Hasche, K., Pohlenz, F., Seemann, R., 2001. Characterisation of the geometry of indenters used for the micro- and nanoindentation method. Measurement 29, 201–207. doi:10.1016/S0263-2241(00)00039-7

Herrmann, K., Jennett, N.M., Wegener, W., Meneve, J., Hasche, K., Seemann, R., 2000. Progress in determination of the area function of indenters used for nanoindentation. Thin Solid Films 377–378, 394–400. doi:10.1016/S0040-6090(00)01367-5

Hodge, A.M., Nieh, T.G., 2004. Evaluating abrasive wear of amorphous alloys using nanoscratch technique. Intermetallics 12, 741–748. doi:10.1016/j.intermet.2004.02.014

Huang, H., Zhao, H., Mi, J., Yang, J., Wan, S., Xu, L., Ma, Z., 2012. A novel and compact nanoindentation device for in situ nanoindentation tests inside the scanning electron microscope. AIP Adv. 2, 0–10. doi:10.1063/1.3676691

Hyun, S.K., Nakajima, H., 2003. Anisotropic compressive properties of porous copper produced by unidirectional solidification. Mater. Sci. Eng. A 340, 258–264. doi:10.1016/S0921-5093(02)00181-8

Inamura, V.I.K.V.R., Toda, V.J., Morita, V.T., 2006. Ultra high density perpendicular magnetic recording technologies. Fujitsu Sci. Tech. J 42, 122–130.

Inoue, A., Shen, B.L., Chang, C.T., 2004. Super-high strength of over 4000 MPa for Fe-based bulk glassy alloys in [(Fe1-xCox)0.75B0.2Si 0.05]96Nb4 system. Acta Mater. 52, 4093–4099. doi:10.1016/j.actamat.2004.05.022

Jang, B.K., Matsubara, H., 2005. Influence of porosity on hardness and Young's modulus of nanoporous EB-PVD TBCs by nanoindentation. Mater. Lett. 59, 3462–3466. doi:10.1016/j.matlet.2005.06.014

Jee, A.-Y., Lee, M., 2010. Comparative analysis on the nanoindentation of polymers using atomic force microscopy. Polym. Test. 29, 95–99. doi:10.1016/j.polymertesting.2009.09.009

Johnson, K.E., Choe, G., Acharya, B., Abarra, E., 2006. Perpendicular thin-film recording media ??? materials and design challenges. INTERMAG 2006 - IEEE Int. Magn. Conf. 2383, 716. doi:10.1109/INTMAG.2006.376440

Johnson, K.L., 1970. The correlation of indentation experiments. J. Mech. Phys. Solids 18, 115–126. doi:10.1016/0022-5096(70)90029-3

Ju, G., Peng, Y., Chang, E.K.C., Ding, Y., Wu, A.Q., Zhu, X., Kubota, Y., Klemmer, T.J., Amini, H., Gao, L., Fan, Z., Rausch, T., Subedi, P., Ma, M., Kalarickal, S., Rea, C.J., Dimitrov, D. V., Huang, P.W., Wang, K., Chen, X., Peng, C., Chen, W., Dykes, J.W., Seigler, M.A., Gage, E.C., Chantrell, R., Thiele, J.U., 2015. High Density Heat-Assisted Magnetic Recording Media and Advanced Characterization - Progress and Challenges. IEEE Trans. Magn. 51. doi:10.1109/TMAG.2015.2439690

Jung, Y.G., Lawn, B.R., Martyniuk, M., Huang, H., Hu, X.Z., 2004. Evaluation of elastic modulus and hardness of thin films by nanoindentation. J. Mater. Res. 19, 3076–3080. doi:10.1557/JMR.2004.0380

Katta, R.R., Polycarpou, A. a., Lee, S.-C., Suk, M., 2010. Experimental and FEA Scratch of Magnetic Storage Thin-Film Disks to Correlate Magnetic Signal Degradation With Permanent Deformation. J. Tribol. 132, 21902. doi:10.1115/1.4000848

Katta, R.R., Polycarpou, A. a., Lee, S.-C., Suk, M., 2010. Experimental and FEA Scratch of Magnetic Storage Thin-Film Disks to Correlate Magnetic Signal Degradation With Permanent Deformation. J. Tribol. 132, 21902. doi:10.1115/1.4000848

King, R.B., 1987. Elastic analysis of some punch problems for a layered medium. Int. J. Solids Struct. 23, 1657–1664. doi:10.1016/0020-7683(87)90116-8

Kitaoka, S., Tsuji, T., Yamaguchi, Y., Kashiwagi, K., 1997. Tribochemical wear theory of non-oxide ceramics in high-temperature and high-pressure water. Wear 205, 40–46. doi:10.1016/S0043-1648(96)07335-8

Kral, E.R., Komvopoulos, K., Bogy, D.B., 1996. Hardness of Thin-Film Media: Scratch Experiments and Finite Element Simulations. J. Tribol. 118, 1–11.

Kundu, S., Das, S.K., Sahoo, P., 2014. Properties of electroless Nickel at elevated temperature - A review. Procedia Eng. 97, 1698–1706. doi:10.1016/j.proeng.2014.12.321

Lee, J.H., Holland, T.B., Mukherjee, A.K., Zhang, X., Wang, H., 2013. Direct observation of Lomer-Cottrell locks during strain hardening in nanocrystalline nickel by in situ TEM. Sci. Rep. 3, 1061. doi:10.1038/srep01061

Lee, J., Zhang, Y., Crone, R.M., Ramakrishnan, N., Polycarpou, A.A., 2016. Wear Modeling of Nanometer Thick Protective Coatings. J. Tribol. 139, 21601. doi:10.1115/1.4033492

Lee, K.M., Yeo, C.-D., Polycarpou, A. a., 2006. Mechanical property measurements of thin-film carbon overcoat on recording media towards 1 Tbit⁄in[sup 2]. J. Appl. Phys. 99, 08G906. doi:10.1063/1.2166595

Lee, K.M., Yeo, C.-D., Polycarpou, A. a., 2008. Relationship between scratch hardness and yield strength of elastic perfectly plastic materials using finite element analysis. J. Mater. Res. 23, 2229–2237. doi:10.1557/JMR.2008.0279

Lemoine, P., Quinn, J.P., Maguire, P.D., Zhao, J.F., McLaughlin, J.A., 2007. Intrinsic mechanical properties of ultra-thin amorphous carbon layers. Appl. Surf. Sci. 253, 6165–6175. doi:10.1016/j.apsusc.2007.01.028

Lemoine, P., Quinn, J.P., Maguire, P.D., Zhao, J.F., McLaughlin, J.A., 2007. Intrinsic mechanical properties of ultra-thin amorphous carbon layers. Appl. Surf. Sci. 253, 6165–6175. doi:10.1016/j.apsusc.2007.01.028

Li, H., Randall, N.X., Vlassak, J.J., 2010. New methods of analyzing indentation experiments on very thin films. J. Mater. Res. 25, 728–734. doi:10.1557/JMR.2010.0095

Li, H., Valssak, J.J., 2009. Determining the Elastic Modulus and Hardness of an Ultrathin Film on a Substrate Using Nanoindentation. J. Mater. Res. 24, 1114–1126. doi:10.1557/JMR.2009.0144

Li, Q., Lee, C., Carpick, R.W., Hone, J., 2010. Substrate effect on thickness-dependent friction on graphene. Phys. Status Solidi Basic Res. 247, 2909–2914. doi:10.1002/pssb.201000555

Li, S., Li, Q., Carpick, R.W., Gumbsch, P., Liu, X.Z., Ding, X., Sun, J., Li, J., 2016. The evolving quality of frictional contact with graphene. Nat. Publ. Gr. 539, 4–1. doi:10.1038/nature20135

Li, Z., Brand, U., 2013. Towards Quantitative Characterisation of the Small Force Transducer Used in Nanoindentation Instruments 2013, 61–67. doi:10.4236/mi.2013.24009

Lichinchi, M., Lenardi, C., Haupt, J., Vitali, R., 1998. Simulation of Berkovich nanoindentation experiments on thin films using finite element method. Thin Solid Films 333, 278–286. doi:10.1016/S0040-6090(98)01263-2

Liu, D., Benstetter, G., Lodermeier, E., Chen, X., Ding, J., Liu, Y., Zhang, J., Ma, T., 2003. Surface and structural properties of ultrathin diamond-like carbon coatings. Diam. Relat. Mater. 12, 1594–1600. doi:10.1016/S0925-9635(03)00248-6

Liu, H., Tanaka, a., Umeda, K., 1999. The tribological characteristics of diamond-like carbon films at elevated temperatures. Thin Solid Films 346, 162–168. doi:10.1016/S0040-6090(98)01093-1

Liu, Y., Xiong, S., Lou, J., Bogy, D.B., Zhang, G., 2014. Quantitative relationship between contact stress and magnetic signal strength in perpendicular recording media. J. Appl. Phys. 115, 2014–2017. doi:10.1063/1.4865880

Lu, W., Komvopoulos, K., 2001. Nanomechanical and nanotribological properties of carbon, chromium, and titanium carbide ultrathin films. J. Tribol. 123, 717–724. doi:10.1115/1.1330737

Lucca, D.A., Herrmann, K., Klopfstein, M.J., 2010. Nanoindentation: Measuring methods and applications. CIRP Ann. - Manuf. Technol. 59, 803–819. doi:10.1016/j.cirp.2010.05.009

Luo, J., Stevens, R., 1999. Porosity-dependence of elastic moduli and hardness of 3Y-TZP ceramics. Ceram. Int. 25, 281–286. doi:10.1016/S0272-8842(98)00037-6

Ma, T.-B., Hu, Y.-Z., Wang, H., 2009. Molecular dynamics simulation of shear-induced graphitization of amorphous carbon films. Carbon N. Y. 47, 1953–1957. doi:10.1016/j.carbon.2009.03.040

Ma, X.G., Komvopoulos, K., Wan, D., Bogy, D.B., Kim, Y.S., 2003. Effects of film thickness and contact load on nanotribological properties of sputtered amorphous carbon thin films. Wear 254, 1010–1018. doi:10.1016/S0043-1648(03)00307-7

Mangolini, F., Rose, F., Hilbert, J., Carpick, R.W., 2013. Thermally induced evolution of hydrogenated amorphous carbon. Appl. Phys. Lett. 103. doi:10.1063/1.4826100

Mani Biswas, M., Knigge, B., 2016. Opportunities and Challenges of Atomistic Modeling to Simulate Amorphous Carbon Properties for Computer Hard-Disk Applications. IEEE Trans. Magn. 52. doi:10.1109/TMAG.2015.2496331

Marchon, B., Heiman, N., Khan, M.R., 1990. Evidence for tribochemical wear on amorphous carbon thin films. IEEE Trans. Magn. 26, 168–170. doi:10.1109/20.50524

Maschmann, M.R., Zhang, Q., Wheeler, R., Du, F., Dai, L., Baur, J., 2011. In situ SEM observation of column-like and foam-like CNT array nanoindentation. ACS Appl. Mater. Interfaces 3, 648–653. doi:10.1021/am101262g

Mate, C.M., Homola, A.M., 1997. Molecular tribology of disk drives. NATO ASI Ser., Ser.E 330(Micro/, 647–661. doi:10.1023/A:1019107305988

Mate, C.M., Marchon, B., Murthy, A.N., Kim, S.H., 2010. Lubricant-induced spacing increases at slider-disk interfaces in disk drives. Tribol. Lett. 37, 581–590. doi:10.1007/s11249-009-9555-y

Mcmillin, B.K., 1996. Materials research. Situ 11, 1–4.

Minor, A.M., Morris, J.W., Stach, E.A., 2001. Quantitative in situ nanoindentation in an electron microscope. Appl. Phys. Lett. 79, 1625–1627. doi:10.1063/1.1400768

Miyake, S., Yamazaki, S., 2013. Nanoscratch properties of extremely thin diamond-like carbon films. Wear 305, 69–77. doi:10.1016/j.wear.2013.05.005

Moler, C., 2009. Chapter 5 1–13. doi:10.1007/978-1-60761-380-0

Montagne A; Tromas, C; Audurier, V and Woirgard, J., 2009. A new insight on reversible deformation and incipient plasticity during nanoindentation test in MgO. J. Mater. Res. 24, 890–897. doi:10.1557/jmr.2009.0113

MTS Systems Corporation, 2002. The Nano Indenter ® XP 405. doi:D1418XPA-10629

Naito, K., Hieda, H., Sakurai, M., Kamata, Y., Asakawa, K., 2002. 2.5-Inch Disk Patterned Media Prepared By an Artificially Assisted Self-Assembling Method. IEEE Trans. Magn. 38, 1949–1951. doi:10.1109/TMAG.2002.802847

Note, A., n.d. Ultimate Solution for Ultra-Thin Film Systems 8–9.

Oh, I.H., Nomura, N., Masahashi, N., Hanada, S., 2003. Mechanical properties of porous titanium compacts prepared by powder sintering. Scr. Mater. 49, 1197–1202. doi:10.1016/j.scriptamat.2003.08.018

Oliver, W.C., Pharr, G.M., 2004. Measurement of hardness and elastic modulus by instrumented indentation: Advances in understanding and refinements to methodology. J. Mater. Res. 19, 3–20. doi:10.1557/jmr.2004.19.1.3

Options, U., n.d. High Temperature Stage 1–2.

Ozkan, T., Demirkan, M.T., Walsh, K.A., Karabacak, T., Polycarpou, A.A., 2016. Density modulated nanoporous tungsten thin films and their nanomechanical properties. J. Mater. Res. 31, 2011–2024. doi:10.1557/jmr.2016.197

Pan, X.F., Zhang, H., Zhang, Z.F., Stoica, M., He, G., Eckert, J., 2005. Vickers hardness and compressive properties of bulk metallic glasses and nanostructure-dendrite composites. J. Mater. Res. 20, 2632–2638. doi:Doi 10.1557/Jmr.2005.0328

Parallel, E., Actuators, P., n.d. , At Any Position, X.

Passeri, D., Bettucci, A., Biagioni, A., Rossi, M., Alippi, A., Lucci, M., Davoli, I., Berezina, S., 2008. Quantitative measurement of indentation hardness and modulus of compliant materials by atomic force microscopy. Rev. Sci. Instrum. 79, 56–59. doi:10.1063/1.2949387

Pelegri, A.A., Huang, X., 2008. Nanoindentation on soft film/hard substrate and hard film/soft substrate material systems with finite element analysis. Compos. Sci. Technol. 68, 147–155. doi:10.1016/j.compscitech.2007.05.033

Pelletier, H., 2006. Predictive model to estimate the stress-strain curves of bulk metals using nanoindentation. Tribol. Int. 39, 593–606. doi:10.1016/j.triboint.2005.03.019

Pelletier, H., Krier, J., Cornet, A., Mille, P., 2000. Limits of using bilinear stress-strain curve for finite element modeling of nanoindentation response on bulk materials. Thin Solid Films 379, 147–155. doi:10.1016/S0040-6090(00)01559-5

Pelletier, H., Krier, J., Mille, P., 2006. Characterization of mechanical properties of thin films using nanoindentation test. Mech. Mater. 38, 1182–1198. doi:10.1016/j.mechmat.2006.02.011

Peng, J., Sergiienko, A., Mangolini, F., Stallworth, P.E., Greenbaum, S., Carpick, R.W., 2016. Solid state magnetic resonance investigation of the thermally-induced structural evolution of silicon oxide-doped hydrogenated amorphous carbon. Carbon N. Y. 105, 163–175. doi:10.1016/j.carbon.2016.04.021

Peng, P., Sezen, a. S., Rajamani, R., Erdman, a. G., 2010. Novel MEMS stiffness sensor for force and elasticity measurements. Sensors Actuators A Phys. 158, 10–17. doi:10.1016/j.sna.2009.12.002

Piramanayagam, S.N., 2007. Perpendicular recording media for hard disk drives. J. Appl. Phys. 102. doi:10.1063/1.2750414

Piramanayagam, S.N., Srinivasan, K., 2009. Recording media research for future hard disk drives. J. Magn. Magn. Mater. 321, 485–494. doi:10.1016/j.jmmm.2008.05.007

Quinn, T.F.J., 1967. The Effect of "Hot-Spot" Temperatures on the Unlubricated Wear of Steel. A S L E Trans. 10, 158–168. doi:10.1080/05698196708972175

Re, M., 2015. Tech Talk on HDD Areal Density Safe Harbor Statement 1–14.

Robertson, J., 2002. Diamond-like amorphous carbon. Mater. Sci. Eng. R Reports 37, 129–281. doi:10.1016/S0927-796X(02)00005-0

Robertson, J., 1999. Ultrathin Carbon Overcoats for Magnetic Storage Technology. Proc. Symp. Interface Technol. Towar. 100 Gb/in 39–45.

Robertson, J., 2003. Requirements of ultrathin carbon coatings for magnetic storage technology. Tribol. Int. 36, 405–415. doi:10.1016/S0301-679X(02)00216-5

Robertson, J., 2008. Comparison of diamond-like carbon to diamond for applications. Phys. Status Solidi Appl. Mater. Sci. 205, 2233–2244. doi:10.1002/pssa.200879720

Rose, F., Wang, N., Smith, R., Xiao, Q.-F., Inaba, H., Matsumura, T., Saito, Y., Matsumoto, H., Dai, Q., Marchon, B., Mangolini, F., Carpick, R.W., 2014. Complete characterization by Raman spectroscopy of the structural properties of thin hydrogenated diamond-like carbon films exposed to rapid thermal annealing. J. Appl. Phys. 116, 123516. doi:10.1063/1.4896838

Rusanov, A., Nevshupa, R., Fontaine, J., Martin, J.M., Le Mogne, T., Elinson, V., Lyamin, A., Roman, E., 2015. Probing the tribochemical degradation of hydrogenated amorphous carbon using mechanically stimulated gas emission spectroscopy. Carbon N. Y. 81, 788–799. doi:10.1016/j.carbon.2014.10.026

Saha, R., Nix, W.D., 2002. Effects of the substrate on the determination of thin film mechanical properties by nanoindentation. Acta Mater. 50, 23–38. doi:10.1016/S1359-6454(01)00328-7

Sawa, T., Tanaka, K., 2001. Evaluating Performance of Nanoindentation Instruments 16.

Schwarzer, N., Chudoba, T., Richter, F., 2006. Investigation of ultra thin coatings using nanoindentation. Surf. Coatings Technol. 200, 5566–5580. doi:10.1016/j.surfcoat.2005.07.075

Search, H., Journals, C., Contact, A., Iopscience, M., Address, I.P., n.d. Structural change of a hydrogenated carbon film upon 475. doi:10.1088/0953-8984/13/22/105

Shekhter, L.N., Tripp, T.B., Lanin, L.L., 2001. Method for producing tantalum/niobium metal powders by the reducction of their oxides with gaseous magnesium 1, 1–17. doi:10.1197/jamia.M1139.Adar

Shondeep, L., Energy, C., Energy, C., Cited, R., 1995. United States Patent [191.

Song, W., Ovcharenko, A., Knigge, B., Yang, M., Talke, F.E., 2012. Tribology International Effect of contact conditions during thermo-mechanical contact between a thermal flying height control slider and a disk asperity. Tribiology Int. 55, 100–107. doi:10.1016/j.triboint.2012.05.016

Srinivasan, K., Piramanayagam, S.N., Wong, S.K., Kay, Y.S., 2008. Microstructure and magnetic properties of CoCrPt-SiO2 perpendicular recording media with synthetic nucleation layers. J. Appl. Phys. 103. doi:10.1063/1.2831499

Suh, A.Y., Polycarpou, A.A., 2005. Adhesive contact modeling for sub-5-nm ultralow flying magnetic storage head-disk interfaces including roughness effects. J. Appl. Phys. 97. doi:10.1063/1.1914951

Tabor, D., 1985. Indentation Hardness and Its Measurement: Some Cautionary Comments. Microindentation Tech. Mater. Sci. Eng. ASTM Inter, 129–129–31. doi:10.1520/stp32955s

Tabor, D., 1956. The physical meaning of indentation and scratch hardness. Br. J. Appl. Phys. 7, 159. doi:10.1088/0508-3443/7/5/301

Tabor, D., 1970. The hardness of solids. Rev. Phys. Technol. 1, 145. doi:10.1088/0034-6683/1/3/I01

Tang, K., Bian, X., Choe, G., Takano, K., Mirzamaani, M., Wang, G., Zhang, J., Xiao, Q.F., Ikeda, Y., Risner-Jamtgaard, J., Xu, X., 2009. Design consideration and practical solution of high-performance perpendicular magnetic recording media. IEEE Trans. Magn. 45, 786–792. doi:10.1109/TMAG.2008.2010479

Tang, W.C., Nguyen, T.C.H., Howe, R.T., 1989. Laterally Driven Polysilicon Resonant Microstructures. Sensors and Actuators 20, 25–32. doi:10.1016/0250-6874(89)87098-2

Tayebi, N., Polycarpou, A. a., Conry, T.F., 2004. Effects of substrate on determination of hardness of thin films by nanoscratch and nanoindentation techniques. J. Mater. Res. 19, 1791–1802. doi:10.1557/JMR.2004.0233

Ter, A., Benlahsen, M., Branger, V., Badawi, F., Zellama, K., 1998. D | REIJ T6D The effect of hydrogen evolution on the mechanical properties of hydrogenated amorphous carbon a 5, 3–7.

The, W.H.Y., For, N., Technology, A., 2006. Performance of 54, 319–323.

Tomasella, E., Meunier, C., Mikhailov, S., 2001. a-C : H thin films deposited by radio-frequency plasma : influence of gas composition on structure , optical properties and stress levels. Surf. Coatings Technol. 286–296.

Treatment, S., Higgs, C.E., Canning, W., 1974. The effect of heat treatment on the structure and hardness of an electrolessly deposited nickel-phos- phorus alloy 2, 315–326.

Treatment, S., Jones, R., Pollock, H.M., Cleaver, J. a S., Hodgest, C.S., 2002. Adhesion Forces between Glass and Silicon Surfaces in Air Studied by AFM : Effects of Relative Hunidity , Particle T * ffiffiH : 8045–8055.

Tsui, T.Y., Pharr, G.M., 1999. Substrate effects on nanoindentation mechanical property measurement of soft films on hard substrates. J. Mater. Res. 14, 292–301. doi:10.1557/JMR.1999.0042

Van der Donck, T.， , Muchlado, M., W, Z.E., Achanta, S., Carvalho, N.J.M., Celis, J.-P., 2009. Effect of hydrogen content in aC: H coatings on their tribological behaviour at room temperature up to 150° C. Surf. Coatings Technol. 203, 3472–3479. doi:10.1016/j.surfcoat.2009.05.032

Vanhulsel, A., Blanpain, B., Celis, J.-P., Roos, J., Dekempeneer, E., Smeets, J., 1998. Study of the wear behaviour of diamond-like coatings at elevated temperatures. Surf. Coat. Technol. 98, 1047–1052. doi:10.1016/S0257-8972(97)00227-2

VanLandingham, M.R., Juliano, T.F., Hagon, M.J., 2005. Measuring tip shape for instrumented indentation using atomic force microscopy. Meas. Sci. Technol. 16, 2173–2185. doi:10.1088/0957-0233/16/11/007

Vanlandingham, M.R., 2003. Review of Instrumented Indentation. J. Res. Natl. Inst. Stand. Technol. 108, 249–265. doi:10.6028/jres.108.024

Venkatraman, C., Brodbeck, C., Lei, R., 1999. Tribological properties of diamond-like nanocomposite coatings at high temperatures. Surf. Coatings Technol. 115, 215–221. doi:10.1016/S0257-8972(99)00241-8

Voevodin, A.A., Phelps, A.W., Zabinski, J.S., Donley, M.S., 1996. Friction induced phase transformation of pulsed laser deposited diamond-like carbon. Diam. Relat. Mater. 5, 1264–1269. doi:10.1016/0925-9635(96)00538-9

Walters, J.K., Rigden, J.S., Newport, R.J., Howells, W.S., Parker, S.F., 1995. The effect of temperature on the structure of amorphous hydrogenated carbon. Phys. Scr. 1995. doi:10.1088/0031-8949/1995/T57/025

Weller, D., Parker, G., Mosendz, O., Champion, E., Stipe, B., Wang, X., Klemmer, T., Ju, G., Ajan, A., 2014. A HAMR media technology roadmap to an areal density of 4 Tb/in2. IEEE Trans. Magn. 50. doi:10.1109/TMAG.2013.2281027

Xin, K., Lambropoulos, J.C., 2000. Densification of fused silica: Effects on nanoindentation. Proc. SPIE - Int. Soc. Opt. Eng. 4102, 112–121. doi:10.1117/12.405275

Xu, J., Furukawa, M., Nakamura, A., Honda, M., 2009. Mechanical demagnetization at head disk interface of perpendicular recording. IEEE Trans. Magn. 45, 893–898. doi:10.1109/TMAG.2008.2010670

Ye, N., Komvopoulos, K., 2003. Indentation Analysis of Elastic-Plastic Homogeneous and Layered Media: Criteria for Determining the Real Material Hardness. J. Tribol. 125, 685. doi:10.1115/1.1572515

Yu, N., Polycarpou, A.A., 2004. Use of the focused ion beam technique to produce a sharp spherical diamond for sub-10nm nanoindentation measurements. J. Vac. Sci. Technol. B 22, 668–672. doi:10.1116/1.1676467

Yu, N., Polycarpou, a a, Conry, T.F., 2003. Experimental , Analytical and Finite Element Studies of the Nanoindentation Technique to Investigate Material Properties of Surface Layers Less Than 100 Nanometers Thick 61801.

Yu, N., Bonin, W.A., Polycarpou, A.A., 2005. High-resolution capacitive load-displacement transducer and its application in nanoindentation and adhesion force measurements. Rev. Sci. Instrum. 76, 1–8. doi:10.1063/1.1878532

Yu, N., Polycarpou, A.A., Conry, T.F., 2004. Tip-radius effect in finite element modeling of sub-50 nm shallow nanoindentation. Thin Solid Films 450, 295–303. doi:10.1016/j.tsf.2003.10.033

Zhang, Y., Polycarpou, A.A., 2016. Lubricant Transfer Model at the Head-Disk Interface in Magnetic Storage Considering Lubricant – Lubricant Interaction. Tribol. Lett. 62, 1–9. doi:10.1007/s11249-016-0688-5

Zhang, Y., Polycarpou, A.A., 2016. A single asperity sliding contact model for molecularly thin lubricant. Microsyst. Technol. doi:10.1007/s00542-016-2910-7

Zhang, Y., Polychronopoulou, K., Humood, M., Polycarpou, A.A., 2017. High temperature nanotribology of ultra-thin hydrogenated amorphous carbon coatings. Carbon 123, 112–121. doi:10.1016/j.carbon.2017.07.047

Zhou, B., Prorok, B.C., 2010. A New Paradigm in Thin Film Indentation. J. Mater. Res. 25, 1671–1678. doi:10.1557/JMR.2010.0228

Zhu, Y., Espinosa, H.D., 2005. An electromechanical material testing system for in situ electron microscopy and applications. Proc. Natl. Acad. Sci. U. S. A. 102, 14503–8. doi:10.1073/pnas.0506544102

Zorzi, J.E., Perottoni, C.A., 2013. Estimating Young's modulus and Poisson's ratio by instrumented indentation test. Mater. Sci. Eng. A 574, 25–30. doi:10.1016/j.msea.2013.03.008

APPENDIX A: DERIVATION OF THE MODIFIED GOVERNING EQUATION

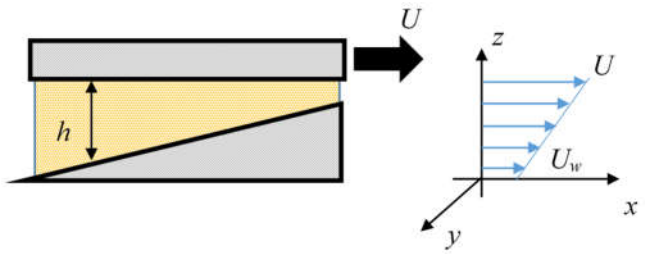

Figure A.1 Nomenclature for lubrication with slippery wall

A nomenclature for lubrication for the solid-liquid interface is depicted by Fig. A.1. Derivation of Eq. (6.2) begins from the Navier-Stokes equation:

$$\rho\left(\frac{\partial u}{\partial t}+u\frac{\partial u}{\partial x}+v\frac{\partial u}{\partial y}+w\frac{\partial u}{\partial z}\right)=-\frac{\partial p}{\partial x}+\mu\left(\frac{\partial^2 u}{\partial x^2}+\frac{\partial^2 u}{\partial y^2}+\frac{\partial^2 u}{\partial z^2}\right) \tag{A.1}$$

Assuming steady-state conditions and neglecting the velocity gradients along the z and y directions, i.e., $\partial u/\partial y=\partial u/\partial z=0$, the Naiver-Stokes equation simplifies to:

$$\rho\left(u\frac{\partial u}{\partial x}\right)=-\frac{\partial p}{\partial x}+\mu\left(\frac{\partial^2 u}{\partial z^2}\right) \tag{A.2}$$

The velocity along x keeps constant, thus $\partial u/\partial x=0$, then we have:

$$-\frac{\partial p}{\partial x}+\mu\left(\frac{\partial^2 u}{\partial z^2}\right)=0 \tag{A.3}$$

Integration with respect to z to obtain:

$$u=\frac{1}{\mu}\frac{\partial p}{\partial x}\left(\frac{z^2}{2}+Az+B\right) \tag{A.4}$$

Using the boundary conditions for a slip case: $u(z=0)=U_W$; $u(z=h)=U$, then we have the velocity profile:

$$u(z)=\frac{1}{2\mu}\frac{\partial p}{\partial x}z(z-h)+\frac{(h-z)U_W}{h}+\frac{z}{h}U \tag{A.5}$$

Similarly, we have velocity expression along *y* by using boundary conditions:

$$v=\frac{1}{\mu}\frac{\partial p}{\partial y}\left(\frac{z^2}{2}\right) \tag{A.6}$$

The mass conservation requires that net flow in a finite control volume is zero:

$$\frac{\partial q_x}{\partial x}-\frac{\partial q_y}{\partial y}=0 \tag{A.7}$$

, where

$$\begin{aligned} q_x &= \int_0^h\left[\frac{1}{2\mu}\frac{\partial p}{\partial x}z(z-h)+\frac{(\mathrm{h}-z)U_W}{h}+\frac{z}{h}U\right]dz \\ &= \left[\frac{1}{2\mu}\frac{\partial p}{\partial x}\left(\frac{z^3}{3}-\frac{hz^2}{2}\right)+\left(z-\frac{z^2}{2h}\right)U_W+\frac{z^2}{2h}U\right]\Bigg|_0^h \\ &= -\frac{h^3}{12\mu}\frac{\partial p}{\partial x}+\frac{h}{2}(U+U_W) \end{aligned} \tag{A.8}$$

$$q_y=-\frac{h^3}{12\mu}\frac{\partial p}{\partial y} \tag{A.9}$$

Substitute q_x and q_y into the mass conservation relation:

$$\frac{\partial}{\partial x}\left(\frac{h^3}{12\mu}\frac{\partial p}{\partial x}\right)+\frac{\partial}{\partial y}\left(\frac{h^3}{12\mu}\frac{\partial p}{\partial y}\right)=\frac{\partial}{\partial x}\left(\frac{U+U_W}{2}h\right) \tag{A.10}$$

By definition of the slip factor *f**:

$$f^*=(U-U_W)/U=h/(b+h). \tag{A.11}$$

The governing equation for pressure becomes:

$$\frac{\partial}{\partial x}\left(\frac{h^3}{12\mu}\frac{\partial p}{\partial x}\right)+\frac{\partial}{\partial x}\left(\frac{h^3}{12\mu}\frac{\partial p}{\partial y}\right)=\frac{\partial}{\partial x}\left[\left(1-\frac{f^*}{2}\right)h\right]U \tag{A.12}$$

APPENDIX B.1: DERIVATION OF LUBE-LUBE INTERACTION PRESSURE ΠLUBE IN EQ. (7.6)

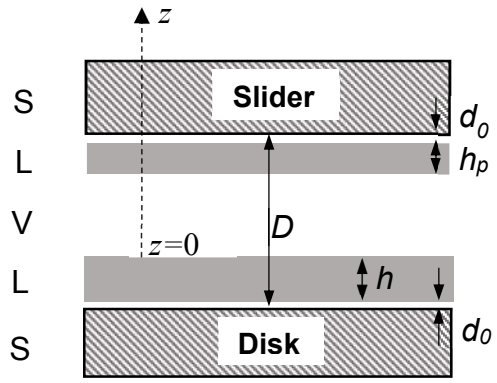

Figure B.1.1 Schematic view for lube-lube interaction of the Head-disk Interface.

Consider the lubricant on the disk, the interaction energy with the lubricant with distance of *dz* on the slider is an integration form:

$$W_{\text{lube-lube}} = -\frac{A_{LVL}}{6\pi}\int_{D-2h-2d_0}^{D-h-2d_0}\frac{dz}{z^3} = -\frac{A_{LVL}}{12\pi}\left[\frac{1}{\left(D-h-2d_0\right)^2}-\frac{1}{\left(D-h-h_p-2d_0\right)^2}\right] \quad \text{(B.1.1)}$$

Assuming the lubricant thickness picked up by the slider is also h, i.e., $h_p=h$, then the equation becomes:

$$W_{\text{lube-lube}} = --\frac{A_{LVL}}{12\pi}\left[\frac{1}{\left(D-h-2d_0\right)^2}-\frac{1}{\left(D-2h-2d_0\right)^2}\right] \quad \text{(B.1.2)}$$

Obtaining the force per unit area (pressure) for lube-lube interaction:

$$\pi_{\text{lube}} = -\frac{\partial W_{\text{lube-lube}}}{\partial D} = \frac{A_{LVL}}{6\pi}\left[\frac{1}{\left(D-h-2d_0\right)^3}-\frac{1}{\left(D-2h-2d_0\right)^3}\right] \quad \text{(B.1.3)}$$

APPENDIX B.2: EFFECTS OF THE BONDING RATIO ON THE LUBRICANT TRANSFER, FOR FIG. 7.10 (B)

When the lubricant bonding ratio equals to zero (BR=0), A_{LVS} plays a very weak role in the determination of the critical clearance, as indicated by Fig. 7, and therefore the π_{slider} term in Eq. 4 can be neglected and reduces to:

$$\frac{A_{VLS}}{6\pi\left(h+d_0\right)^3}=\frac{A_{LVL}}{6\pi}\left\{\frac{1}{\left[D-2h-2d_0\right]^3}-\frac{1}{\left(D-h-2d_0\right)^3}\right\} \tag{B.2.1}$$

Also neglecting the attraction from the lubricant itself, namely the second term on the RHS of Eq. 7.13, it reduces to:

$$\frac{A_{VLS}}{6\pi\left(h+d_0\right)^3}-\frac{A_{LVL}}{6\pi}\frac{1}{\left[D-2h-2d_0\right]^3}=0 \tag{B.2.2}$$

Then the critical solid distance can be solved:

$$D_{C(BR=0)}=2\left(h+d_0\right)+\sqrt[3]{\frac{A_{LVL}}{A_{VLS}}}\left(h+d_0\right) \tag{B.2.3}$$

To the contrary, when BR is equal to one (BR=1), there is no mobile lubricant available for transfer, thus $\pi_{Lube}=0$; and Eq. 7.4 reduces to:

$$\frac{A_{VLS}}{6\pi\left(h+d_0\right)^3}-\frac{A_{LVS}}{6\pi}\frac{1}{\left[D-h-d_0\right]^3}=0 \tag{B.2.4}$$

, which is the form widely used in the literature that ignores lube-lube interaction. The solution for the critical solid distance is:

$$D_{C(BR=1)}=h+d_0+\sqrt[3]{\frac{A_{LVS}}{A_{VLS}}}\left(h+d_0\right) \tag{B.2.5}$$